Some Aspects of Gas Turbine Fuel Preparation and Turbomachinery Response to LCV Fuels

Eriksson, Pontus

2009

Some Aspects of Gas Turbine Fuel Preparation and Turbomachinery Response to LCV Fuels

Sprays, LCV Fuel Combustion, Turbo-machinery Off-Design Behaviour and Bluff Body Stabilized Combustion

Pontus Eriksson

Doctoral Thesis

Division of Thermal Power Engineering
Department of Energy Sciences
Faculty of Engineering
Lund University
Sweden

Some Aspects of Gas Turbine Fuel Preparation and Turbomachinery Response to LCV Fuels

Sprays, LCV Fuel Combustion, Turbo-machinery Off-Design Behaviour and Bluff Body Stabilized Combustion

Pontus Eriksson

May 2009

Doctoral Thesis

Division of Thermal Power Engineering
Department of Energy Sciences
Faculty of Engineering
Lund University
Sweden
http://www.energy.lth.se

ISBN 978-91-628-7681-4
ISRN LUTMDN/TMHP--09/1064—SE
ISSN 0282-1990
Printed by Media-Tryck, Sweden, April 2009

To Hypatia

Abstract

We humans thrive on energy. Much of this energy comes from combustion. Until now, most of our combustion devices have been operating on fossil fuels. Fossil fuels are, however, a limited resource. Whether they will last 50 or 300 years, it is still only a few human life spans at most, and we have to drastically limit our consumption long before we run out of oil, gas and coal in order not to overheat our atmosphere. In any event, fossil fuel combustion has to be replaced at some point.

So what can we do?

In the shorter perspective we may sequester and store the CO_2 that fossil fuel combustion emits. This will perhaps allow us to limit the effects of global warming somewhat, but it is costly and in many cases difficult to realize. Meanwhile we must work to find sustainable alternatives. Bio-fuel combustion is one of many alternatives. It is CO_2-neutral if managed correctly, but it presents other problems. In many cases, pollutants like NO_X and SO_X will be emitted. These emissions are primarily linked to smog and acidification of lakes. We therefore need to improve our methods of harvesting the bio-energy.

This thesis gives some background information on environmental issues as the scientific community at-large currently sees it. It tries to relate the plethora of current combustion technologies that may be used in gas turbines to those issues. Some basic principles on design of combustion systems are given. Different candidate fuels for gas turbine combustion are discussed. Combustion of bio-fuels is treated and provides background material for Papers 1, 4, 5, 6 and 7. Pre- and post-treatment technologies are covered briefly. Bluff body stabilized combustion is discussed in relation to Paper 3.

In the case of liquid fuel combustion, the liquid must first be atomized before it can be burnt. A chapter on atomization discusses the various mechanisms involved in the break-up process of a liquid column being injected into gas. Papers 2, 8 and 9 deal with sprays.

Laser-based diagnostics tools are used extensively to analyze fluid flow. In Papers 2, 8 and 9, PIV and PDA have been used. An overview of these techniques is provided.

Process simulation tools are used to model and analyze plants and machinery. A flow network is set up between components which act on a fluid to produce a desired outcome. The system may be a complete plant or

e.g. a gas turbine. Papers 4, 5, 6 and 7 use this tool to analyze component behavior in one- and two-shaft industrial gas turbines and a combined cycle plant. All are fired with high, medium and low calorific fuels.

Contents

Nomenclature

Symbols

[ ]	Molar concentration	[mol/L]
A	Area	[m^2]
c	Progress variable, constant	[-]
c	Speed of light	[m/s]
C	Correlation function	[-]
c_p	Specific heat at constant pressure	[J/kgK]
d, D	Diameter	[m]
D_t	Characteristic length of obstacle or flow feature	[m]
e	Unit vector	[m]
E_a	Activation energy	[J/mol]
e_L	Laminar flame thickness	[m]
f	Frequency	[Hz]
Fr	Froude number	[-]
g	Gravity	[m/s^2]
g_{cr}	Critical quenching velocity gradient	[s^{-1}]
G	Flux of momentum	[varies]
k	constant	[varies]
k	Turbulent kinetic energy	[m^2/s^2]
k	Chemical kinetics reaction rate constant	[varies]
l_t	Turbulent length scale	[m]
L	Characteristic length	[m]
L_i	Thermoacoustic loss	[W/m^3]
$\dot{m}$	Mass flow	[kg/s]
m	Ratio of refractive indices	[-]
Ma	Mach number	[-]
Oh	Ohnesorge number	[-]
P, p	Pressure	[Pa]
p´	Pressure fluctuation	[Pa]
$\dot{q}'$	Heat release	[W/m^3]
R	Universal gas constant	[J/molK]
r, R	Radius	[m]
Re	Reynolds number	[-]
s_L	Laminar flame speed	[m/s]
S	Swirl number	[-]
St	Stokes number	[-]
t	Time	[s]
T	Time period	[s]

T	Temperature	[K]
u_i	Velocity	[m/s]
u´	Turbulent velocity	[m/s]
U	Particle velocity (LDA), Axial velocity (swirl)	[m/s]
V	Characteristic velocity	[m/s]
V	Volume	[m^3]
W	Tangential velocity	[m/s]
We	Weber number	[-]
x	spatial position { x y z}	[m]
x, x_i, x_j	Coordinate	[m]
x_f	Flame front position	[m]

Subscripts

B	Brewster
c	Critical, chemical, column, continuous phase
d	Dispersed
D	Doppler
eq	Equilibrium
f	Fluid
g	Gas
i	Incident, a counter
in	At inlet
j	Coordinate (1, 2, 3)
l	Laminar, liquid
s	Scattered
t, T	Turbulent, tangential
u	Unburnt
v	Particle

Greek symbols

β	Combustion Intensity parameter	[MW/m^3atm]
δ	Displacement	[m]
δ_t	Flame thickness	[m]
ε	Turbulent dissipation rate	[m^2/s^3]
η	Kolmogorov length scale	[m]
η_c	Combustion efficiency	[%]
Θ	Combustor Loading Parameter	[$kg/sPa^{1.75}m^{2.75}$]
θ	Angle between the incoming laser beams	[°]
λ	Wavelength of laser light	[m]
λ_u	Thermal diffusivity	[m^2/s]

μ	Viscosity	[Pa s]
μ_{str}	Empirical model constant (0.28)	
ν	Kinematic viscosity	[m^2/s]
ξ	Reaction coordinate	[m]
ρ	Density	[kg/m^3]
σ	Surface tension	[N/m]
σ_c	Turbulent Schmidt Number	[-]
τ	Time scale	[s]
φ	Off axis angle in PDA setup	[°]
ϕ	Fuel/air ratio over stoichiometric fuel/air ratio a.k.a. equivalence ratio	[-]
Φ	PDA phase shift	[°]
ψ	Elevation angle in PDA	[°]

Acronyms

AB	Afterburner
AFR	Air Fuel Ratio
AMF	Air Mass Flow
BBO	Basset-Boussinesq-Oseen (equation)
bn	Billion
CC	Combined Cycle
CFBC	Circulating Fluidized Bed Combustion
CFCs	ChloroFluoroCarbons
CFD	Computational Fluid Dynamics
CI	Combustion Intensity
CLP	Combustor Loading Parameter
COSTAIR	Continuous Staged Air Combustion
CR	Conversion Rate for FBN
DLE	Dry Low Emissions
DLN	Dry Low NO_X
DNS	Direct Navier-Stokes
DU	Dobson Unit
EDM	Electrical Discharge Machining
EGR	Exhaust Gas Recirculation
EvGT	Evaporative Gas Turbine
FBN	Fuel Bound Nitrogen
FLOX	FLameless OXidation
GCV	Gross Calorific Value
GT	Gas Turbine
GWP	Global Warming Potential

FBC	Fluidized Bed Combustion
FLOX	FlameLess OXidation
HCV	High Calorific Value gas (~50 MJ/kg)
HRSG	Heat Recovery Steam Generator
IGCC	Integrated Gasification & Combined Cycle
IPCC	Intergovernmental Panel on Climate Change
JAS	Jakt Attack Spaning
KHI	Kelvin-Helmholtz Instability
LBO	Lean BlowOut
LCV	Low Calorific Value gas (~5 MJ/kg)
L/D	Length/Diameter
LDA	Laser Doppler Anemometry
LES	Large Eddy Simulation
LHV	Lower Heating Value
LJIGCF	Liquid Jet in Gas Crossflow
LPP	Lean Prevaporized Premixed or Lean Partially Premixed
LPT	Lagrangian Particle Tracking
LVG	Low (heating) Value Gas
MCV	Medium Calorific Value gas (~20 MJ/kg)
MP	MegaPixels
NF	Normalized Flow
NG	Natural Gas
ODS	Ozone Depleting Substances
PDA	Phase Doppler Anemometry
PFR	Plug Flow Reactor
PIV	Particle Imaging Velocimetry
PM	Photo Multiplyer (tube)
ppm	parts per million
ppb	parts per billion
PSR	Perfectly Stirred Reactor
RAPRENO$_X$	RAPid REduction of NO$_X$
RCL	Rich Catalytic/Lean burn
RQL	Rich burn/Quick quench/Lean Burn
SCR	Selective Catalytic Reduction
SNCR	Selective Non-Catalytic Reduction
STIG	Steam Injection Gas Turbine
TAPS	Twin Annular Pre-mixing Swirler
TBM	Tertiary Butyl Mercaptan
TFC	Turbulent Flame Closure
TFN	Total Fixed Nitrogen
TID	Turbine Inlet Duct

TIT	Turbine Inlet Temperature
TOMS	Total Ozone Mapping Spectrometer
TVC	Trapped Vortex Combustor
UHC	Unburnt HydroCarbons
UV	Ultra Violet (radiation)
VOC	Volatile Organic Compounds
VOF	Volume of Fluid (method)

1 Introduction

1.1 Background

The incredible technological progress that we have witnessed in the last centuries is to a large extent due to combustion. In fact, our ways of living would be completely different without combustion. From early times when we prepared our food over open fire, through today when everything from heating, cooling, production of electric energy, processing of raw materials, manufacturing of goods and transportation rely on combustion, we have benefited immensely from this phenomenon. Ultimately it can be said that the cells in our body get their energy from slow combustion, i.e. the process in which the chemical bonds of energy-rich molecules such as glucose are converted into energy usable for life processes.

Combustion doesn't come without problems though. To an overwhelming extent, combustion involves some fuel in the form of hydrocarbons and air. During combustion, the carbon will combine with the oxygen to form carbon dioxide CO_2. If this results in significantly raised CO_2 concentrations in the atmosphere, it is going to have an impact on Earth's climate. At high temperatures, small quantities of oxygen will combine with nitrogen to form nitric oxides NO, nitrogen dioxide NO_2 and nitrous oxides N_2O. These molecules are to varying degrees linked to smog, acid rain, global warming and depletion of the stratospheric ozone layer. The fuel may also contain other species with a potential to form harmful compounds during combustion.

The process of converting the chemically stored energy of the fuel into heat is itself a rather simple task. Most well-designed combustion systems will convert nearly 100% of the chemically available energy into heat. The exception is perhaps jet engine afterburners, which will convert about 90% of the available energy. The field of combustion research is therefore very much directed towards the study of polluting and climate-altering emissions, and methods to suppress, sequester or avoid these emissions. It is a challenging but rewarding task to work in the field of combustion, since so much still needs to be done before we can say that we can "burn with a clean conscience".

It is not enough though, to be able to convert chemically-stored energy to heat in an efficient and sustainable manner. We must also make the most out of the available energy by producing it in a user-friendly format and distributing it efficiently for end use. Here the gas turbine fills an important role in that it is an integral part of modern combined cycle plants having

high overall efficiency. The European Community has taken initiatives to improve energy utilization by drafting the "Cogeneration Directive" EC/2004/8 as a means to push this technology. The EC has also drafted directive 2001/77/EC in order to meet our energy demands in a more sustainable way. This directive promotes the use of renewable fuels, where biofuels are key components. Combustion of these biofuels is therefore also expected to become much more important in the future.

1.2 Objectives

- Give an account of the consensus in the scientific community about the state of our environment in terms of pollution and climate.
- Identify the links between combustion in general and gas turbine combustion in particular on one side, and environmental impact on the other
- Give an overview of different fuel sources for gas turbine combustion and identify advantages and disadvantages with each
- Give an account of current techniques to abate polluting emissions from combustion of various fuels and provide background information to Papers 1, 4, 5, 6 and 7
- Discuss bluff body stabilized combustion and provide background information to Paper 3
- Give an overview of the different phenomena encountered in spray formation and provide background information for Papers 2, 8 and 9
- Provide a cursory overview of the process simulation tool used in Papers 4-7
- Give an overview of laser-based flow measurement techniques used in Papers 2, 8 and 9

1.3 Methodology

The study of gas turbines involves many fields of science. In this thesis the emphasis has been on combustion and fuel preparation.

In Paper 1 a diffusion combustor was designed and built in cooperation with AIT Ltd. (Smiths group). AIT's facilities were used to test the hardware with synthetically produced biomass gasification gas, blast furnace gas and compositions with varying amounts of H_2O and H_2/CO. The effects of fuel-bound nitrogen were studied using NH_3 injection.

A spray rig was designed, built and used to study spray in cross-flow under low-Weber conditions (Paper 2). A test section was built and used in another (existing rig) to study spray in cross-flow under higher-Weber conditions (Papers 8 and 9). The sprays were investigated with PIV and PDA. Matlab™ was used to recreate a measured spray. The spray was then injected in a RANS CFD package using Lagrangian Particle Tracking (Papers 8 and 9). Measurements and computations were compared.

In Paper 3, four different RANS turbulence models were compared for bluff body combustion using the Zimont Turbulent Flame Closure model.

The behaviors of one- and two-shaft gas turbines as they are subjected to some of the medium and low-calorific fuels (MCV, LCV) we may encounter in the future have been studied (Papers 4, 5, 6 and 7). Here the approach has been to model a gas turbine in a simulation package and study the effects on turbomachinery components and discuss necessary modifications. Paper 7 deals with an MCV/LCV fired gas turbine in a combined cycle plant.

1.4 Outline of thesis

Chapter 1. Contains the background and the objectives for the work

Chapter 2. Discusses environmental concerns in terms of pollutions and climate change

Chapter 3. Gives an overview of gas turbine emissions

Chapter 4. Discusses gas turbine combustor design

Chapter 5. Discusses different fuels for gas turbine combustion

Chapter 6. Gives an overview of spray formation and discusses how different mechanisms lead to breakup

Chapter 7. Discusses spray rig design, build and modifications

Chapter 8. Gives an introduction to process simulation as it pertains to gas turbines and plants containing gas turbines

Chapter 9. Details laser-based methods used in the research. In particular Laser Doppler Anemometry, Phase Doppler Anemometry, and Particle Imaging Velocimetry are discussed

Chapter 10. Bibliography

Chapter 11. Summary of papers

1.5 Acknowledgements

This thesis is the result of an Industrial Ph. D. program initiated by Rolf Gabrielsson and Göran Holmqvist of Volvo Aero. I wish to extend my deepest gratitude to Rolf and Göran for providing the opportunity and support on this journey. My thanks also go out to Bengt-Olof Elfström, Lena Andersson and Håkan Schmidt for their valuable support.

I also wish to thank my supervisor Jens Klingmann for his expertise and guidance throughout this work.

A very warm Thank You also goes out to Göran Josefsson, Volvo Cars, for lending "his" PDA system. Without it, the spray papers would not be possible.

I would also like to thank technicians Rutger Lorensson, Ingjald Andreasson and Fredrik Johansson and the ladies on the fifth floor: Maj-Lis Roos, Ingrid Elofsson and Gunvi Andersson.

Finally I wish to thank all my colleagues at Energy Sciences and especially my co-authors Raik Orbay, Magnus Genrup, Klas Jonshagen and Fredrik Hermann.

Financing of the various projects within this thesis are from Volvo Aero Corporation, Swedish National Energy Administration (STEM), Gullspångs Kraft AB, Stockholm Energi AB, Graninge AB, TPS Termiska Processer AB, Sigtuna Energi AB, E.ON and Vinnova. I wish to extend my gratitude to all financing bodies.

2 Earth's atmosphere

Earth's atmosphere is a mixture of gases consisting of approximately 78% nitrogen, 21% oxygen, 1% argon (dry volume). The atmosphere also contains water vapor. The amount varies between 0 and 4%. On average the atmosphere contains 0.4% water vapor (by volume). In addition there are trace amounts of carbon dioxide, neon, helium methane krypton and hydrogen. Of these, CO_2 is dominating at 383 ppm. The atmosphere plays a fundamental role in the survival of all life on Earth. It provides oxygen for animal life, CO_2 for plant life, protection against cosmic radiation, traps heat from the sun such that temperatures become conducive to life and re-circulates water from the oceans to land. Earth's atmosphere has not always had the composition we see today. It is believed that the atmosphere has undergone three development stages:

- H_2O-CO_2-NH_3 atmosphere (ca. 4.4 bn years ago)
- cyanobacteria oxygenated atmosphere (ca. 2.5 bn years ago)
- photosynthesis oxygenated atmosphere

Animal and plant life has evolved with the changing atmosphere. They are contingent on it being sufficiently stable to allow for evolutionary adaptation to occur. Two events in recent history have the potential to rapidly change the composition of Earth's atmosphere:

- human population growth
- industrialization

Some of the consequences of these changes as it pertains to combustion are discussed in this chapter and serve as a background and motivation for the following chapters.

2.1 Photochemical smog

When NO_X mixed with hydrocarbons (aka volatile organic compounds or VOC for short) is subjected to sunlight, photochemical smog forms. Besides NO_X and VOCs, the smog contains particulate matter, SO_2 and ozone (O_3). Smog is hazardous to humans, animals and vegetation. Since it is fairly simple to measure ozone concentrations in air this is often used as a measure of smog severity.

The history of smog is quite interesting in that it was the first serious air pollution problem that humanity took on. The following is recounted from California's perspective (California Air Resources Board [1]) since parts of

this state were severely affected due to the geological and meteorological circumstances there.

As early as 1943, citizens of Los Angeles experienced smog. Visibility was only 3 blocks and people complained about irritated eyes, respiratory discomfort, nausea, and vomiting. The phenomenon was at that time termed "gas attack" and a nearby butadiene plant was blamed. The plant was shut down, but the problem persisted. In 1952 over 4000 deaths were attributed to "Killer Fog" in London, England. In the early fifties Dr. Arie Haagen-Smit discovered the nature and causes of photochemical smog [2]. He found that nitrogen oxides and hydrocarbons in the presence of ultraviolet radiation from the sun form smog (a key component of which is ozone). In 1956 "Killer Fog" enveloped London, England resulting in 1,000 deaths above normal. By 1970 California's population reached 20 million people. Total registered vehicles exceeded 12 million and vehicle miles travelled were 110 billion (Figure 1). Cumulative California vehicle emissions for nitrogen oxides and hydrocarbons were about 1.6 million tons/year (Figure 2). The South Coast Air Basin's maximum one-hour ozone concentration recorded was 0.58 ppm, which is nearly five times greater than the health-based US national standard of < 0.12 ppm that was adopted in the subsequent year (Figure 3). The problems associated with smog were by now very serious in certain parts of the world. From 1955 tougher and tougher laws were implemented to stave off the problems. In the mid 70s the three-way catalytic converter was introduced to control hydrocarbons, nitrogen oxides, and carbon monoxide emitted from petrol-fuelled vehicles. In the 1970s trends were broken and cumulative California vehicle emissions for nitrogen oxides and hydrocarbons started to decline despite a rapid growth of fossil-fuelled vehicles and an ever-increasing demand for energy. In 1975 there were 118 Stage 1 Alerts (>0.20 ppm ozone) issued to warn Californian residents of hazardous levels of smog. By the year 2000 there were none. Although we have seen a tremendous growth of combustion devices during the past decade, it has been shown that smog can be combated with legislation and technological progress.

While the situation has improved a great deal in many places in the world, other parts like China (which relies heavily on coal-fired power plants and open pit mines releasing large quantities of CH_4) still very much suffer from smog.

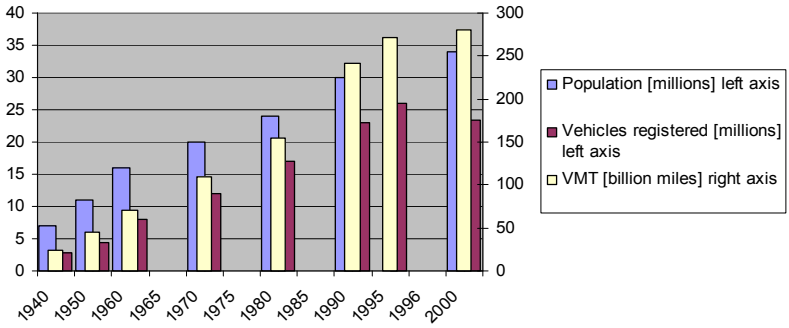

Figure 1: Population growth, vehicles registered and Vehicle Miles Travelled in California

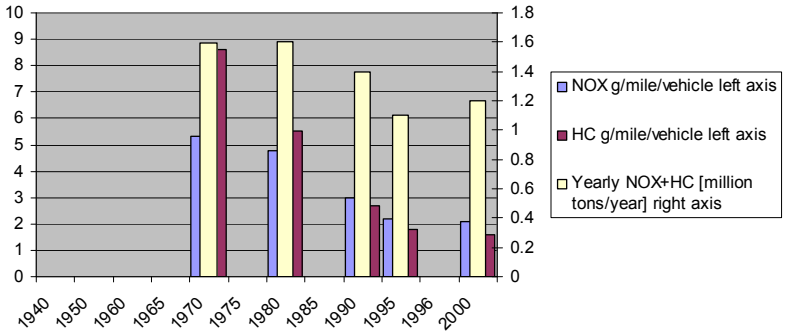

Figure 2: NOX emissions, HC emissions and yearly cumulative emissions of NO_X and VOCs for California

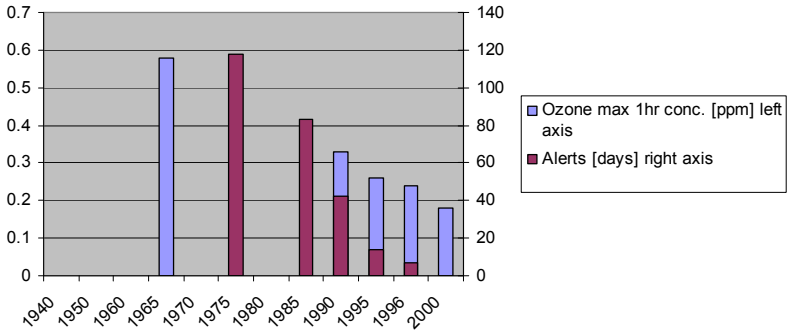

Figure 3: Maximum one-hour ozone concentrations and Stage 1 Smog Alerts for California

2.2 Acid rain [3]

Acid rain forms when NO_X and SO_2 emissions mainly from fossil fuel combustion come in contact with the moisture contained in the air. Sulphuric acid (H_2SO_4), ammonium nitrate (NH_4NO_3) and nitric acid

(HNO_3) form in the atmosphere and can be transported hundreds of kilometers before being washed out as rain or snow. Chemical precursors to acid rain can also come from volcanic activities and decaying vegetation. In the United States, roughly 2/3 of all SO_2 and 1/4 of all NO_X come from electric power generation that relies on burning fossil fuels.

Acid rain will affect life in lakes and streams because the acidity will cause elevated aluminium concentrations, which are highly toxic. Acid rain destroys forests and painted surfaces, causes corrosion of metals and destroys marble and limestone. The associated particulate matter derivatives - sulfates and nitrates - will reduce visibility and deposit as black dirt on buildings. Nitrates will add to the problems of over-fertilization of waters. Many scientific studies have shown a relationship between fine particulate matter and increased illness and premature death from heart and lung disorders.

2.3 Global warming

The greenhouse effect has been widely discussed in the past decade. It seems, however, that the scientific community is coming to a consensus that the Earth's climate is becoming warmer. This can be seen as [4]:

- increased global-average land, biospheric and tropospheric temperatures since the 1960s
- decrease of Arctic and Antarctic ice extent
- change in the Arctic's southern extent of the discontinuous permafrost zone in the last century
- receding mountain glaciers

2.3.1 CH_4 as a greenhouse gas

Methane (CH_4) is a potent greenhouse gas. It is 21 times more powerful than CO_2[1] [5]. It will also participate in the formation of tropospheric ozone, which is a greenhouse gas. Wetlands, rice fields, cattle farming, biomass burning and landfills are some of the sources of methane in the atmosphere [6]. According to a compilation by IPCC [7] about 65% of the methane is put into the atmosphere through anthropogenic activities. About 25% of this comes from the energy sector. An overwhelming part of this is released through mining and transportation of hydrocarbons and coal. Only a very small fraction is released during actual combustion in industrial

[1] 100-year GWP [5] (Global Warming Potential)

processes. CH_4 accounts for about 20% of the total change in the radiative balance[2] on Earth. It's lifetime in the atmosphere is about 12 years [4].

2.3.2 CO_2 as a greenhouse gas

CO_2 is the single most important greenhouse gas. It accounts for about 60% of the total change in the radiative balance on earth [4]. Anthropogenic CO_2 comes from fossil fuel combustion (64%), changes in land use, e.g. forest clearing (35%) and cement manufacture (1%). CO_2 from fossil fuel combustion represents about 14% of the total amount of CO_2 in the atmosphere. About 60% of all anthropogenic CO_2 released into the atmosphere has been absorbed by the oceans and the terrestrial biosphere [8]. CO_2 can be very long-lived in the troposphere with a lifetime of 5–200 years for a small perturbation[3].

2.3.3 N_2O (nitrous oxide or laughing gas) as a greenhouse gas

N_2O is 310 times more potent as a greenhouse gas when comparing with CO_2 [5]. The life expectancy of an N_2O molecule is in the order of 114 years [7], so concentration changes are long-lived. Taking into account the rise of N_2O levels during the industrialized period, one finds that N_2O adds approximately 6% to the radiative forcing on earth [7].

Major sources of anthropogenic N_2O are the use of synthetic fertilizer and production of nitric acid and nylon. Contributions from combustion processes in the power industry are mainly from low-temperature combustion such as FBC and CFBC (Circulating Fluidized Bed Combustion) combustors for boilers [9] and some post-combustion NO removal systems e.g. Selective Non-Catalytic Reduction (SNCR) de-NO_X based on urea or ammonia [10] (see Chapter 4.17).

Calculated lifetimes of N_2O in combustion products indicate that for temperatures above 1500K, the lifetime of N_2O is typically less than 10 ms [11]. Steele et al. found that NO_X and N_2O emissions are on par at the combustion temperature 1430K for a lean premixed jet-stirred CO/H_2/air flame [12]. Gutierrez et al. [10] set a lower limit for waste and biomass combustion temperatures at 900°C. It is, based on these assertions, prudent to consider N_2O emissions from low-temperature combustors below

[2] From the year 1750 to 1998

[3] No single lifetime can be determined for carbon dioxide. (See IPCC 2001 [7])

approximately 1400K. Since CO burnout in gas turbine applications needs about 1500K for 10 ms [13], N_2O will therefore not be the limiting factor in most applications.

2.3.4 NO_x as a greenhouse gas

NO and NO_2 are not greenhouse gases in themselves. In the presence of NO_X, CO and hydrocarbons are oxidized. This will produce ozone, which is a greenhouse gas.

2.3.5 O_3 as a greenhouse gas

According to the IPCC Third Assessment Report [7], the radiative forcing of tropospheric ozone is estimated to be about 24% of that of CO_2. Even though total ozone is decreasing, in the troposphere it is increasing. This will lead to a net contribution to the greenhouse effect. The overall contribution to the greenhouse effect remains to be assessed since there are many un-quantified effects.

2.3.6 CFCs as greenhouse gases

Artificially created chlorofluorocarbons are the strongest greenhouse gases per molecule. They account for as much as 14% of the radiative forcing [7] and can also be very long lived (up to 50 000 years for certain molecules). Compounds containing flourine are particularly vicious. The emissions of CFCs were however drastically reduced after the signing of the Montreal protocol in 1987. Halogenated hydrocarbons containing Cl, F or Br may be formed in combustion of landfill gases depending on the composition of the ingredients used to make the gas. Of the three, Cl usually dominates [14].

2.3.7 Global warming

In regions where the temperature never climbs above freezing, snow accumulates. It changes over the years to ice as it is compacted by more recent precipitation. In the process small amounts of air are trapped and preserved for posterity. Changes in the gas composition of these trapped bubbles can therefore provide valuable information about earth's past atmosphere. Global temperatures are related to isotopic content of ^{18}O and deuterium. This may thus be used as a gage of historic temperature change spanning several 100 000 years. Figure 4 shows data from the Vostok 420 000 year ice core sample [15]. One can see a striking correlation between CO_2 levels, CH_4 levels, changes in ^{18}O isotope content and therefore average global temperature change. It can be seen that, as the CO_2 levels rise, so does the temperature of the precipitation as it was evaporating

somewhere else on earth. It is furthermore believed that dust levels rose when the climate became colder and dryer. The Vostok record confirms much higher aerosol fallout during cold glacial periods than during interglacials.

During the industrial revolution the average CO_2 concentration in the atmosphere has risen to 383 ppm. CO_2 levels have never, prior to this, exceeded 300 ppm during the entire 420 000 year history we know from the Vostok ice core samples. The situation is similar with CH_4, with record high levels. Adding the radiative forcing effects from CO_2, CH_4, vapour, sea ice, and possibly clouds make it reasonable to assume that greenhouse gases have, at a global scale, contributed significantly (possibly about half, that is, 2–3°C) to the globally averaged glacial–interglacial temperature change seen in the Vostok record [15].

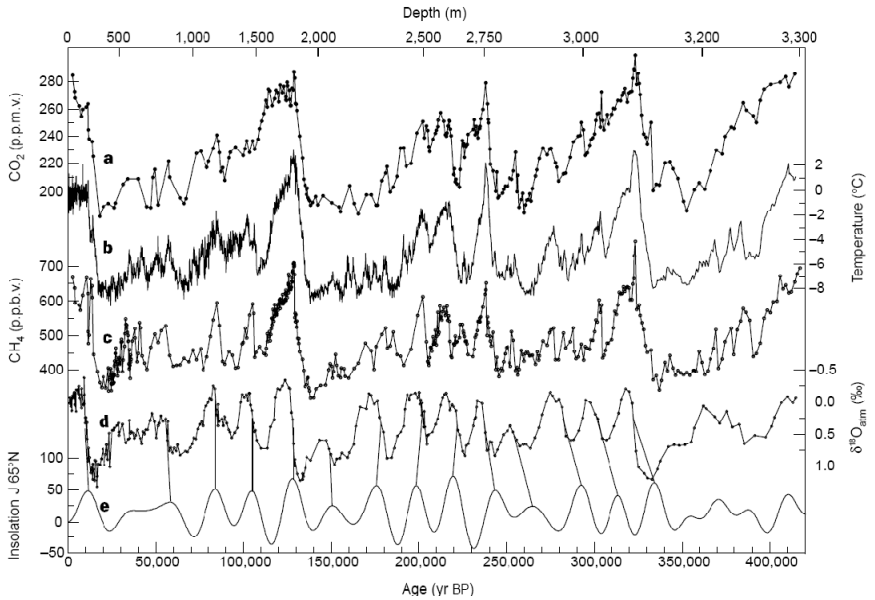

Figure 4: Vostok ice core data over 420 000 years of ice core records: **a**) CO_2, **b**) Isotopic temperature of the atmosphere profile, **c**) CH_4, **d**) $\delta^{18}O_{atm}$, **e**) mid-June insulation at 65°N [W/m^2] [15]

According to IPCC[4], the average surface temperature could rise by between 1.1°C and 6.4°C by the end of the century as a result of anthropogenic greenhouse gases. The actual outcome depends on choice of

[4] Intergovernmental Panel on Climate Change

scenario and climate model [4]. The change in temperature will not be uniform however. The models predict that more heating will take place at the poles and less at the equator. Since the ice covering Greenland and the Antarctic rests on land, increased melting here will result in higher sea water levels. Maximum density for water occurs around +4°C. Since the average temperature of the ocean surface waters is 15-17°C an increase in temperature is accompanied with an expansion. Both melting and expansion will therefore contribute to rising sea levels.

We are, however, currently in a warm period, the Holocene interglacial, which has been suggested, will continue for 3–19 thousand years. In the long perspective it may prove correct to artificially increase CO_2 levels. In the shorter perspective (still thousands of years) it seems that CO_2 levels are undesirably high.

Figure 5 shows the change in atmospheric concentrations of the three most common greenhouse gases since 1850. All these gases are relevant to combustion, either directly or indirectly.

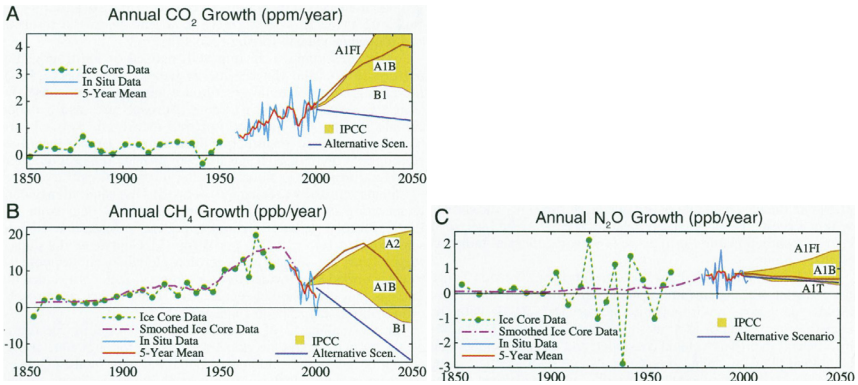

Figure 5: CH_4, CO_2 and N_2O concentration changes since 1850 [16]

2.4 Ozone layer

Ninety percent of the atmospheric ozone resides in the stratosphere, which lies between 10 and 50 km from the ground layer. The ozone layer is an effective screen for UV light. Without it, many life forms, including us humans, would be threatened by extinction.

2.4.1 Ozone layer depletion [17]

It has been known since 1979 that tropospheric ozone formation is linked to NO_X and stratospheric ozone destruction is linked to N_2O [18]. Since 1985 the connection between stratospheric ozone depletion and CFC's (Chloro-

Fluoro-Carbons), compounds containing bromine and other related halogen compounds were also known [19]. Figure 6 shows the ozone hole over Antarctica in September 2006 and measurements of ozone since 1979. Measurements during the 1960s, when the minimum ozone levels started to decrease were generally around 300-350 DU (Dobson Units). At times the ozone levels over Antarctica may drop to only 30% of normal levels. Levels below 100 DU have been observed over Antarctica since 1994. Due to differences in air circulation patterns and also because the stratosphere does not become as cold there, ozone levels over the Arctic do not drop as dramatically. Nevertheless, small but quite distinct "mini holes" have been observed even in tempered zones [20].

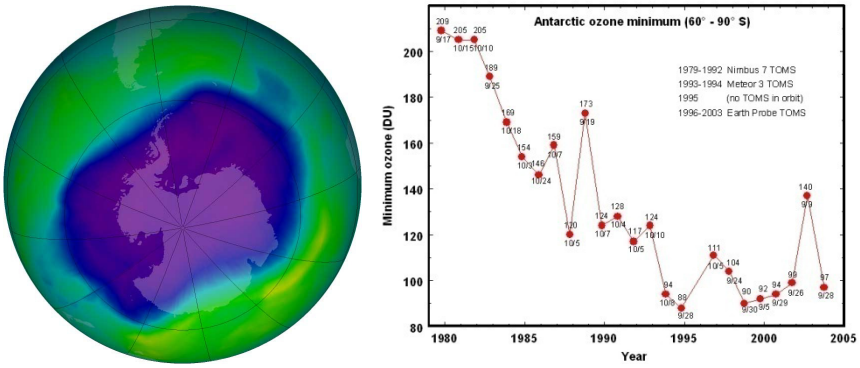

Figure 6: Largest ever recorded "ozone hole" in Sept. 2006 and lowest value of ozone measured by TOMS each year in the "ozone hole" over Antarctica [NASA]

Since NO_X, and to some extent N_2O, is produced in most combustion systems, the mechanism by which NO, NO_2 and N_2O interact with stratospheric ozone will be touched on.

N_2O production in the troposphere is particularly important because it is an unreactive gas which is not water-soluble and does not interact with the available radiation. It can therefore survive long enough (O. 100–150 years) to be able to reach the stratosphere. Once it has reached the stratosphere it may be destroyed in the following ways:

$$N_2O + h\nu \rightarrow N_2 + O\ (\sim 90\%),\ \lambda \leq 310\ nm \qquad (2.1a,b)$$

$N_2O + O(^1D) \rightarrow 2\mathbf{NO}$ (~10%), (^1D) denotes a particular excitation

The nitric oxide acts as a catalyst viz:

$$\mathbf{NO} + O_3 \rightarrow NO_2 + O_2 \quad (2.2a)$$

$$NO_2 + O \rightarrow O_2 + \mathbf{NO} \quad (2.2b)$$

$$\text{Net: } O_3 + O \rightarrow 2O_2 \quad (2.2c)$$

The concentration of N_2O has increased by about 10% in the last 100 years and it is currently increasing by about 0.5 ppb/year. This trend can be observed in Figure 5c.

NO and NO_2 are not long-lived enough to be transported from the ground to the stratosphere. Being very reactive, they will be chemically converted to nitric acid (HNO_3) and rain out within 5-10 days (see Chapter 2.2). If on the other hand, NO and NO_2 are created in the stratosphere as is the case with supersonic jet propulsion, they may directly take part in the destruction of O_3.

The most important source of N_2O is biological fixation followed by denitrification. This cycle happens naturally, but is reinforced by agricultural fertilization. It is now believed that combustion is only a minor contributor to the observed increase of N_2O.

Since the global ratification of the Montreal Protocol in 1987, the release of compounds that deplete ozone in the stratosphere i.e. chloro-fluoro-carbons (CFCs), halons, carbon tetrachloride, and methyl chloroform have all decreased slowly. Figure 7 shows that stratospheric Ozone-Depleting Substances (ODS) peaked in 1994. In (a), CFC production is shown in black. HCFCs are shown in grey. In (b), combined effective abundances of ODS is shown. In (c), measured and projected global stratospheric ozone change is shown. Complete recovery of the ozone layer will not occur before the year 2050 [22]. (d) shows erythermal (sunburning) UV radiation change. The hatched area accounts for uncertainties for climate-related changes in clouds and aerosols.

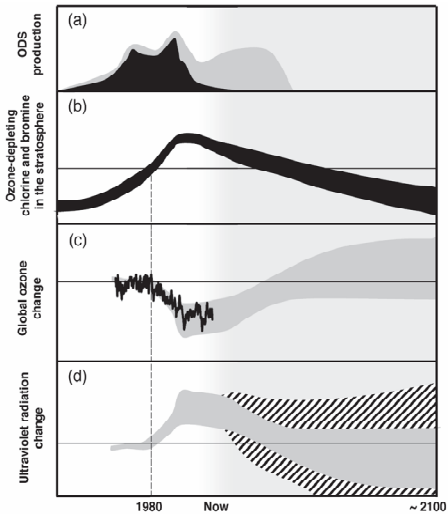

Figure 7: Ozone-Depleting Substances, history and projections [21]

3 Gas turbine emissions

3.1 Chemical kinetics of flames

Combustion is chemical oxidation of a fuel. The chemically stored energy is converted to heat in reactions that are predominantly exothermic. Many reactions will occur concurrently, even when the simplest fuels are oxidized. As an example: a detailed reaction scheme for oxidation of hydrogen may contain 19 elemental reactions even though only the two elements, O and H, are present [23]. In order to accurately model even the simplest hydrocarbons, detailed schemes will have hundreds of elemental reactions.

In the case where a laminar premixed type flame front is studied, one may fix a reaction coordinate to some position of the flame front and study the evolution of different species and various intensive properties like temperature and density. Figure 8 shows such an example where progress is expressed in terms of a distance from the flame front. Sometimes the reaction coordinate is expressed as time, reflecting the fact that the flame front is propagating through the mixture at a certain velocity; the flame speed.

Depending on temperature, pressure and concentrations, some species will find themselves in equilibrium with respect to some species, while not being in equilibrium with others. Net reactions will occur between species not being in equilibrium. Eventually, given enough time, all species will reach steady state-concentrations. This will happen when production and destruction of all species balance. If the system changes, by adding or removing heat, changing pressure or changing the concentration of some species the system will readjust given enough time. Introducing a catalyst or inhibitor will affect reaction rates. They have no effect on chemical equilibrium however.

Chemistry computations can thus be aimed at calculating equilibrium or time-dependent concentrations. The latter is called chemical kinetics.

In order to understand the relative importance of certain reactions, given certain conditions, a reaction path diagram (such as in Figure 9) may be constructed. This can be a valuable tool in understanding the chemistry. Thick arrows will indicate major reaction paths.

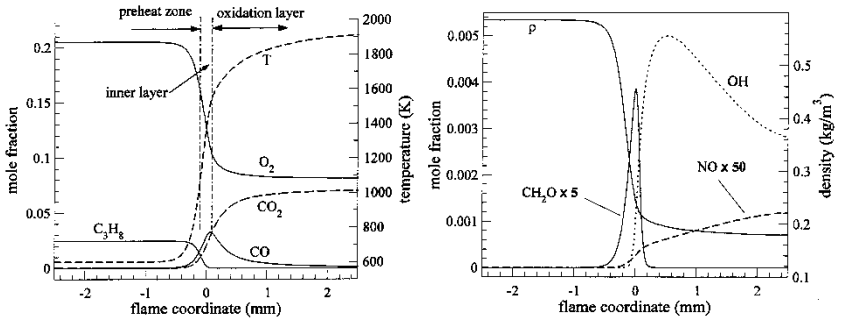

Figure 8: Laminar premixed C_3H_8/air flame, 1 atm, ϕ=0.6 [24]

Reaction rates may in the simplest form be expressed as:

$$\frac{d[AB]}{dt} = k_f \cdot [A] \cdot [B] \tag{3.1}$$

for the simple elemental (2nd order) reaction:

$$A + B \xrightarrow{k_f} AB \tag{3.2}$$

Here the brackets denote species concentrations.

k_f is temperature-dependent. Like concentration dependence, the relationships deduced for temperature dependence vary greatly. The most common form is the "Arrhenius' rate equation":

$$k_f = AT^n e^{\frac{-E_a}{RT}} \tag{3.3}$$

Here; AT^n is the pre-exponential, or frequency factor and E_a is the activation energy.

Strictly speaking it isn't concentrations, but rather partial pressures, which will determine reaction kinetics, but assuming perfect gases, molar concentrations, mole fractions and partial pressures will be interchangeable. Summing all partial pressures will give the total pressure of the system. Increasing the pressure in a gaseous reaction will increase the number of collisions between reactants and therefore increase reaction rates.

Expressing all forward- and backward-reaction rates for each elemental reaction, integrating with respect to time and summing contributions to each species will yield the overall time-dependent concentrations of each species.

3.2 CO formation in combustion

CO is very toxic [25], therefore there are strict limits on allowable concentrations in the exhaust from gas turbines. At ambient temperatures its half-life in the earth's atmosphere is, however, counted in hours. In time, CO will oxidize to CO_2.

CO forms as intermediate species in the conversion to CO_2 of fuels containing carbon. Under rich conditions there will be a lack of oxidizer to complete combustion. Large amounts of CO will form under these conditions. In the primary zone of diffusion-type combustors (see Chapter 4.4) operating on diesel or natural gas, temperatures are sufficiently high to favor large quantities of CO over CO_2 due to dissociation. At temperatures around 1800 K and residence times in excess of 8 ms, practically all CO will be converted to CO_2 under lean to stoichiometric conditions. At $\phi \approx 0.7$ the highest conversion to CO_2 will occur [26]. At lower temperatures and leaner conditions, reaction rates go down and large quantities of CO may escape unburnt. Reactions may also be quenched due to high turbulent strain rates. Care must be taken in the design of a gas turbine combustor to avoid cold and/or rich pockets from e.g. dilution holes, liner cooling air or poor fuel/air mixing.

3.3 CO_2 formation in combustion

CO_2 is an inevitable product from combustion of hydrocarbons. The quantity released is dependent on the H/C relation of the fuel and also the specific energy content of a fuel. Taking these two effects into account, the CO_2 release from some common fuels are according to Table 1.

Fuel	H/C	CO_2 emissions [g/MJ]
Natural Gas	4/1	57
Oil	2/1	78
Coal	0 – 1/10	95
Biofuels	3/20	100

Table 1: H/C relation and CO_2 emissions from fuels [27], [28]

Biofuels are, however, considered to be CO_2 neutral since the CO_2 emitted during combustion is balanced by an equal amount absorbed as new biological material is formed.

3.4 NO_x formation in combustion

3.4.1 Thermal NO_x

Thermal NO_X is produced at high-combustion temperatures. It is described by the Zeldovich mechanism:

$$O + N_2 \rightarrow \mathbf{NO} + N \quad (3.4a)$$

$$N + O_2 \rightarrow \mathbf{NO} + O \quad (3.4b)$$

$$N + OH \rightarrow \mathbf{NO} + H \quad (3.4c)$$

The mechanism starts with oxygen atoms forming from the H_2–O_2 radical pool or from dissociation of O_2 molecules. The oxygen atoms attack the nitrogen molecules in the air.

Assuming the first reaction to be rate determining and equilibrium between O and O_2, the formation rate of thermal NO can be written:

$$\frac{d[NO]}{dt} = 2k_{O+N_2 \rightarrow NO+N} \cdot k_{\frac{1}{2}O_2 \rightarrow O,eq} \cdot [O_2]^{1/2} \cdot [N_2] \quad (3.5)$$

where the two rate constants follow the Arhenius type expressions:

$$k = AT^n e^{-\frac{E_a}{RT}} \quad (3.6)$$

The rate constants in Equation (3.5) are strongly temperature-dependent but the whole equation is only square root-dependent on the O_2 concentration. Comparing stoichiometric combustion (at ~2100K) of the reference gas from Paper 1 with lean combustion of methane (ϕ=0.69, T_{ad}~2100K) one finds that $[O_2]^{1/2} \cdot [N_2]$ in the post flame zone is some six times higher for the methane flame. $[N_2]$ is very similar for the two cases. It is also much more abundant than $[O_2]$ and therefore not rate-determining. $[O_2]$ is however almost 30 times less in the LVG case. The reduced equilibrium concentration of O_2 typically seen in stoichiometric LVG combustion therefore allows elevated temperatures without excessive thermal NO_X production. The typical 1800K maximum combustion temperature given for LPP combustors in order to avoid excessive thermal NO_X is therefore not applicable to LVG combustion.

In Paper 1 the stoichiometric combustion temperature given for the various gas compositions are in the range 1911K – 2394K. Still the measured NO_X levels are in the single-digit range up to approximately 2100K. It is therefore possible to use diffusion-type combustors for LVG gases (see Chapter 4.4). This type of combustor offers several advantages in

terms of simple design, compactness and less thermo-acoustics when comparing with the LPP concept (Chapter 4.5).

3.4.2 Fuel Bound NO_x (FBN)

Fuels based on organic matter may contain nitrogen. The fuel-bound nitrogen is markedly more reactive compared with nitrogen in air. As much as 50 – 90% of this nitrogen will be converted to NH_3, NH_2, NH and small quantities of HCN and CN during thermal decomposition. A large portion of these species will oxidize in the flame and turn into NO_X.

The amount of fuel-bound nitrogen that is converted to NO_X is often described by the conversion rate:

$$CR = \frac{[\text{Total\_NO}_X] - [\text{Thermal\_NO}_X]}{[\text{NH}_3]} \frac{\text{Air} + \text{Fuel\_vol\_flow}}{\text{Fuel\_vol\_flow}} \cdot 100 \ \% \qquad (3.7)$$

Especially in lean combustion and in the presence of CH_4 large amounts of fuel-bound nitrogen will be converted to NO_X. The conversion process occurs in the flame on a timescale similar to the prompt NO_X mechanism. Post flame quenching is therefore not possible [11].

Natural Gas contains negligible amounts of nitrogen and will therefore not form NO_X through this mechanism.

3.4.3 Prompt NO_x [29]

In the 1970s Fenimore showed that that the thermal NO_X mechanism could not explain all NO_X formed, especially in cooler, under-stoichiometric conditions and for short residence times. Fenimore found no prompt NO in CO or H_2 flames [30]. This would suggest that the presence of carbon and hydrogen together was important. He proposed that prompt NO_X was formed from HCN. From Figure 9 it can be understood that HCN is instrumental for the formation of both prompt NO_X and fuel-bound NO_X (FBN), as there is no path from N_2 or FBN (shown as FN) that does not involve this molecule.

For combustion of hydrocarbons, he suggested the following reaction path:

$$N_2 + CH \rightarrow HCN + N \qquad (3.8a)$$

$$HCN \xrightarrow{+O} NCO \xrightarrow{+H} NH \xrightarrow{+H} N \xrightarrow{+O_2, +OH} \mathbf{NO} \qquad (3.8b)$$

This path will only be active in regions where combustion is incomplete and CH molecules are present. This means in the flame front. Since the formation of nitric oxide through this mechanism is fast, the nitric oxide

formed is denoted prompt NO. Prompt NO is only slightly temperature dependent.

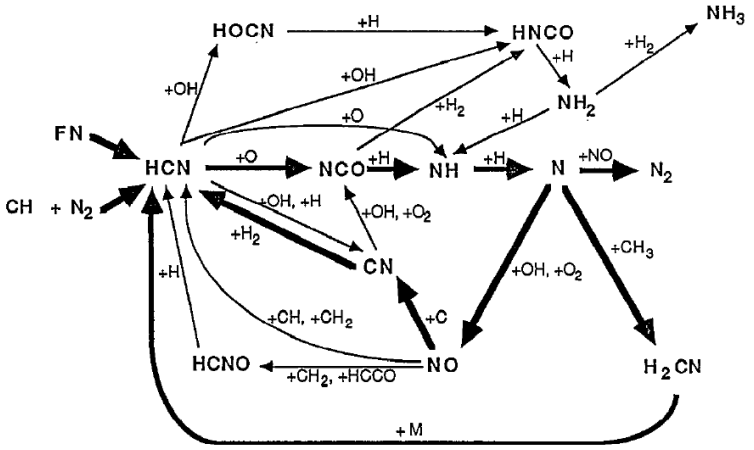

Figure 9: Prompt NO formation from N_2 and FBN conversion to NO [30]

Prompt NO has historically only contributed to a small fraction of the total NO_X emissions. With the advent of low-NO_X combustors operating at single digit values the importance of this mechanism has however increased.

3.4.4 The N_2O mechanism [29]

Another mechanism that was presented in the 1970s is the N_2O mechanism. Here NO forms from the intermediate N_2O according to the following scheme [12]:

$$N_2 + O + M \rightarrow N_2O + M \quad (3.9a)$$

$$N_2O + O \rightarrow 2\mathbf{NO} \quad (3.9b)$$

$$N_2O + H \rightarrow \mathbf{NO} + NH \quad (3.9c)$$

$$N_2O + H \rightarrow N_2 + OH \quad (3.9d)$$

$$N_2O + O \rightarrow N_2 + O_2 \quad (3.9e)$$

$$N_2O + OH \rightarrow N_2 + HO_2 \quad (3.9f)$$

where M represents an arbitrary third-body component. N_2O is oxidized to NO by reactions 3.5b and c. Reactor calculations suggest that the N_2O mechanism can dominate at lean conditions.

3.5 SO_2 formation, sulfur, sour gas, mercaptans

Sour Gas is any gas that contains impurities that form acidic combustion products. More commonly, however, Sour Gas is associated with hydrogen sulphide or H_2S.

In general the sulphur content in natural gas is low enough not to be an issue. One-third of the world's natural gas reserves, however, contain prohibitive levels of carbon dioxide and hydrogen sulfide. As an example, the Lacq gas field in southwestern France contains a very sour gas (16% H_2S and 10% CO_2). Some fields have gas containing up to 30% H_2S or CO_2.

H_2S is a poisonous gas. At 1-5 ppm of H_2S, people may experience nausea and headaches. When it reaches 20 ppm there is often eye and lung damage. Levels around 600 ppm are often lethal. Prolonged exposure to very low levels can also cause permanent neurological and physical problems.

Every time an engine stops and goes cold, sulphide or chloride condensation may occur. These acidic constituents severely corrode engine bearings, exposed copper and mild steel components. Most rubber seals will experience excessive hardening and subsequent failure, even at low concentrations of H_2S. It is therefore common to limit H_2S content to 200 ppm for most engines.

Mercaptans (or thiols) are organic compounds containing the group -SH bonded to the carbon atom in hydrocarbons. Mercaptans are less corrosive and less toxic than hydrogen sulphide. Tertiary Butyl Mercaptan (TBM) is widely used to make natural gas smell. Mercaptans are also a source of SO_2 during combustion though.

Sulphur content is generally low in fuels produced from biomass. Anaerobic digesters may, however, produce a gas with 40% CO_2 and 0.3 - 2% H_2S and mercaptans depending on the quantity of sulphur available in the raw material.

During combustion H_2S will combine with oxygen in the air to form SO_2, which can cause breathing problems, respiratory illness, or worsening of an existing respiratory disease such as asthma. SO_2 also damages crops and trees (see Chapter 2.2).

3.6 Alkali metal compounds, halogens, ash

Biomass fuels contain large quantities of alkalis in comparison with oil and natural gas. Volatile alkalis such as K and Na, but also S and Cl, interact with heavy metals such as Zn and Pb to form aerosols of some 0.1 – 1 μm in size. The aerosols form from nucleation processes as the hot combustion

products cool down. The condensate compounds will deposit on cold surfaces such as gas turbine vanes and blades, boiler tubes and downstream heat exchangers. This is detrimental to the efficiency of these components. The compounds are often highly corrosive as well.

Non-volatile compounds of Si, Ca and Mg are engaged in ash fusion as well as coagulation processes. Coarse ash structures, of some 10–100 μm will form. These particles are erosive and will destroy components subjected to high gas velocities such as gas turbine vanes and blades. In boilers and furnaces, ash may be removed from flue gases by filtration with baghouse filters or electrostatic precipitators. This is not possible in gas turbines. Alkalis, alkaline earths and halogens are therefore a major obstacle in gas turbine applications and will have to be limited before combustion.

4 Gas turbine combustor design

4.1 Turbulent premixed flames

The laminar flame seen in Figure 8 will normally not be encountered in a gas turbine combustor (see Chapter 4.16 for an exception). Flow conditions will instead be highly turbulent, since mixing of fuel and air, as well as reaction rates are greatly promoted by turbulence. The flame speed of a typical fuel under laminar flow conditions will be in the order of 0.5 m/s, while a turbulent flame will reach several m/s. The increase is due to wrinkling of the flame front, which thereby will exhibit a larger reaction front area.

The interaction between the flame front and the turbulence can be described with two parameters:

- turbulent length scale
- turbulent velocity fluctuation scale

This interaction is best described by the Borghi diagram seen in Figure 10.

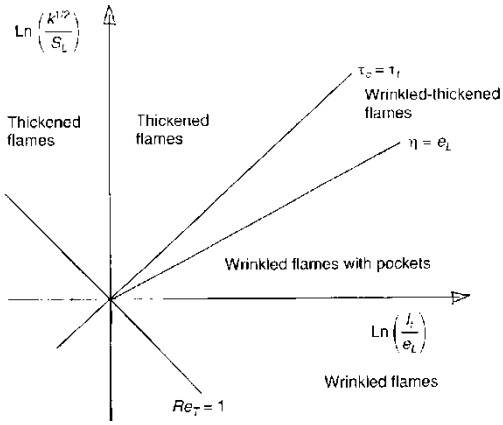

Figure 10: Borghi diagram [31]

Here the turbulent length scale l_t is scaled with the laminar flame thickness e_L on the abscissa. On the ordinate, $k^{1/2}$ (approximately the turbulent velocity) is scaled with the laminar flame speed s_L. To the right and below the abscissa there will be large-scale turbulence with the smallest eddies (at the Kolmogorov scale: η) still large enough not to interact with the inner structure of the flame front. The turbulence will only wrinkle and stretch the flame front. Further up, where $\eta = e_L$, small-scale turbulence will

start interacting with the flame front and thicken it. Premixed lean gas turbine combustion is generally considered to occur in this wrinkled-thickened regime. Above the line where $\tau_c = \tau_t$, wrinkled thickened flames will transition into thickened flames. Here, chemical timescales will be larger than the 'large scale turbulence' timescales.

4.2 Reactor and combustion modeling

Reactor and combustion modeling are good tools where the effects of residence time are important (such as in gas turbine combustion). There are (at least) four basic approaches:

- Perfectly Stirred Reactor (PSR)
- Plug Flow Reactor (PFR)
- 1-D Premixed Flame Code
- CFD

The PSR is characterized by having a uniform mixture at every point within the reactor. Reactants entering are considered to be instantly and perfectly mixed with the species already present. A swirl-stabilized primary zone of a diffusion-type combustor may be modeled in this way since this part of the combustor will have intense mixing and recirculation. A physical reaction coordinate would simply not make sense here, whereas an overall residence time may be defined (with some difficulty though). The PSR is best represented in the Borghi diagram (Figure 10) in the region high up and to the left.

For the portion downstream of the intermediate holes in the diffusion combustor, the flow will be more ordered. The equations may now have a physical reaction coordinate representing different positions along the combustor where local stoichiometry may be calculated. This will make it possible to study slow chemistry, such as CO burnout and thermal NO_X formation.

The third type of model has adaptations for the chemistry that takes place in the very thin reaction zone of laminar flames. This model will, in addition to the features offered by the PFR, add terms for thermal conduction and gradient diffusion of species.

All three models may contain terms that account for heat exchange with the surrounding walls.

CFD will be able to take into account the actual three-dimensional flow pattern within the combustor, as well as spatially varying degrees of

turbulence. The chemistry may be accounted for as detailed on-line kinetics, or as a pre-calculated flamelet library that will be matched to a scalar, which is computed throughout the domain. Paper 3 uses this latter approach in the Zimont TFC embodiment. A similar approach, still using a pre-computed chemistry library, is to use the Level Set G-equation [32], [33].

4.3 Combustor sizing

In general any type of industrial combustor shall be able to:

- operate on full load without excessive NO_X production and negligible amounts of CO and UHC
- be able to turn down without excessive amounts of CO and UHC
- ignite and relight easily
- operate without excessive combustion oscillations

In order to size a combustor to cope with these requirements, there exist two basic parameters [26], [34], [35]:

$$\Theta = \frac{\dot{m}}{P^{1.75} \cdot A_{comb.} \cdot D_{comb.}^{0.75} \cdot e^{T_{in}/300}} \tag{4.1}$$

$$\beta = \frac{\dot{m}_f \cdot \eta_c \cdot LHV}{P_{in} \cdot V} \tag{4.2}$$

Θ is the Combustor Loading Parameter (CLP). This parameter reflects the combustion stability or "the ability of the combustion process to sustain itself in a continuous manner" [35]. If the conditions inside the combustor become too lean or too rich, the reaction rates and the temperature inside the combustor drop and blow-out occurs. This is schematically illustrated in Figure 11. At high loading values the operating range between lean and rich narrows. The combustor loading parameter is derived assuming infinitely fast evaporation and mixing [26]. This is the case with premixed combustors. The pressure exponent in (4.1) is two for bimolecular reactions unhindered by limited mixing rates. For hydrocarbon reactions it has been experimentally determined to be 1.75 - 1.8. For the diffusion type combustor a value closer to unity is more adequate since mixing rather than kinetics is limiting. Here a similar, but not identical parameter to CLP may be used [26].

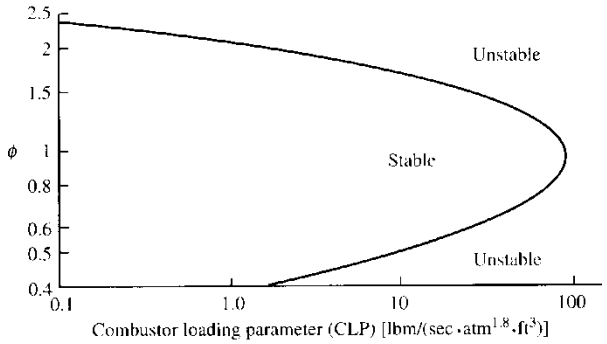

Figure 11: Equivalence ratio ϕ vs. Combustor Loading Parameter Θ [35]

It should be noted that different versions of the Θ parameter exist. There will also be different recommended limits depending on whether diffusion type, premixed combustors, full load or max altitude relight is discussed, so comparisons must be done with care. Figure 11 is also based on a simplified relationship where effects of the inlet temperature are omitted.

β, or Combustion Intensity (CI), is also a measure of the appropriateness of a design for combustion. It reflects heat release per unit volume. For gas turbines full-load combustion intensity should not exceed 60 MW/m^3atm [34]. In solid fuelled furnaces, where the fuel must first be gasified, this value is much lower (order of 0.1 MW/m^3atm).

Θ and β together will yield combustor diameter and length.

As pointed out in Chapter 4.1, a turbulent premixed flame will have a higher flame speed due to increased surface area (until quenching effects start to dominate). Combustors operating at different levels of turbulence will therefore have different average consumption rates of fuel and therefore need to be sized differently. This is not accounted for in the Θ or β parameters.

Combustor loading is reported in Paper 4 and 5. Combustion intensity is shown in Paper 5.

4.4 Diffusion combustion

Diffusion combustion is the simplest and most abundant type of combustion process. Here the fuel and the oxidant enter separately into the combustion volume. Combustion takes place where there is a suitable mixture of the two. Combustion will essentially progress at stoichiometric conditions. For high calorific fuel types this will result in very high combustion temperatures in the order of 2400K (depending on fuel type

and initial temperatures of reactants). This will yield high quantities of thermal NO_X production when the fuel is oxidized by air.

The biggest advantage with diffusion-type combustors is that they are very stable in terms of blow out, since there will always be stoichiometric regions regardless of overall stoichiometry. This will also mean better fuel flexibility when compared with premixed concepts. Diffusion-type combustors are also generally less susceptible to thermo-acoustics when compared with LPP combustors (see Chapter 4.5 and 4.7).

If the fuel contains large quantities of inerts, combustion temperatures may be low enough, to not form excessive amounts of thermal NO_X (see Paper 1). For this case, a gas turbine combustion system should have this type of combustor since it offers several advantages over competing types.

A typical diffusion type combustor for a gas turbine may be seen in Figure 12.

The combustor is divided into three separate zones; primary, intermediate and dilution zone. Each zone's individual task is to:

- stabilize/anchor the flame and oxidize a good portion of the fuel. Significant quantities of CO and H_2 will still be unburnt (~2400K, η_c~90%)
- reduce the temperature of the combustion products to eliminate dissociation products (mainly CO) and to burn out soot (~1800K)
- further reduce the temperature of the combustion products to suit the requirements of the turbine (~1400K–1700K)

Temperatures will vary considerably within the primary zone. At some locations where air is admitted, temperatures are essentially equal to compressor outlet temperatures. At other locations, where stoichiometry, turbulence and temperature allow combustion, stoichiometric temperatures may be reached. This will, however, be modified by re-entrainment of hot gases; which act like EGR in piston engines, but also by turbulence.

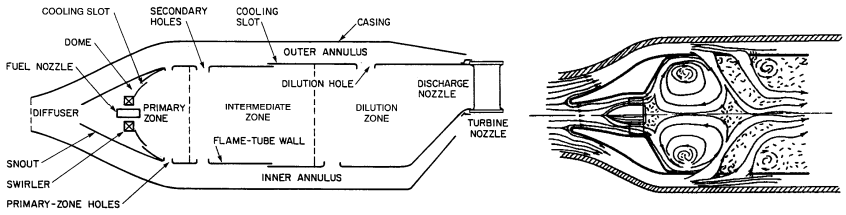

Figure 12: Diffusion type combustor [26]

Since the reactants need an induction time before ignition and high levels of turbulent shear will quench combustion, turbulence can to some extent mix air and fuel before combustion. Therefore diffusion-type combustors may to some extent also be partially premixed (see discussions on quenching in Chapter 4.11 and Paper 3).

Most of the thermal NO_X will be produced in the high temperature zones of the primary zone. Since this is a fairly slow process, a short primary zone is of the essence. Residence time selection is, however, inevitably a trade-off between NO_X production at full load and CO/UHC production at turn-down conditions. Typical primary zone residence times for diffusion type combustors are therefore 1.5–2 ms. This will correspond to an $L/D \approx 1$ for tubular combustors. Intermediate zone residence times are also in the order of 1.5–2 ms.

Often times, cold regions that propagate through the combustor will also carry large amounts of CO. A typical source of cold regions is also invasive flame-tube cooling which has to be carefully designed in order to not produce CO. Non-invasive cooling is therefore preferred where possible.

Invasive cooling may also be a problem in liquid spray combustion. The reason for this is that droplets can end up near walls, where they may burn at stoichiometric conditions and overheat the metal part intended to be cooled.

A typical diffusion-type combustor burning natural gas may produce 70–150 ppm NO_X and 10-50 ppm CO. On liquid fuels, such as diesel, these numbers will be higher, sometimes as much as double the amount.

4.5 Premixed combustion

In order to reduce the amount of thermal NO_X produced in conventional diffusion type combustors, several techniques have been tried. The preferred method for the last 15 years or so has been Lean Premixed Combustion, and in the case of liquid combustion, Lean Prevaporized Premixed Combustion. Other common terms are Dry Low NO_X (DLN) or Dry Low Emission (DLE) combustion.

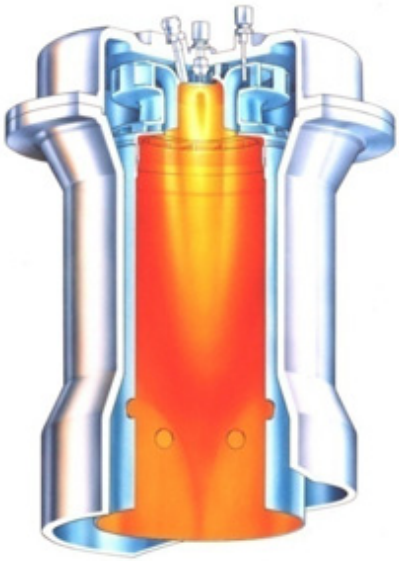

Figure 13: The Volvo LPP concept

In an LPP combustor, fuel and air is pre-mixed in a mixing device prior to injection and combustion. By having a uniform and lean mixture the peak combustion temperatures can be kept lower. Less thermal NO_X will therefore be produced. A typical LPP combustor can be seen in Figure 13.

In the LPP concept there is no intermediate zone. Instead the fuel mixture entering the primary zone is such that the combustion temperature will not exceed approximately 1800K. This is achieved by having an equivalence ratio in the order of 0.5 for HCV fuels. As more inerts are introduced in the lower calorific gases, ϕ will approach unity for a fixed combustion temperature. When ϕ reaches unity for the design point (full load), the LPP concept is no longer viable.

In gas turbines with fixed geometry for the combustion and dilution air, the equivalence ratio will decrease when turning down to part-load conditions. Since the device is already running lean on full load, problems with lean blow out will typically arise. In order to sustain combustion at part-load conditions, a diffusion type pilot combustor is often incorporated. This device, a.k.a. the primary combustor will supply heat (and to some extent, radicals) to the premixed combustor (secondary combustor), which will therefore be able to operate at leaner conditions.

The combustion process, i.e. evaporation, heat up of reactants and oxidation takes place at a lower temperature in the LPP combustor compared with the primary zone of a diffusion type combustor. Chemical

kinetics will therefore be much slower. For this reason, the residence time in the primary zone needs to be in the order of 8 ms at a minimum. This will set a lower limit for the length of the primary zone. The residence time usually does not change much on part-load because the normalized flow (acc. to formula 4.3) doesn't change much on part-load.

$$NF = \frac{\dot{m}\sqrt{T}}{P} \tag{4.3}$$

where $\dot{m}$ is the mass flow, T is combustion bulk temperature and P is combustor pressure. It is however customary to evaluate residence time as a function of load when designing a new combustor.

It is important to properly mix the incoming reactants and stabilize the flame. These processes are associated with pressure losses, which should be kept to a minimum since they will be detrimental to the performance of the gas turbine in terms of power output and thermal efficiency.

Pressure losses will also come from annuli flow to the premix module and hot loss which is inevitably a result of the flow acceleration which takes place within the combustor as the high-density reactants are turned into low-density products. Pressure losses may also be required in order to provide cooling (i.e. impingement cooling). A typical range is 3.5–5% of the available compressor discharge pressure, where the latter number is considered unduly high, especially in diffusion-type combustors. The subject of combustor pressure loss is discussed in Paper 4 and touched on in Paper 5.

A portion of the combustor pressure drop is used to anchor the flame by creating a recirculating flow pattern at the injector outlet. Flame anchoring is an extensively researched topic in the field of gas turbine combustor design [36], [37], [38], [39]. It is especially important for LPP combustors, since these are operating close to LBO and nowhere within the combustor will there be stoichiometric pockets present which will maintain combustion. HCV LPP combustors will typically be designed to operate at primary zone AFR≈30 at full load conditions but blow out at AFR≈40 as the turbine is turned down. Control over recirculation of hot products, which ignites the fresh mixture entering, is therefore essential and much effort is usually devoted to flow characterization in the primary zone during the development phase. It is not uncommon to start out with water tunnel tests, followed by atmospheric rig tests and pressurized tests on single cans or sectors, before running a new design in an actual gas turbine. Diffusion type combustors may, in contrast, operate reliably at primary zone overall AFR in excess of 1000 for pressure atomizers. Airblast atomizers which provide

better mixing may be limited to AFR≈250 [26]. This, together with thermo acoustics and flashback concerns at high combustor inlet temperatures, is why the diffusion-type combustor has been so difficult to replace with DLE burners in the aviation industry, where reliable operation at widely varying operating conditions is paramount. Efforts are being made, though.

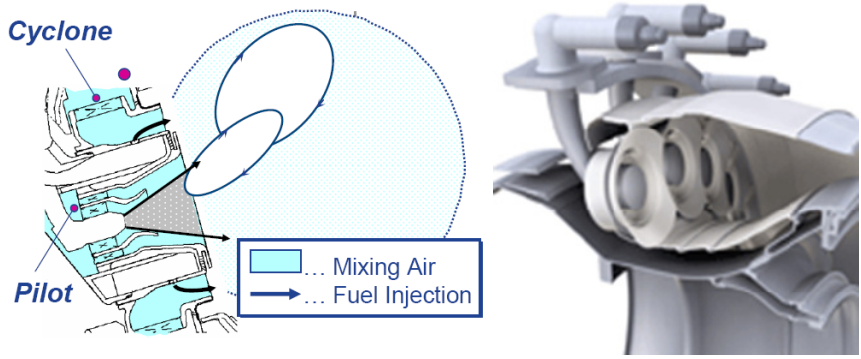

Figure 14: GE TAPS combustor [GE Web]

The Twin Annular, Pre-mixing Swirler (TAPS) combustor from General Electrics, shown in Figure 14, is such an example. Most notable in this design is perhaps the lack of dilution holes. This is typical of LPP combustors followed by turbines with advanced blade cooling concepts allowing high gas temperatures. The idea here is to have a set of pilot flames that stabilize an annular lean main flame.

An interesting concept, which may become common in future gas turbine installations, where part-load emission performance is important, is where the amount of air admitted to the primary zone can be controlled on part-load. This allows the combustor to operate at essentially a fixed equivalence ratio. Thus a larger operating window for low emissions is obtained. Care must be taken, however, in the design of such a system so that the combustor pressure drop does not increase unduly as the air-flow to the primary zone is gradually blocked off (when turning down). Figure 15 shows an example of an arrangement with varying pressure drop, while Figure 16 shows a design that concurrently reduces area to the primary zone and opens up area at the combustor exit. Here, the optimum tradeoff between NO_X and CO production is selected by a control algorithm based on CO measurements. The diverter valve position and compressor inlet guide vane position are used as control mechanisms. Solar Inc.™ claims sub 5 ppm NO_X in the 40-100% load range at fixed 10 ppm CO with this concept. The fuel injector uses axial swirlers and a backward-facing step to anchor the flame. In contrast, the SGT-600 control algorithm for the bypass

valve is based on an open loop computation of the "firing temperature" in the combustor. One difficulty with these 'variable air' concepts lies in maintaining suitable radial temperature profiles for the following turbine.

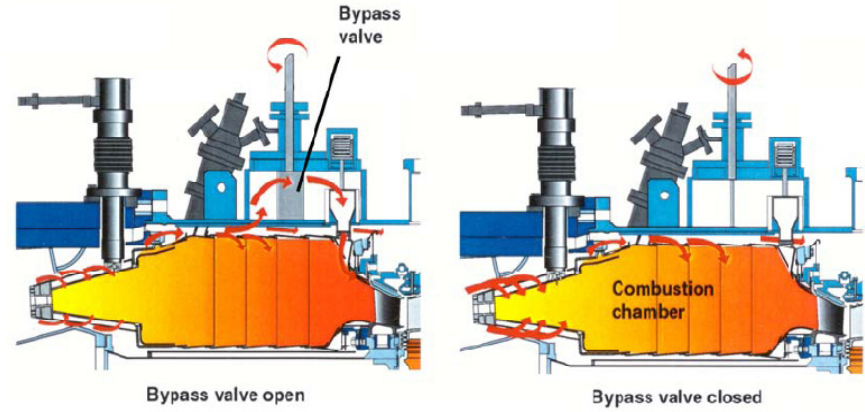

Figure 15: Primary air management for the Siemens SGT-600 [40]

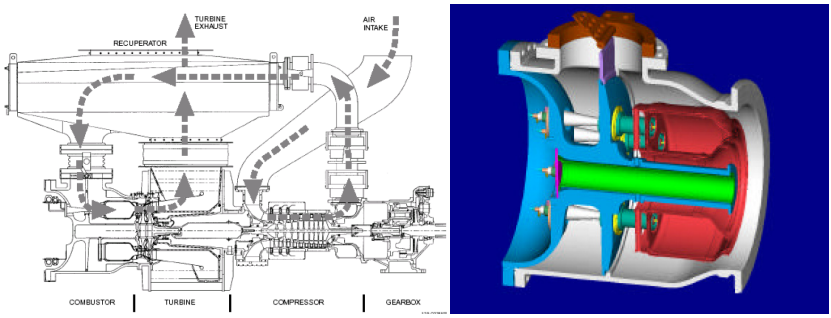

Figure 16: Primary air management for the Solar Mercury 50 combustor [41]

4.6 Swirl stabilization

It has already been mentioned that in order for the combustor to operate stably over a wide range of operating conditions, fresh gases must be re-lit by the hot combustion products. Swirl stabilized combustion is the preferred method of achieving this in the gas turbine industry. It is used both in diffusion and lean combustors. Oftentimes swirl in the primary zone is set up quite differently in the two cases though. In both cases, swirlers at the head of the combustor impart a tangential momentum on the air (Figure 17b). In the case of the diffusion combustor, much less air enters at the head compared with the premixed combustor. Diffusion combustors, however, benefit from primary dilution holes which provide a radial inward flow approximately one combustor diameter downstream of the head end (Figure

17a). It is therefore quite common to combine the effects from swirl and the primary air jets to create a compact recirculation zone with high mixing rates and good stability over a wide range of operating conditions (Figure 17c).

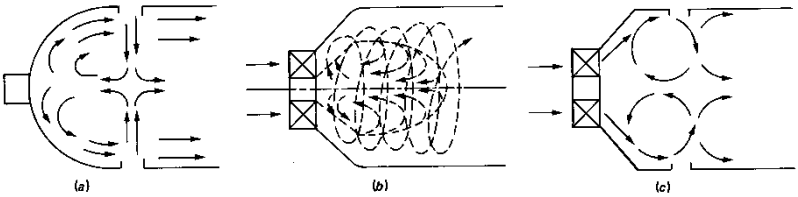

Figure 17: Primary zone flow patterns, **a**) opposed primary jets, **b**) swirl stabilization, **c**) combined flow [26]

Premixed combustors, on the other hand, have most of the primary air admitted through the premixer. They also lack primary holes. It is therefore preferred to inject the mixture axially, but with a higher swirl component imparted by swirlers within the premix module (Figure 17b). Depending on the strength of the swirl component in relation to the axial component, quite different flow patterns may emerge. In order to quantify the relation between tangential and axial flow, the swirl number is introduced [26]:

$$S_1 = \frac{G_t}{RG_a} \tag{4.4}$$

where R is the radius of the swirler. G_t is the axial flux of tangential momentum and G_a is axial flux of axial momentum (thrust). These may be calculated as follows:

$$G_t = 2\pi \int_0^R \rho W U r^2 dr \tag{4.5}$$

$$G_a = 2\pi \left(\int_0^R \rho U^2 r dr + \int_0^R p\, r dr \right) \tag{4.6}$$

where ρ is the density, U is the axial velocity, W is the tangential velocity and p is the static pressure.

Sometimes the pressure term in Equation (4.6) is omitted. This leads to a simplified expression involving only tangential and axial bulk velocities W_b and U_b:

$$S_2 = 0.75 \frac{W_b}{U_b} \tag{4.7}$$

For unconfined flow, the swirl number must be larger than 0.6 in order to obtain flow reversal in the core. The effect of having a downstream contraction is that flow reversal starts at a lower swirl number.

There exist a couple of well-known principles for flame stabilization in LPP combustors. Most concepts rely on a set of air swirlers and a premix duct combined with a step expansion. An example of this concept is shown in Figure 13. A related concept is the Alstom (A)EV concept, seen in Figure 18. Instead of swirlers, a cone with tangential slots is used to impart tangential momentum. The secondary fuel is admitted adjacent to the slots. The two will mix inside the cone and combustion will take place when the vortex that forms inside the mixer cone breaks down at the exit. Siemens guarantees 25 ppm NO_X on gaseous fuel in the 80 -100% load range for the SGT-600 with the 2nd generation burner. The 3rd generation burner with a 4-slot cone and an added mixing tube is claimed to reach 15 ppm NO_X and CO on gaseous fuel in the 50 – 100% load-range. This burner is now standard in the 29 MW SGT-700 (formerly GT10C) and 45 MW SGT-800 (formerly GTX100) [40].

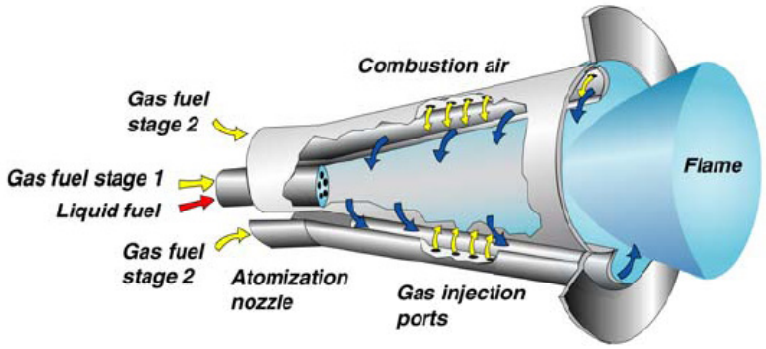

Figure 18: Alstom 2nd generation burner for the Siemens SGT-600 (formerly GT 10B) [40]

4.7 Combustion oscillations

For a long time gas turbine combustors were of diffusion type, i.e. where fuel and oxidizer meet inside the combustion chamber. In this type of combustor, combustion takes place where the two meet provided that enough heat is supplied to sustain the chemical reactions. This type of combustor is very stable in terms of combustion oscillations as the position of heat release is essentially dictated by the position of the fuel/oxidizer interface.

Problems with thermoacoustics started with the advent of lean premixed combustors. Here there is no interface between fuel and oxidizer in the combustion chamber. Instead, the two are mixed in a premix tube. The flow velocity is kept higher than the turbulent flame speed of the mixture in order to avoid flashback. After the premix duct, the mixture is

dumped into the combustor where velocities drop rapidly. Combustion will take place where:

- stoichiometry allows
- strain rates are sufficiently low
- temperatures are sufficiently high
- sufficient amount of radicals are present
- turbulent flame speed matches flow field velocities

Several of these criteria may be strongly modulated by thermoacoustics. For instance, if a pressure wave is allowed to travel to the premix duct, air- or fuel-supply may change. This will affect stoichiometry, flame temperature and turbulent flame speeds. The flame front may, as a result, shift position and in doing so induce another acoustic pressure pulse.

Rayleigh formulated a criterion for positive feedback [42]:

"If heat be given to the air at the moment of greatest condensation, or be taken from it at the moment of greatest rarefaction, the vibration is encouraged. On the other hand, if heat be given at the moment of greatest rarefaction, or abstracted at the moment of greatest condensation, the vibration is discouraged."

In integral form this may be written [43]:

$$k \int_V \int_T p'(\mathbf{x}, t)\dot{q}'(\mathbf{x}, t)\, dt dV \geq \int_V \int_T \sum_i L_i(\mathbf{x}, t)\, dt dV \qquad (4.8)$$

where k is a (dimensional) constant [44], p' is the instantaneous pressure fluctuation as a function of position and time, and $\dot{q}'$ is the instantaneous heat release rate per unit volume as a function of position and time. V is the combustor volume and T is the time of one period for an oscillation of a given frequency. Wherever the pressure pulse and heat release pulse are less than 90° out of phase, the left integral will be positive and the thermoacoustic feedback mechanism will be reinforced.

On the right hand side energy loss is represented as L_i where L_i may be e.g. viscous dissipation, radiation and acoustic dissipation [43]. Dilution holes and film cooling holes may provide substantial damping. When the forcing energy supplied to the cavity matches energy dissipation, amplitudes will stop growing. This is the equal sign in Equation (4.8).

There may be various sources for excitation of particular frequencies stemming from the premixer module e.g.:

- precessing vortices
- turbulence generated within the premixer
- wake von Karman instabilities
- sheer layer Kelvin-Helmholtz instabilities

At times very small modifications to the geometry of the injector module can have a large impact on thermoacoustics.

If possible, passive damping may and have been used commercially. Quarter-wave tubes or Helmholtz resonators may be connected strategically to the combustor. This is a fairly inexpensive option as it is, in its simplest form, only a tube closed at one end. Quarter wave tubes are used e.g. on the GE LM6000 DLE.

Active damping may be used to break the feedback loop. The most common approach is to modulate the fuel supply using a fast valve for a small portion of the total fuel flow. This is complicated and expensive.

4.8 Tubular vs. annular

There exist two basic types of gas turbine combustion chambers:

- annular (Figure 19 left)
- tubular (Figure 19 right)

There are distinct advantages and disadvantages with each type. The annular type makes better use of the available space and is generally lighter. It is therefore preferred in aircraft propulsion where a small cross section and low mass is important. For industrial engines this is less important and one or several can combustors may be used. The main driver for using several identical can combustors is that development is simplified and substantially less costly since it may be performed on only one combustor. Can designs will have a set of identical components that will be smaller and generally more robust, especially for low pressure-ratio designs. Large engines and aero derivatives will generally have high pressure-ratios and therefore relatively compact combustors, so it makes less sense to split them into individual cans with potentially more surface area to cool, especially since these engines tend to have very limited supply of cooling air, too. Annular combustors will also be simpler to ignite since cross-ignition tubes or individual igniters for each combustor are unnecessary. A hybrid design, where separate combustion chambers dump into a common annular turbine inlet duct, is also used in

some designs. One major drawback of annular designs is that service and retrofitting of hot parts usually involves a complete teardown of the engine. In terms of combustion acoustics, the can concept is preferred since there will be less scope for interaction between individual, or groups of burners.

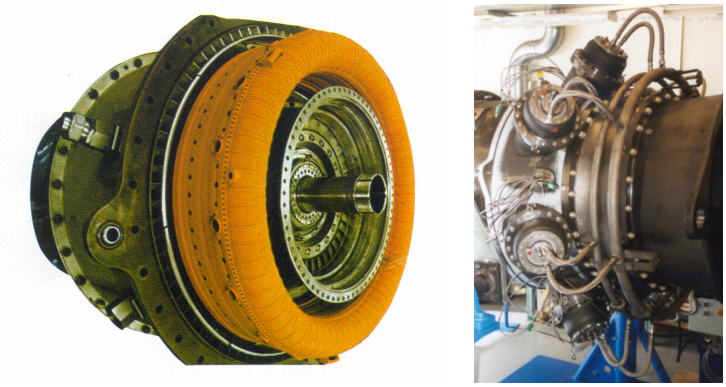

Figure 19: Volvo VT4400 annular diffusion combustor left and seven can LPP combustor right.

4.9 Wet combustion

Wet combustion was perhaps the first step towards limiting the amount of NO_x formation in diffusion type combustors in gas turbines. Merely adding liquid water to the combustor will, however, reduce the thermal efficiency of the gas turbine since heat will be required to vaporize the water. Shaft power will increase though, due to the increased mass flow and higher heat capacity seen by the turbine(s).

In the early days (1940s), water was injected at the compressor inlet of a gas turbine in order to reduce compression work and increase mass flow through the turbine. Reduced NO_x emissions were at these times merely serendipitous. In order to raise power output and thermal efficiency, especially on part load, exhaust heat was later recovered through the insertion of a Heat Recovery Steam Generator (HRSG) at the exhaust, followed by injection of the steam into the combustion section. This is the STIG cycle, and in its more advanced form the Cheng cycle that was commercialized in 1982 [45].

The addition of water into the combustor, regardless of method, will raise c_p. This will lower combustion temperature for a given fuel supply. For a given Turbine Inlet Temperature (TIT), combustion will progress in a more diluted environment and peak temperatures will be reduced due to the lower peak combustion temperature of the reactants. It has also been argued that the water interacts with oxygen radicals to form OH radicals, which are

less efficient in attacking the N_2 molecules in the air [11]. Adding water is for these reasons an efficient method for NO_X reduction.

Water may be added to the air stream or the fuel stream. Adding water to the fuel stream is preferable since this will guarantee that all the water will have to pass through a reaction front. In Cheng et al. [46] it was demonstrated that a diffusion flame producing ~60 ppm NO_X without steam injection can be modified to produce 2 ppm NO_X with a steam/fuel ratio=4, -while CO is kept in the single digit range.

Besides being more complex than simple cycle gas turbines, "wet cycles" inevitably require extremely clean water in order to not foul injector passages and destroy downstream blading. Since the water is normally not recovered from the exhausts, a constant supply is required. This will add to the operating costs of the installation, hence the desire to have semi-closed cycles where the water is recovered from the exhaust gases. This is what the EvGT cycle with a flue gas condenser does [47], [48]. The EvGT cycle will, however, have the water ballast carried as humidified air which is not ideal from an emissions perspective when operating on HCV fuels. It would, however, be possible to add an HRSG to the EvGT and inject parts of the water as steam/fuel mixture rather than as humidified air directly into the combustor. The subject needs further study, though.

Combining an LPP combustor with water or steam injection seems less ideal since both techniques on their own are capable of creating sufficiently low combustion temperatures required for low NO_X combustion.

4.10 Trapped Vortex Combustion (TVC)

The Trapped Vortex Combustor (Figure 20), or TVC, was pioneered by Wright Aeronautical Research Laboratories. It is mainly seen as a means to create relatively simple, compact combustors for supersonic military aircraft, but efforts have been made to introduce the concept in industrial gas turbines (ALM Turbine, Inc.). The trapped vortex combustor maintains a high degree of flame stability because the vortex trapped in a cavity provides a stable recirculation zone that is protected from the main flow of the combustor. The cavity serves as a pilot flame and provides a continuous ignition source for the main combustor, helping to keep the flame lit throughout the operating envelope. This interaction between the cavities and main combustor significantly enhances mixing, allowing for a short-length, compact combustor. The low NO_X emissions are primarily the result of improved fuel and air mixing in the cavity at the front end of the main combustion zone [49].

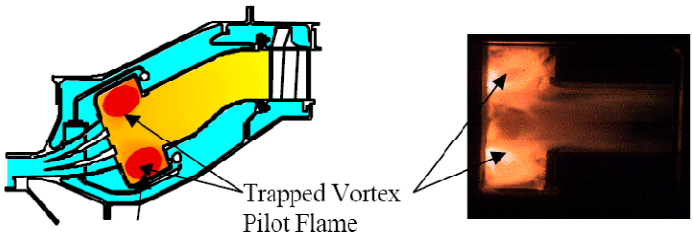

Figure 20: Trapped Vortex Combustor [49].

4.11 Bluff body stabilized combustion

Bluff body stabilized combustion is mainly used in aviation propulsion where a temporary boost of power is required. Typical examples would be in afterburners of supersonic transport at takeoff and when going supersonic. It is, however, most prolific in jet fighter engines such as the one shown in Figure 21. In this image it is the red ring and struts at the inlet of the tailpipe which form the flame-holder. The addition of extra heat behind the gas generator will raise the exhaust temperature and therefore the volumetric flow. For the afterburner to work efficiently a variable geometry convergent-divergent nozzle is fitted at the back end.

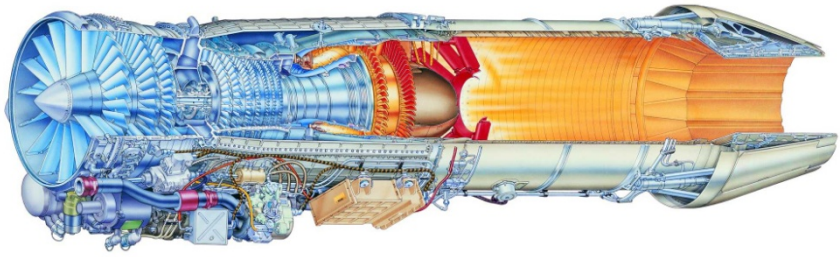

Figure 21: The RM-12 engine for the JAS-Gripen

A detail of the arrangement can be seen in Figure 22. The gas flow coming out of the turbine will vary in pressure, velocity and temperature. Typical values would be 0.5 to 5 bar(a), 1100K and 180 m/s (Ma=0.25). Direct combustion in those conditions is clearly not possible. A flame would simply be advected out through the tailpipe at those velocities. Flame-holders are therefore introduced after the fuel bars in order to reduce the velocity, recirculate hot gases and thereby ignite fresh gases. The simplest and most proven shape that does this is the triangular flameholder. It presents a reasonably aerodynamic shape to the flow, provides a large, fairly stable wake zone while being light and having little surface area to cool.

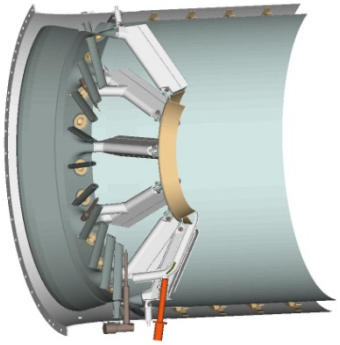

Figure 22: Fuel bars and flame holder arrangement

Upstream of the flameholder the fuel is injected with a multitude of fuel bars. Each fuel bar contains several holes which admit the liquid fuel perpendicularly to the gas flow. This is the LJIGCF (Liquid Jet in Gas Crossflow) situation described in Chapter 6.6. Weber numbers (defined in chapter 6.1) are typically in the range 300–2500 depending on nozzle sizing and operating conditions. In the space between the fuel bars and the flameholder the fuel and gas generator efflux will mix. The fuel coming out as droplets is vaporized and further gas phase mixing will ensue. Combustion in the wake of the flameholder will therefore be premixed. Cold bypass air is used to cool the arrangement. Staging is sometimes considered in order to maintain combustion near stoichiometric conditions at different points in the flight envelope. Flame holder blockage is typically 30%. Design point pressure loss will be 5–7% plus 5–10% hot-loss [34]. Burning length will be 0.9–1.3 m typically and desired heat release is 80 $Wm^{-3}Pa^{-1}$ [50] i.e. somewhat higher than for the primary combustor.

Flame holding has certainly been extensively studied, but much of the work is classified, since it is so tightly coupled to military aircraft propulsion. Volvo Aero has, however, provided data from their 'Validation Rig 1' which is described in Paper 3. This data set has been used extensively in the research community; see [51] and references given in Paper 3.

Figure 23 shows the axial velocity profile and Figure 24 shows the temperature profile from the k-ω computations in Paper 3. Behind the bluff body, the recirculation zone is visible as the dark blue area. Further downstream the velocity is seen to increase as the cold reactants are heated when passing the reaction zone. It is seen in Figure 24 that the flame front starts out as a thin reaction zone at the dump edge of the flame holder. Further downstream the reaction zone gradually thickens. The flame front is, however, on average stationary. The flame is therefore called a "stationary developing flame". It turns out that premixed flame fronts can be described with just one non-dimensional reaction coordinate ξ, being normalized with local flame thickness δ_t:

$$\xi = \frac{x - x_f}{\delta_t} \tag{4.9}$$

Here x is a coordinate that traverses the flame front and x_f is the flame front position. Any scalar which describes the flame structure; such as temperature, density or species concentration will, if plotted vs. ξ and scaled properly, collapse into one curve regardless of fuel type, equivalence ratio, turbulence properties, state of development etc. [51]. It is therefore tempting to simplify the analysis and compute just one progress variable c [0, 1] for the domain and put all the scalars in a pre-computed library which relates each of those quantities to c. This is the flamelet library approach. c=0 will here mean always completely unburnt and c=1 will mean always completely burnt.

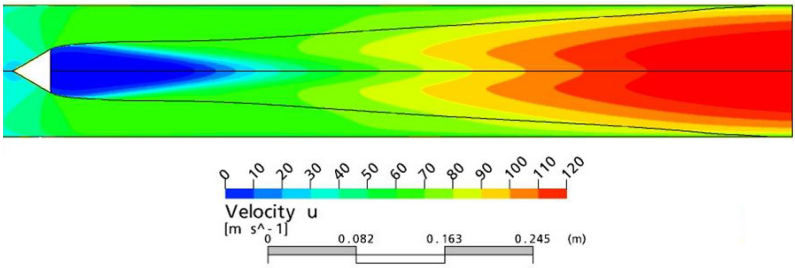

Figure 23: Axial velocity distribution behind flame holder

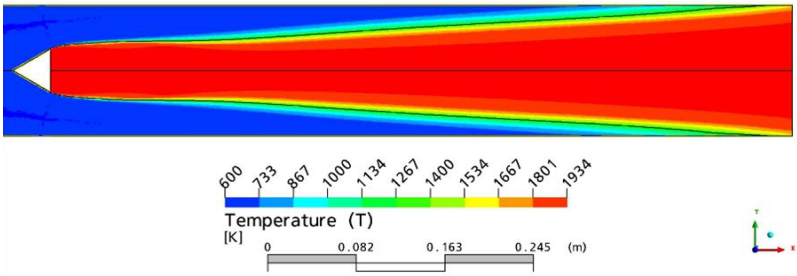

Figure 24: Temperature distribution behind flame holder

Other quantities like velocities, turbulence, temperature and density need to be solved concurrently with c. This is normally done in a CFD-code and the most common approach is to use the Reynolds Averaged Navier-Stokes approach or in the combusting case, Favre averaged Navier-Stokes. In addition to the transport equations for momentum and energy, a turbulence model is needed. Many such models have been proposed, each with some advantages and disadvantages. The most popular ones in the industry are the two-equation models. For a comprehensive review of these see e.g. Wilcox [52].

It remains to compute c in the domain. Zimont et al. [53] proposed the combination of a transport equation (Equation (4.10)) for c and a turbulent flame speed model (Equation (4.11)) to close the transport equation.

$$\frac{\partial(\bar{\rho}\tilde{c})}{\partial t}+\frac{\partial(\bar{\rho}\tilde{u}_j\tilde{c})}{\partial x_j}=\frac{\partial}{\partial x_j}\left(\frac{\mu_t}{\sigma_c}\cdot\frac{\partial\tilde{c}}{\partial x_j}\right)+\rho_u s_t|\nabla\tilde{c}| \tag{4.10}$$

$$s_t = AGu'^{3/4}s_l^{1/2}\lambda_u^{-1/4}l_t^{1/4} \tag{4.11}$$

In Equation (4.10) the terms are from left to right:

- transient
- convective
- diffusive
- source

The diffusive term will scale with turbulent viscosity μ_t and diffusivity through σ_c. This term will provide for the developing nature of the flame.

The flame speed model will respond to turbulence through the dependence on the turbulent velocity u′ and turbulent length scale l_t. The stretch factor will reduce the turbulent flame speed in situations of high strain rates. This is modeled through G viz:

$$G=\frac{1}{2}\operatorname{erfc}\left[-\frac{1}{\sqrt{2\sigma}}\left(\ln\frac{\varepsilon_{cr}}{\tilde{\varepsilon}}+\frac{\sigma}{2}\right)\right] \tag{4.12}$$

where erfc is the complementary error function.

G is the probability of having an unquenched flame. It is obtained by integrating the log-normal distribution of the turbulent dissipation rate ε.

Here:

$$\sigma=\mu_{str}\ln\frac{l_t}{\eta},\ \eta=\frac{\nu^{3/4}}{\varepsilon^{1/4}},\ \varepsilon_{cr}=15\nu g_{cr}^{\ 2}\ \text{and}\ l_t=\frac{k^{3/2}}{\varepsilon} \tag{4.13-16}$$

where σ is the standard deviation, μ_{str} is an empirical model constant (0.28), η is the Kolmogorov length scale, ν is the kinematic viscosity and k is turbulent kinetic energy.

g_{cr}, the critical quenching velocity gradient must be tuned for the application at hand. In the case investigated here this parameter proved to make small differences when changed within the range suggested by ANSYS Inc. for their implementation in CFX (see Paper 3).

The flame speed model will respond to changes to the thermal diffusivity through λ_u too. This quantity is temperature- and pressure-sensitive.

The Zimont model was used in Paper 3 to investigate how the CFX implementation would work when applied to bluff body combustion, and to find some recommendations regarding choice of turbulence model. The paper also tries to shed some light on what the most likely overall turbulent flame speed really was in the conducted experiments. There has been some uncertainty regarding flame position due to flashback in the wall boundary layers [32]. It also discusses difficulties when using RANS models on problems with periodic fluctuations, and suggests that this may be present in the experimental data.

It should be mentioned that many other combustion models exist besides the Zimont model. The subject of combustion and turbulence interaction is well described by e.g. Peters [54].

As mentioned before, available research on bluff body combustion is scarce. One idea worth mentioning seems to focus on reducing the inherently high drag from the triangular flame holder and creating a more stable flow pattern in the wake. Yang et al. [55], [56] suggest an open-slit V gutter according to Figure 25 and found that the flow field in the wake became asymmetric. This was explained with the Coanda effect. This device was reported to provide less drag through better pressure recovery and wider stability limits. The tests were however not performed at realistic Reynolds numbers.

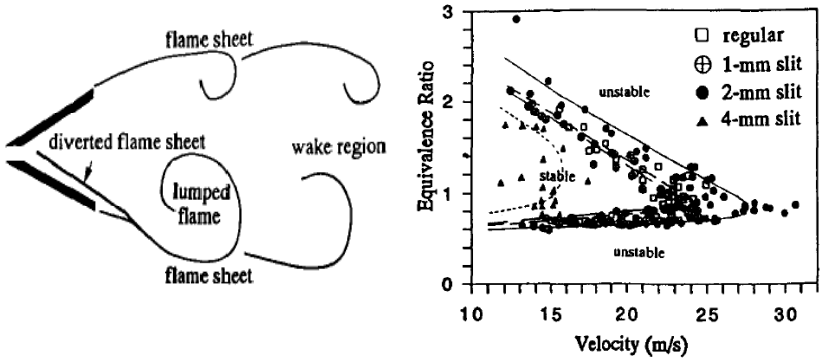

Figure 25: Flow field behind open-slit V gutter and stability limits [55]

4.11.1The DESS rig afterburner

The DESS rig (described in Chapter 7.2) was used for the spray papers 8 and 9. It was originally planned to use Jet A1 aviation kerosene or LeanJet from EcoPar AB for the spray tests. These are combustible and in the case of Jet A1, quite odorous. It was therefore necessary to incinerate the spray vapors in the afterburner, being located downstream of the test section, but prior to exhaust. The NG fuelled afterburner lacked flame holding and primary zone. It was therefore necessary to design a flame holder and a flame tube and test the equipment. The afterburner prior to rebuild can be seen in Figure 26.

The original design was limited to 200 kW heat input from afterburner 'NG fuel' + spray. This was extended to 1.1 MW in order to reach 830°C incineration temperature at maximum rig air-flow (1.1 kg/s) with no air pre-heat. In order to keep the afterburner cooling air separate, a water-cooled flame tube was designed. Thus only rig air was held at the incineration temperature. The residence time was set to minimum 15 ms yielding a flame tube with ∅490 mm and L=900 mm.

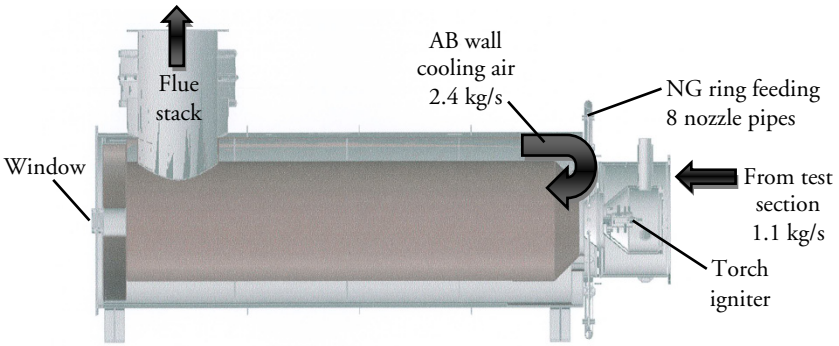

Figure 26: DESS afterburner prior to rebuild

The flame holder is of an open V-gutter type and contains 8 arms. For each arm there is a radial NG fuel feed nozzle pipe. The eight radial nozzle pipes can be seen in Figure 28 and Figure 29. Each nozzle pipe feeds NG into the bottom of the V-gutter. Three different hole patterns were evaluated before satisfactory flame holding was achieved. The final hole pattern is shown in Figure 29.

The flame holder is ignited by hot gases from a propane-fired torch igniter shown in Figure 26. The hot gases are led to the tip of each nozzle pipe with the centrally located pipe shown in Figure 27 (right).

Figure 27: Flame holder seen from downstream (left) and upstream (right)

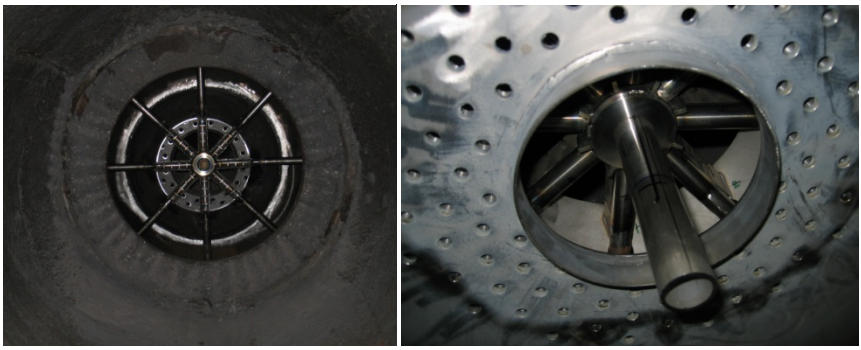

Figure 28: Assembled flame holder seen from downstream (left) and upstream (right). Flame tube is not shown

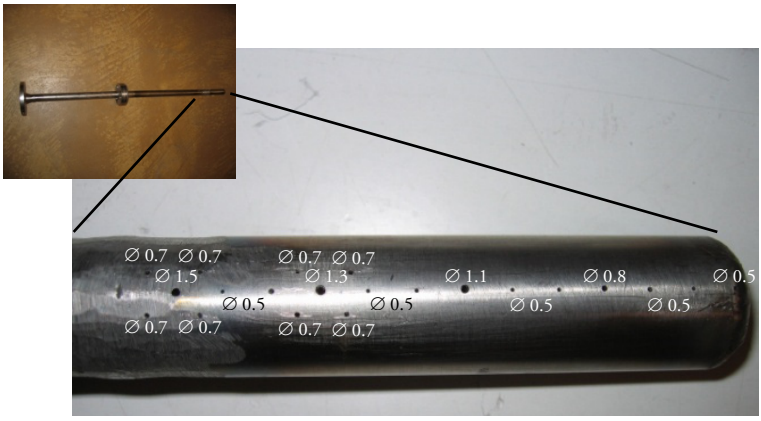

Figure 29: NG nozzle pipe final hole pattern (dimensions in mm)

Figure 30 shows the afterburner operating at 850°C with 300 g/s air from the rig. The INOR TKS15 thermocouple seen glowing red was used to control the afterburner.

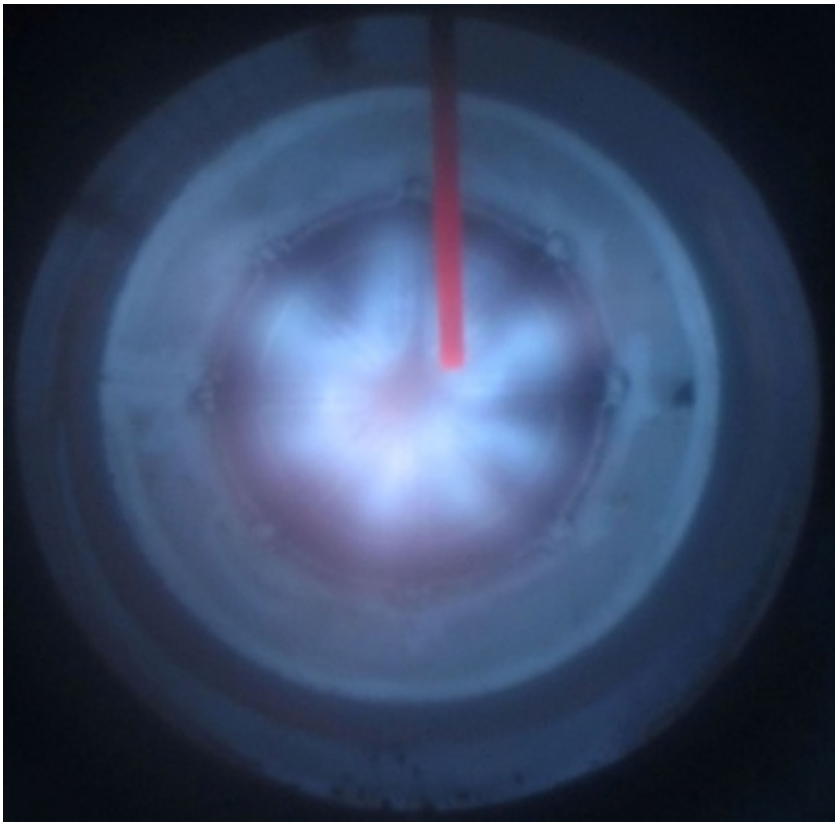

Figure 30: Afterburner operating at 850°C and 300 g/s air flow as seen through window indicated in Figure 26

The modified afterburner performed according to expectations. Due to other problems with the rig, tests with fuel sprays were abandoned in favour for water sprays (see Papers 8 and 9).

4.12 Rich burn, Quick quench, Lean burn (RQL)

NO_X emissions from the thermal NO_X mechanism are avoided if high temperatures are avoided in the combustion chamber. This is possible at both the lean and rich sides of stoichiometric combustion. Figure 31 shows that if the equivalence ratio in the primary zone is set at approximately 1.5, NO_X emissions may be on par with DLE. The products coming out of the rich zone will be partly oxidized and therefore contain large quantities of hydrocarbons, and CO. In addition, parts of the air- and fuel-bound nitrogen will be converted to other nitrogenous compounds. At ϕ=1.4 mostly NO will form. As ϕ is further increased, HCN will start forming. NH_3 will be seen at even richer conditions. The sum of concentrations of all

nitrogen species other than N_2 is expressed in TFN (Total Fixed Nitrogen) [57]. In rich-lean combustion, the TFN concentration exiting the rich primary zone largely determines the degree of NO_X emission downstream of the lean zone. Between the rich zone and the lean zone a mixing module is used to admit more air. In order to avoid formation of thermal NO_X, the transition from rich to lean conditions must be rapid. It is also not desirable to allow products (enriched with oxygen) from the lean zone to enter the rich zone. It is for these reasons customary to incorporate a contraction in the design of the mixing module.

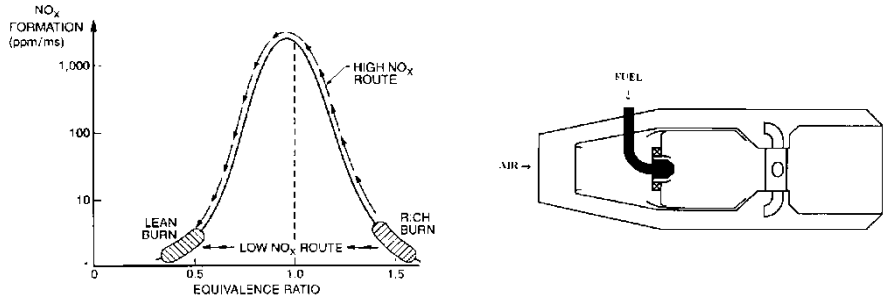

Figure 31: RQL operating regimes and concept design [26]

Primary zone cooling is difficult in RQL combustors. Invasive cooling will create local stoichiometric conditions near walls. This will be a source for NO_X production and lead to over-heated rather than cooled walls. There will also be large amounts of soot present in the primary zone. These will radiate heat to the walls and exacerbate the cooling problems.

4.13 Flameless combustion (Mild combustion, FLOX)

In 1989 J. A. and J. G. Wünning noticed that under conditions of strong exhaust gas recirculation, combustion was possible at very lean conditions. At furnace temperatures of 1000°C and about 650°C air preheat temperature, no flame could be seen and no UV-signal could be detected by flame detectors. Despite that, the fuel was completely burnt and the CO content in the exhaust was below 1 ppm. The NO_X emissions were in the single digits (ppm) and combustion was stable and smooth. J. A. and J. G. Wünning patented the concept and formed the company WS Wärmeprozesstechnik GmbH around the idea.

Contrary to a diffusion-type combustor that has high temperature regions close to the fuel injector, a FLOX burner will have a gradual temperature rise to final product temperatures. Hereby the high temperature

NO_X-producing regions are avoided. FLOX burners can operate as diffusion or premixed combustors. It is also possible to attain flameless combustion in a wide range of stoichiometric conditions ($\phi \approx 0.3–3$).

Figure 32 shows three distinct regimes of combustion. A is the conventional stable flame which works for any level of preheat. This mode is stable up to about 30 – 50% of exhaust gas recirculation depending on ambient temperatures. Region B is the unstable lifted flame region. The third region, C is the flameless oxidation mode characterized by high levels of exhaust gas recirculation and high ambient temperatures (>850°C).

Chemical reaction rates in FLOX combustors are low in comparison with the turbulent mixing rates taking place. A definite flame front therefore does not exist. Instead, conditions approach those of a PSR. Thermoacoustics, which rely on the interaction between a fluctuating pressure field and the displacement of a thin reaction zone, is therefore avoided. FLOX burners can thus, to a large extent, avoid combustion oscillations.

The FLOX combustor is commercially available and more than 1000 combustors are in service. The gas turbines market is being studied [58]. The technology offers significant economical advantages over SCR [59] (see Chapter 4.17).

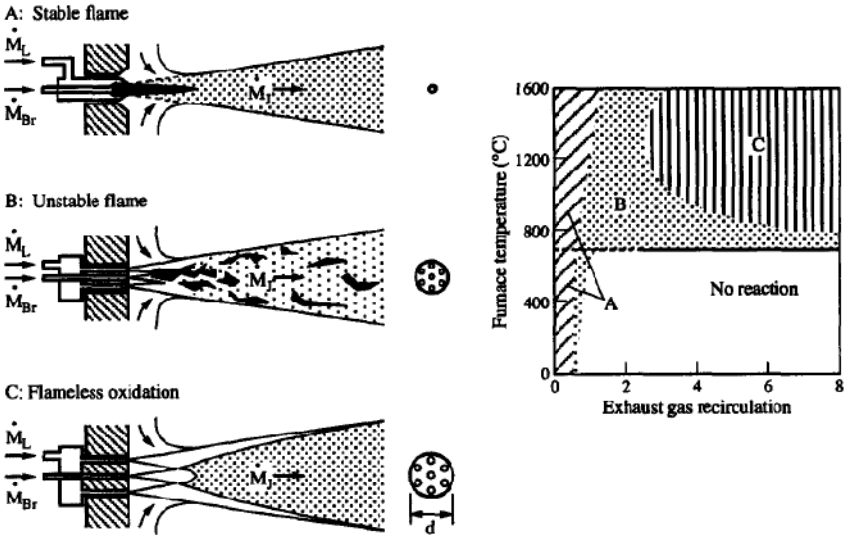

Figure 32: Flameless oxidation regime [60]

4.14 Staged air combustion (COSTAIR)

In the staged air combustor (Figure 33), combustion air is gradually introduced such that the flame starts out rich and cold. As more air is gradually introduced, combustion will take place at ever increasing levels of inert flue gases. This will reduce peak temperatures as the mixture of fuel, air and flue gases reach stoichiometric conditions. Hereby thermal NO_X is avoided to a large extent. Wang et al. concluded though, that COSTAIR is less efficient than FLOX in NO_X reduction. They also concluded that COSTAIR didn't incur quite the same cost as FLOX [59].

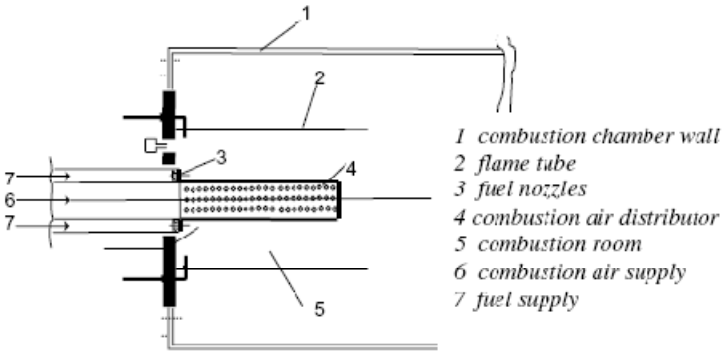

Figure 33: COSTAIR Combustor

Staging is also found in modern aero-engines as a means of extending the low emissions operating range. Here the combustor is divided into separate zones, each with its own injector. A different amount of zones are fuelled in order to change engine load. Each zone can therefore operate within a narrower AFR range. Three different variations within this concept are shown in Figure 34.

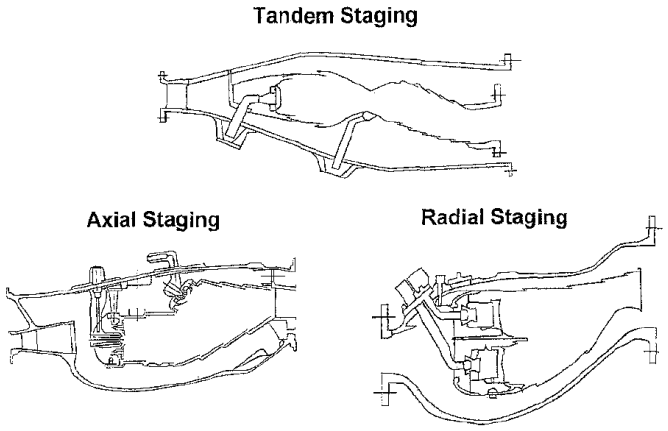

Figure 34: Staging concepts in aero-engines [61]

4.15 Catalytic combustion [26]

Catalytic combustors use a catalytic reactor usually followed by a thermal reaction zone to convert unburnt CO and UHC. The catalyst is typically made of some porous structure in order to provide large surface area. Often an expensive metal such as palladium, platinum or magnesium is applied to the internal surfaces of the matrix in order to support premixed oxidation at equivalence ratios that would be too lean or too rich for normal combustion. Catalysts will typically deteriorate at reaction temperatures above ~1270K. Fuel and/or air may therefore be added after the catalytic reactor in order to burn out CO and UHC and raise the temperature of the products to the appropriate TIT, which may be as high as 1570K.

The temperature of the inlet mixture must be high enough to reach light-off conditions. This temperature is in the range 617–1367K depending on the catalyst material. A pre-burner is therefore normally incorporated in order to raise the temperature of the inlet gases.

Several difficulties arise because of the catalyst's narrow operating temperature range. The temperature rise from inlet to exhaust must be within permissible limits as the catalytic combustion gradually raises the temperature. The temperatures developed within the catalyst are very dependent on inlet conditions. Inlet temperature, velocity and gas-air mixture strength and distribution must therefore be carefully controlled.

In [62], catalytic combustion under fuel-lean versus fuel-rich conditions was investigated. It was found that Pd, Pt and Rh catalysts were much more active under fuel-rich conditions. Gradual light-off occurred between 720 and 870 K. Products from fuel-rich operation are CO and H_2, so post combustion is required. Products from fuel lean combustion on the other hand are (the usual) CO_2 and H_2O.

Precision Combustion, Inc. has developed the Rich Catalytic/Lean burn (RCL) concept which has demonstrated low single digit NO_X in the 32–61% load range of the Solar Taurus engine. It has less than 10 ppm CO, full-load pressure drop at 5% and acoustics below 0.35 psi RMS (2.5 kPa) peak-to-peak [63], [64]. The design is capable of operation without a preburner after a light-off temperature swing. In Figure 35 a similar RCL combustor is shown for the Saturn engine.

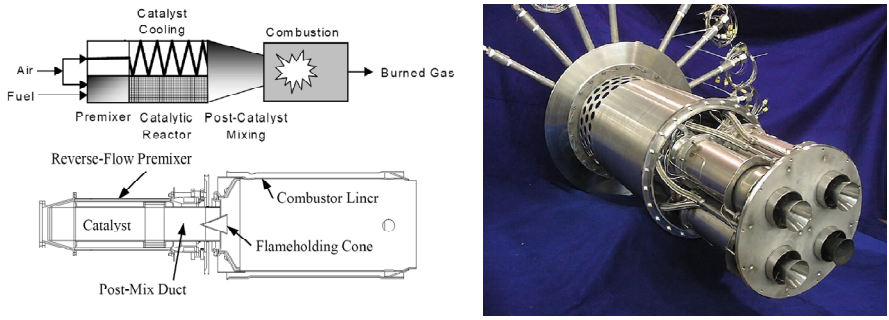

Figure 35: PCI Inc. RCL combustor. Catalytic combustor for the Solar Saturn [63]

4.16 Surface stabilized combustion (ALZETA)

The ALZETA premixed combustor from Alzeta Corp. features surface-stabilized combustion to minimize the formation of NO_X. The combustor can be seen in Figure 36.

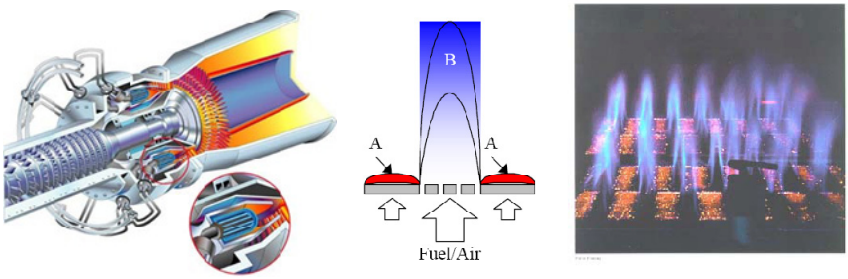

Figure 36: ALZETA NanoSTAR combustor for the Solar Titan, A is surface combustion, B is laminar flame combustion [65]

The laminar blue flame combustion zones (B) supported by the surface stabilized combustion (A) contribute to lower NO_X emissions in three ways. The primary benefit is from using fully lean premixed fuel and oxidizer. The second mechanism is the much lower residence time in the hot combustion zone, since the peak temperatures are realized in the combustion front formed by each laminar flamelet, which is very thin. The third mechanism is a more rapid post-flame cooling of each blue-flame zone via the gas phase radiation mechanism. By spreading the flame over a larger surface, the gas-layer thickness at any specific location on the injector is thin (relative to that of a conventional injector) and can more rapidly transfer heat as a result. The surface combustion (A) is reported to provide radicals that will support the laminar flames (B). The technology has demonstrated emissions of NO_X at less than 3 ppm with correspondingly emissions of CO in the 10 ppm region. The combustor is claimed to have very little combustion dynamics

or noise. Currently, the system is limited to operation on natural gas only. Combustor pressure drop is reported to be 4% [65].

Some potential drawbacks/problems with this design are:

- difficulty to operate on liquid fuels which must be completely and uniformly pre-vaporized and mixed before passing through the wall
- manufacturing problems and costs associated with large sintered structures
- fouling of pores
- thermal instability issues (bending, cracking)

4.17 SCR, SNCR

As an alternative to direct combustion emission abatement, flue gases may be treated a posteriori. In an SCR system (Selective Catalytic Reduction) flue gases first pass through an oxidation catalyst to remove CO and UHC. The gases are subsequently mixed with ammonia and passed through the SCR catalyst. Here the NO_X is converted to N_2 and water through the following reactions:

$$6NO + 4NH_3 \rightarrow 5N_2 + 6H_2O \quad (4.14a)$$

$$6NO_2 + 8NH_3 \rightarrow 7N_2 + 12H_2O \quad (4.14b)$$

The catalyst (usually vanadium pentoxide) works best with natural gas. It is sensitive to sulphur (SO_2 poisoning) and fluctuating inlet temperatures. Optimum flue gas temperature is 560–670K. The system is bulky and costly to install [26]. Typical temperatures for GT exhaust gases are 700–850K. This is too high for SCR. Recuperated GTs, on the other hand, may have temperatures as low as 650K and may therefore have an SCR added directly downstream. Un-recuperated GTs in combined cycles may have the SCR integrated within the HRSG in order to optimize the working temperature for the catalyst. NO_X reduction in the order of 90–95% is achievable. When pushing the technology, higher amounts of ammonia are released (slip).

Selective Non-Catalytic Reduction (SNCR) is used in boilers to abate NO_X. Ammonia (Thermal De-NO_X) or urea (NO_XOUT) may be injected into a furnace where the temperature is approximately 1250K [66]. The process requires an oxidizing environment, i.e. excess oxygen molecules must be present. If hydrogen or hydrogen peroxide is added, the process may be optimized for 1100K operation. This technology is obviously more robust, more compact and less expensive to install, but also less efficient in the use

of the reducing agent. It is tempting to try to integrate this technique within the turbine inlet duct (TID), the component connecting the combustor with the turbine, since the Turbine Inlet Temperature (TIT) for many gas turbines is suitable. A residence time in the order of 30 ms is, however, required [66]. This is most likely not achievable in many existing designs, so modifications would have to be done. The effect of pressure on the Thermal De-NO_X would also have to be considered. This was studied by Schmidt et al. in a flow reactor capable of operating at pressures up to 50 bar. Increasing pressure resulted in a modest decrease in the rate of NO removal [67]. The concept therefore seems possible in certain applications.

Instead of injecting ammonia or urea, cyanuric acid may be injected. This technique is called RAPRENOX. While showing much promise initially, it now seems to offer little advantages in that the thermal operating window is similar to SNCR and that NO is converted to N_2O.

4.18 Scrubbers

Scrubbers are used to remove particulate matter or gaseous pollutants. In the simplest case they bring water into contact with the flue to absorb the pollutants. The scrubber is designed to provide a large contact surface and a sufficient residence time for the contact between agent and subject gas. Scrubbers may also use reagents to chemically remove unwanted substances. Lime ($CaCO_2$) is added for desulphurization. Other agents may be added to enhance the solubility of NO_X in water. The working agent needs to be cleaned or regenerated. This may pose new problems. Scrubber materials, at the end of their useful lives, themselves may become highly toxic waste.

5 Fuels for gas turbine combustion

5.1 Natural Gas (NG)

Natural gas is a fossil gaseous fuel found in oil wells and pockets in the Earth's crust. It consists mainly of methane. The lower heating value of natural gas is approximately 40 MJ/Nm_3. Proven reserves have outpaced production by a wide margin since the 1970s and are now equal to about 66 years of production at current consumption rates [68].

5.2 Petroleum diesel

Petroleum diesel is refined from crude oil, which is a fossil fuel. The lower heating value of diesel is approximately 41 MJ/l. Remaining resources of oil are sufficient to meet the projected average annual production between now and 2030 [68]. Production is estimated to peak somewhere between 2008 and 2037 [69].

5.3 Coal

Coal is also a fossil fuel. It consists mainly of carbon, but H_2, N_2, H_2O, S, CH_4 and minerals may also be present in various quantities. For gas turbine combustion, the coal must be converted to a gaseous or liquid fuel. The first step will be gasification whereby syngas is produced. The gasification plant may be combined with a gas turbine and a bottoming cycle to form an IGCC or Integrated Gasification & Combined Cycle plant. The energy density of coal is roughly 24 MJ/kg.

FBN is a problem in coal combustion. Coal and coal-derived fuels will typically contain 0.5–2% nitrogen by weight [66]. The Earths coal resources are vast. They are projected to last for at least 300 years at the current consumption rate.

5.4 Biogas: sludge gas, swamp gas, landfill gas

Anaerobic digesters are used to convert sewage to biogas and fertilizer. Decomposition is caused by natural bacterial action in an oxygen-depleted environment. The digester is fed with pressed sludge cakes or liquid sludge. Reactions take place at low temperatures. In mesophile reactors the temperature is approximately 37°C. Fermentation will be slow and the reactor will be large. A more efficient and compact type of reactor is the thermophile reactor working at ~55°C. This type is more sensitive though. Most anaerobic digesters will produce a gas with ~50% methane, ~50% carbon dioxide and 0.3-2% H_2S, and significant amounts of mercaptans. If

the sludge gas is aimed for an NG network, all these compounds have to be eliminated at some stage. This is typically done in water or chemical absorbers or active carbon adsorbers. The lower heating value is approximately 23 MJ/Nm^3 [27]. Gases produced by biodigestation are thus Medium Calorific Value (MCV) gases.

Swamp gas comes from natural digestation of biological matter in wetlands. It usually contains no chlorinated hydrocarbons. It has a low C_2+ hydrocarbons content but may contain some H_2S.

Landfill gas may contain less sulphur if ferric oxide from rusting metal food cans is present. However, chloride production may be high in these localities leading to hydrochloric acid production on combustion. FBN in the gasification gas is typically very low (<0.1 ppm) [14]. The lower heating value is approximately 16 MJ/Nm^3 [27].

Other sources of biogas are municipal wastewater treatment plants, farms and food industry waste.

5.5 Biomass gasification gas and pyrolysis gas

Biomass gasification is a process where heat is added to solid biomass in an oxygen-depleted atmosphere. In pyrolysis gas all oxygen supply will be from the fuel itself. The pyrolysis products are mainly tar, carbonaceous charcoal and low molecular-weight gases such as CO, CO_2, H_2, CH_4 C_2-hydrocarbons, benzene and H_2O. If oxygen is used instead of air, the product will contain larger quantities of H_2, especially if water is added in the gasification process. A mixture, produced by gasification, largely containing hydrogen and carbon monoxide is popularly referred to as synthesis gas, or syngas for short. The syngas may be converted to liquid fuels by applying the Fischer-Tropsch process. Typical GCV is 4–7 MJ/Nm^3 for air gasification gas and 10–18 MJ/Nm^3 for oxygen gasification [28]. Examples of biomass gasification gases are the three first gases of Table 5 in Paper 1. Experience from the Värnamo facility shows that biomass gasification gas from wood has low sulphur content (50 ppm H_2S after gasification) [14]. It may however have large quantities of FBN (in the order of 0.25%).

The ARBRE facility, which is similar to the Värnamo plant, is shown in Figure 37. Here the biomass comes as wood chips for storage and drying. Flue gases are used to raise the temperature of the biomass and expel moisture. The wood chips are continuously fed from beneath into the air-blown gasifier, which contains a sand fluidized bed. Gas leaving the gasifier contains ash, wood, char and sand, which is separated out in cyclones and

returned to the bottom of the gasifier. Heavy hydrocarbons (tar) will then be broken down in the cracker. The cracker contains dolomite as a catalyst. Thereby this process can be made non-exothermic. The heating value of the fuel can therefore be maintained [70]. Tars will condensate at 200–500°C [70]. It is therefore important to remove or convert them before they lead to plugging or break-down of subsequent processes such as filters, heat exchangers or turbines. The gas will then be cooled and cleaned from dust particles before being fed into the scrubber; where ammonia, traces of alkali compounds and heavy hydrocarbons, which otherwise could condense out in the gas compressor are removed. From there on it is a regular combined cycle plant.

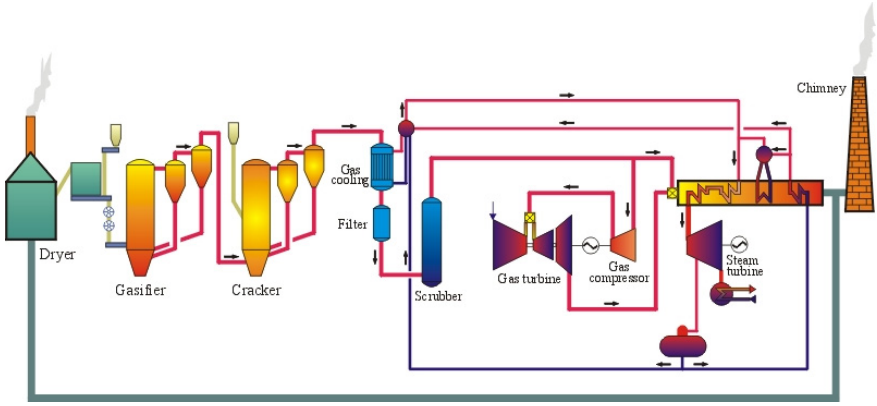

Figure 37: The ARBRE IGCC plant [ARBRE web]

In Figure 38 the option to produce hydrogen from the pyrolysis gas is shown. The process used here is called 'steam reforming'.

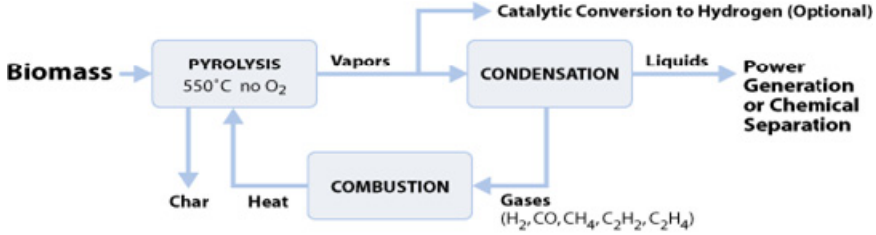

Figure 38: Pyrolysis of biomass with optional separation of hydrogen and liquids [U.S. DOE Web]

5.6 LCV combustion in gas turbines

The effects that anthropogenic combustion have on our environment were discussed in Chapter 2. It is clear that the most important contributor to global warming is CO_2 formed in fossil fuel combustion. If combustion is to

be as prolific as it is today, it has to be CO_2 neutral to a large extent. We therefore need to switch to renewable alternatives or employ some sort of CO_2 sequestration and storage scheme. Furthermore, fossil fuel resources aren't endless. Combustion of the non-fossil MCV and LCV fuels, as outlined above, will therefore become more important.

There are, however, many challenges with bio-fuel combustion. NO_X and SO_2 formation during combustion (which in the case of certain biofuels is exacerbated by large quantities of FBN, H_2S and mercaptans) is perhaps most notable. In addition, alkali compounds entering the fuel compressor, gas turbine, boiler and stack will cause deposits, erosion and corrosion problems.

LCV fuels will have a low stoichiometric flame temperature. They will therefore produce small quantities of thermal NO_X, which can easily be in the single-digit range, even for diffusion-type combustors. Many of the fuels tested in Paper 1 displayed this behavior. Based on the limited amount of mixtures tried there; LCV gases with LHV~5MJ/kg and T_{ad}~2100K will have single-digit non-FBN NO_X. The diffusion-type combustor is well-proven, simple, robust and very stable in terms of combustion oscillations and blow-out characteristics. In order to further reduce NO_X, other techniques may be used as well:

- cleaning or modification of fuel gases
- after -treatment of flue gases

At 600 ppm FBN, some 70% of it will be converted to NO_X. This equates to approximately 100 ppm NO_X in the exhausts (Paper 1, [71]). By today's standards that is not acceptable. Pre- or after-treatment are therefore necessary.

Cold-cleaning of the fuel may remove particulates, alkali metals and reduce ammonia concentrations to 600 ppm. The gas may then be desulfurized with a chemical or physical sorbent which may be regenerated. On the downside of this method there are heat losses, water saturation and the necessity for treating tarry gas washing residues [71].

Catalysts may be used to convert fuel-bound ammonia to hydrogen and nitrogen. Olofsson, for instance, tried a Ni-based catalyst which was able to remove 35–90% ammonia at 790–880°C [72].

The following after-treatment techniques may be used:

- cleaning of flue gases from NO_X with SCR in the exhaust of recuperated gas turbines
- cleaning of flue gases from NO with integrated HRSG/SCR in CC plants
- cleaning of combustor efflux from NO with SNCR where TIT is suitable
    - will require modifications to GT for ammonia/urea injection and sufficient residence time between combustor and turbine
- cleaning of flue gases from NO_X and SO_2 with scrubbers

Most of the combustors detailed in Chapter 4 are aimed at lowering the combustion temperature of HCV and MCV fuels and/or diluting the reactants in order to avoid thermal NO_X. These will not be good candidates for LCV combustion since these requirements are already fulfilled by the fuel itself. Furthermore, lean premixed concepts are not suitable to burn fuels with FBN. Instead, with a 'starved air' primary zone, more of the FBN is converted into molecular nitrogen, thereby lowering the formation of fuel NO_X.

Combustors based on 'initially rich' combustion concepts are:

- RQL (see Chapter 4.12)
- Staged air combustion (see Chapter 4.14)

In practical applications, these concepts still would yield too low gains as reported in Paper 1. They would therefore still need to be combined with pre- and/or post-treatment technologies.

FBN will only form in the presence of CH. CH_4 will therefore often be varied in experiments in order to change the HCN pool and illustrate this effect. Another approach would thus be to use fuels containing only one of the two species of CH, i.e. H_2 or CO, and design combustion concepts around this approach. The FBN will itself predominantly be converted to NH_3 when found as amines and as HCN, if aromatic rings were carrying the nitrogen. This would indicate that hydrogen fuels carrying more amines and less aromatics would have lower conversion ratios in a carbon depraved situation.

In summary it can be concluded that diffusion-type combustors will by themselves yield single digit NO_X for non-FBN fuels, whereas nitrogen laden fuels will incur extra cost in terms of pre and/or post treatment. More advanced combustor concepts, devised to reduce fuel NO_X are inadequate by

today's standards. Even without FBN, pre-treatment will still be required for fuels containing minerals, alkali and sulphur.

5.7 Blast furnace gas

Blast furnace gas is produced in metal reduction processes. As carbon is added to the metal ore, the metal will be reduced and in the process CO and CO_2 will be produced. The gas is also known as converter gas or LD gas. The gases BF1–BF3 in Table 5 of Paper 1 are examples of this kind of gas.

6 Sprays

Sprays are very important for many industrial applications. Whenever liquids are required to be vaporized quickly or dispersed over large areas, sprays will be useful. In the field of combustion, sprays play an important role whenever the fuel comes in the form of a liquid. This may be as petrol, diesel, jet fuel or ethanol, to name just a few. Whenever a liquid is to be used as a fuel in flame combustion, it must first be disintegrated in order to present a large contact area to the gas phase. Secondly, each droplet must be heated by the air and/or combustion products such that it will evaporate fast enough to provide sufficient amounts of fuel in the gas phase for the combustion to progress at the desired rate.

Over the years many forms of injectors have been designed to provide a spray with more or less the desired characteristics. Obtaining an optimum spray entails getting:

- the desired size distribution
- the desired spatial distribution

Often times this means having a mono-dispersed spray, which perfectly fills the entire cross section of a duct in a short distance, or an entire volume in a short amount of time. This should be accomplished without wetting any walls, something that is clearly impossible. Today's spray systems are in general very far from these ultimate goals.

In the case of filling a volume in a short amount of time, the process will be a one-time event or perhaps more often intermittent. The typical case would be the diesel engine. This case is, however, outside the scope of this discussion. Spray systems of gas turbine combustors and military afterburners are, in contrast, continuously providing a spray to suit their application.

Besides aiming towards "the perfect spray" there will inevitably be economical aspects that limit the complexity of the spray system. The art is therefore in finding a balance between a good spray and economics.

In gas turbine applications a constant supply of large quantities of hot gas is available. This may be compressor discharge air for a combustor, or flue gases for an afterburner. The simplest type of injector in this case is an open-ended hole which admits the liquid flow at right angles to the gas stream. This is the "Liquid Jet in Gas Cross-Flow" (LJIGCF) injector. It can be found in premix ducts of LPP combustors (Figure 13) and fuel bars in

afterburners (Figure 22). The spray it produces can be seen schematically in Figure 39.

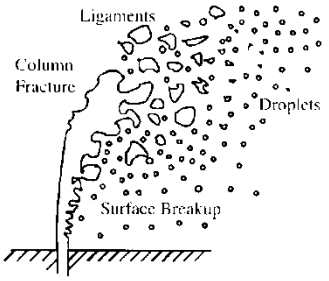

Figure 39: Liquid Jet In Gas Cross-Flow (LJIGCF) [73]

In order to understand the different breakup mechanisms in a LJIGCF, the different breakup regimes of a straight spray in quiescent gas will be touched on first. Then secondary breakup mechanisms will be reviewed.

6.1 Column breakup (liquid injected in quiescent gas)

There are four basic types of forces that will act on a spray. For some conditions some will dominate and some can be neglected. In other instances all will be active. The forces are [74]:

- Gravity force: $\rho L^3 g$
- Inertia force: $\rho L^2 V^2$
- Surface tension force: σL
- Viscous force: μLV

where L and V are the characteristic length and velocity, respectively, and g is the acceleration due to gravity. σ is the liquid surface tension and μ is the dynamic viscosity. The forces may apply both to the liquid or the gas phase, with the exception of the surface tension force. They may be internal or interfacial.

In the following discussion a plain round orifice injecting a liquid into a gas in the direction of the gravity pull is envisaged (e.g. a kitchen tap). A gradually increasing flow rate will be discussed according to Figure 40 (left).

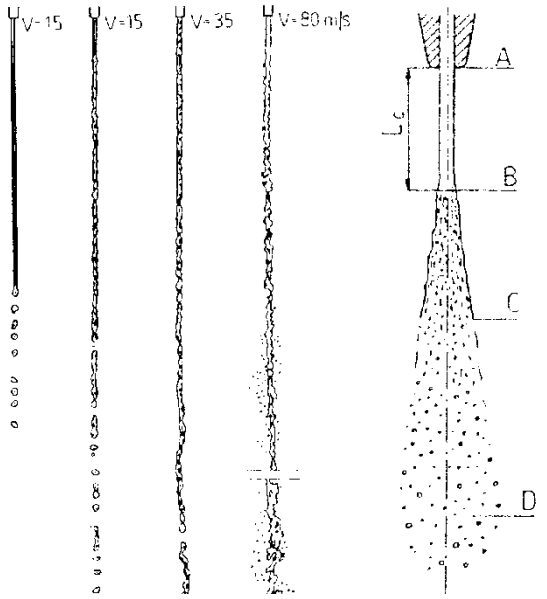

Figure 40: Four breakup regimes for water jet, orifice L/D=60 (left) and the three zones in the atomization regime (right) [75]

For low flow rates the jet will see very little aerodynamic forces due to the low relative velocity between the liquid and the gas. This regime (or mode) is called the Rayleigh or sometimes Plateau-Rayleigh breakup regime. The dominating force will be the surface tension, acting to change the cylindrical jet into spherical droplets.

As the liquid is injected, there will be small perturbations to the column diameter. These may stem from [76]:

- internal turbulence
- cavitation inside the hole
- a non-uniform exit velocity profile
- liquid supply pressure oscillations
- viscous boundary layer adjustment at exit of orifice

In addition it is suggested here that capillary forces at the edge of the hole may initiate disturbances.

As a result of these small early perturbations, pressure differences will emerge inside the column. This is because the surface tension force for a unit length of column will be 2σ and the balancing pressure force in the column will be $P \cdot d$. At two adjacent sections with different diameters, d_1 and

d_2 the corresponding pressures P_1 and P_2 therefore must relate to each other in the following manner [75]:

$$P_1 = \frac{d_2}{d_1} P_2 \tag{6.1}$$

This will lead to a higher pressure in the narrow section and a lower pressure in the wider section. As fluids will flow from high-pressure regions to low-pressure regions, the column will pinch off. Viscous forces in the column will dampen the perturbations and slow the pinching process. There will therefore be a reduced breakup rate and larger droplets for a more viscous liquid. Droplets will be larger than the nozzle size, regardless of the viscosity effect. Breakup will occur many diameters away from the nozzle (Figure 40, V=1.5 m/s).

Next, in the 1st wind-induced regime (V=15 m/s), aerodynamic forces will start to have effect as the relative velocity between the fluids is increased. The premise here is that the column already has some diameter variations. Where the column is thicker, the relative velocity will be larger due to continuity requirements in the gas phase (much like on the suction side of a wing). The pressure at these crests will therefore drop. At the same time, at the waists of the column the opposite will be true. The pressure distribution will thus reinforce the appearing distortions. In addition there will be axial shear forces at the liquid/air interface that will try to curl the interface. This phenomenon is the Kelvin-Helmholtz instability (see also Chapter 6.3 and Figure 57).

In the 2nd wind induced regime (V=35 m/s), non-axisymetric (sinuous) oscillations will form, resulting in droplets of size comparable to the column diameter [74]. These will come about in the same manner as in the 1st wind-induced regime. But now there will be enough aerodynamic forces to displace the centerline of the entire column. With lower pressures forming in the direction of an initial displacement of the centerline (again due to the interface surface curvature), the displacement will continue until gravity forces start to restore the column and eventually swing it over to the other side. The oscillations will grow until disintegration sets in.

When the flow rate is increased further (toward V=80 m/s), the aerodynamic forces will be able to break up the column closer and closer to the injection point. The flow will gradually transform into a spray. This is the atomization regime.

Malloggi et al. [77] suggested three distinct regions for this regime (see Figure 40 right):

- compact zone AB – where surface waves form and grow
- Disintegration zone BC – where the compact zone is transformed to droplets
- Drop zone CD – where the entire column has been broken up into individual droplets

As the flow rate increases, the compact zone and the disintegration zone will shorten, but never disappear entirely.

While some fundamental understanding has been possible to gain for the Plateau-Rayleigh, 1st and 2nd wind-induced modes, not in the least from stability analysis, much of the processes in the atomization mode are still poorly understood [74]. There has, for instance, been much debate about the inner structure of an atomizing jet in the vicinity of the nozzle. Recent studies at the Argonne laboratories concluded that the efflux at 5.5 nozzle diameters from the injection point of a diesel injector operating at 500 bar was not compact [78]. An example of their measurements can be seen in Figure 41.

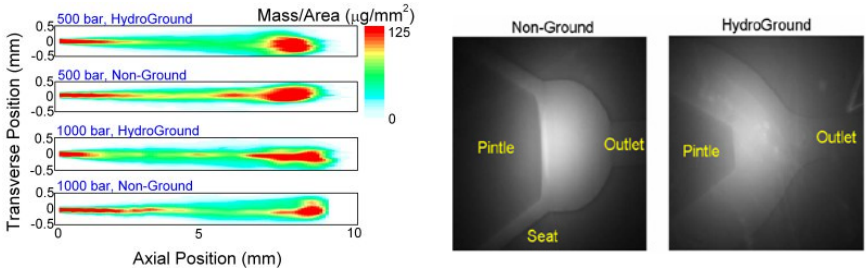

Figure 41: Mass distributions of sprays from two different common rail diesel injectors at different injection pressures and wear state [79]

It should also be noted that the definitions given here for the four breakup regimes are not very precise. Lin et al. [80] discusses the regimes in terms of the magnitude of the various forces at work. This certainly makes the delineations more distinct.

Using the Buckingham Π-theorem one can come up with dimensionless numbers that relate the governing forces to each other. The dimensionless numbers for the liquid flow are:

Reynolds number:

$$\mathrm{Re} = \frac{\rho_l L V_l}{\mu_l} \tag{6.2}$$

Weber number:

$$\mathrm{We} = \frac{\rho_l L V_l^2}{\sigma} \tag{6.3}$$

Froude number:

$$\mathrm{Fr} = \frac{V_l^2}{gL} \tag{6.4}$$

The Weber Number and Reynolds number may be combined to form the Ohnesorge number:

$$\mathrm{Oh} = \frac{\sqrt{\mathrm{We}}}{\mathrm{Re}} = \frac{\mu_l}{\sqrt{\rho_l L \sigma}} \tag{6.5}$$

The Ohnesorge number is useful in that it will be fixed for an experiment once the fluid properties and the geometry have been settled on. The Ohnesorge number is sometimes referred to as the viscosity number, Laplace number or Z number.

For a fixed Fr, We or Oh may be plotted against Re. The result with the different breakup regimes is plotted in Figure 42. These plots will, however, apply to the injection into a gas with a particular set of properties. For higher gas densities or viscosities, a particular set of Re–We or Re–Oh numbers will be shifted towards more atomization.

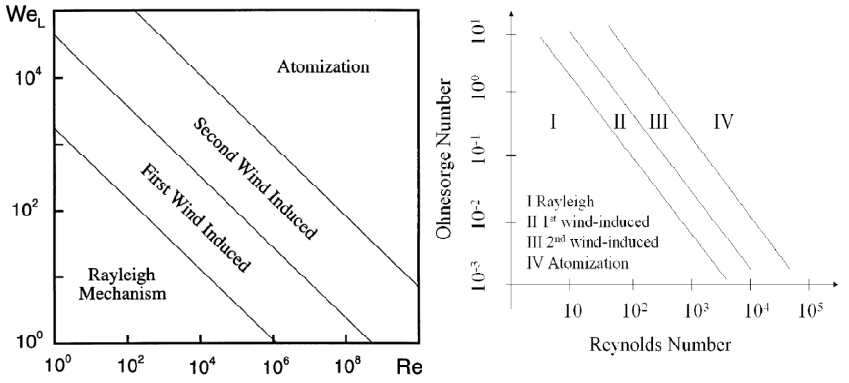

Figure 42: Classification of the modes of disintegration [74], [81]

Again it should be emphasized that different researchers will have different definitions of what constitutes the transition from one regime to the next. In addition, nozzle effects are ignored. The plots seen in Figure 42 are therefore quite sketchy [82].

6.2 Column turbulence

As indicated previously, turbulence generated inside the injector hole may affect the shape of the column as it exits the hole. Examples of turbulent columns can be seen in Figure 43 and Figure 44.

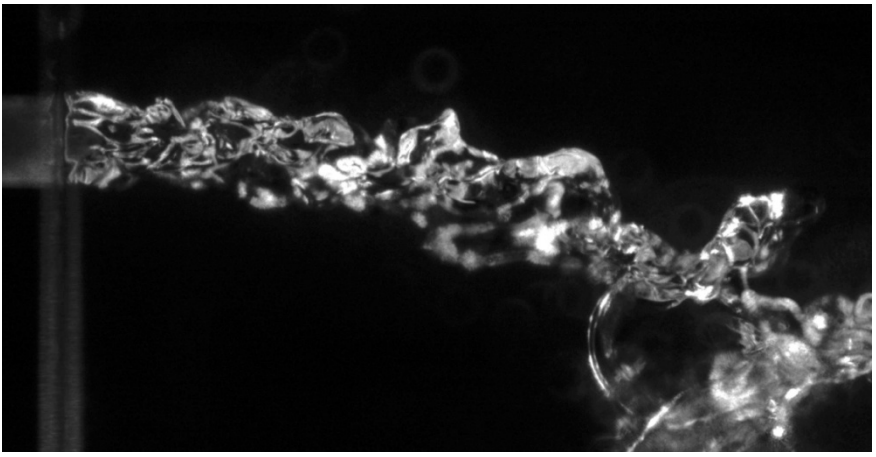

Figure 43: Column turbulence for injector from Paper 2, Re_l=3450, AMF=6.2 g/s

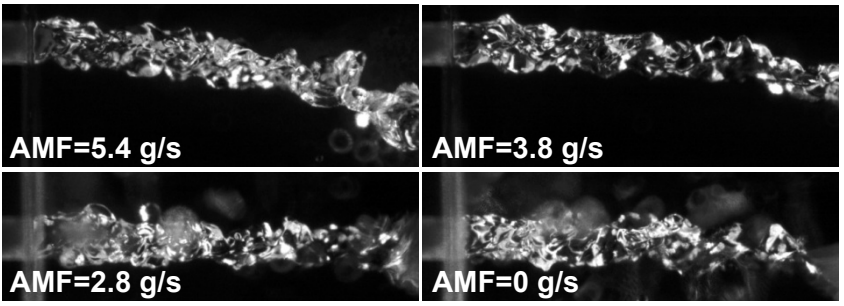

Figure 44: Column turbulence for injector from Paper 2 Re_l=3450, gradually reduced Air Mass Flow (AMF)

The air cross-flow entering from above in these images was here gradually reduced from 8 to 0 g/s at 200 kPa(a) pressure. The inertial forces from the air were thereby also gradually eliminated. We are left with only nozzle and gravity effects, the latter of which will bend the column slightly downwards. It is clear from these images that nozzle flow will have a

significant impact on the shape and size of the initial perturbations of the surface in this case. We can also see that the jet shows signs of becoming unstable at approximately AMF=5.4 g/s. This corresponds to We_g=6. Figure 45 shows a progression from Re_l= 3400 to 19000 for a nozzle with and without a turbulator insert. The effect of the turbulator is clearly seen. In comparison with the nozzle of Figure 43 and Figure 44, it is striking to see the range over which one configuration stays essentially laminar, in this case up until Re_l=19000, while for another configuration it will transition before Re_l=3450. The accelerated flow leaving the vertical nozzle in Figure 45 is here believed to laminarize the flow at higher Reynolds numbers [83]. Marmottant et al. [84] were making experiments on axisymetric liquid jet/air co-flow. For this situation and under those conditions, the turbulence made little difference. It is, however, reasonable to believe that in the cross-flow situation, the buckled surface will be conducive to aerodynamic breakup and aid capillary pinching.

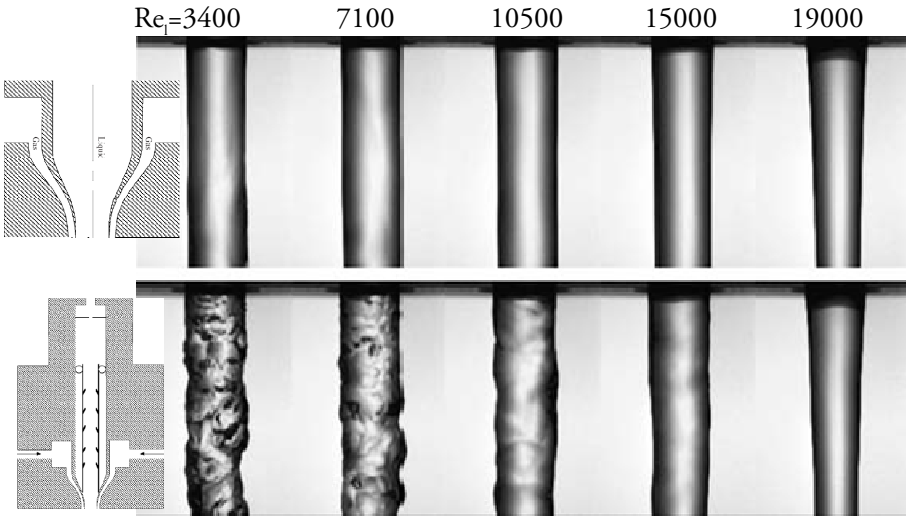

Figure 45: Influence of turbulence in nozzle. Top: laminar nozzle. Bottom; turbulent nozzle [84]

6.3 Instabilities relevant to spray formation

Kelvin-Helmholtz instabilities may form at the interface between two flows. It is shear forces at the interface between the flows that will try to deform the boundary such that it curls up on itself (see Figure 46).

Figure 46: KHI clouds and KHI in the atmosphere of Saturn

Rayleigh-Taylor instabilities may form whenever lighter matter is trying to displace heavier matter. This can be seen in many places in nature and elsewhere in the universe. Two examples are given in Figure 47. To the left cumulus clouds are shown. These are the cusps of plumes of lighter air that are formed when patches at ground level are heated unequally. The heated air will be of less density and therefore rise. In so doing, it will displace heavier air. To the right, the remnants of the supernovae in the Crab Nebula are pushing against the interstellar medium.

Rayleigh-Taylor instabilities will form where small undulations in the interface between light and heavy matter will favour a decrease of potential energy in a gravity or acceleration field. This will result in a redistribution of light matter away from, and heavy matter towards, the gravitational pull. In an accelerating field the light matter will tend in the direction of the acceleration and the heavy matter in the opposite direction. For sprays, the phenomenon can be seen wherever the gas phase accelerates the liquid phase. Small undulations will form on the windward side of liquid structures. These undulations will grow, become pockets and eventually tear the structure apart.

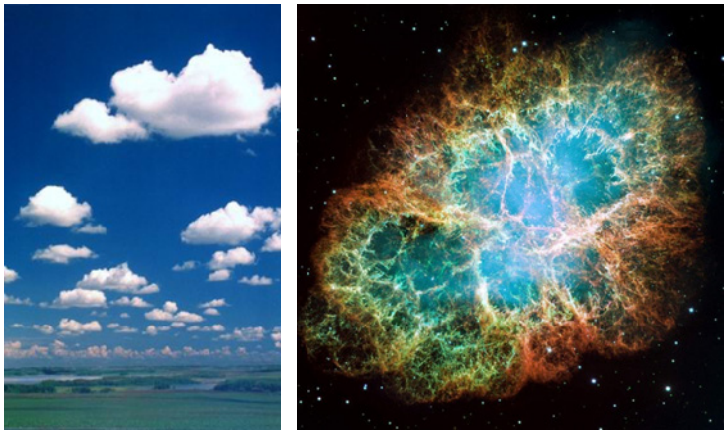

Figure 47: Cumulus humilis clouds and the Crab Nebula [Wiki]

Von Karman vortices may form over a wide range of Reynolds numbers. They can be seen in many places in nature. Two examples are given in Figure 48. The shedding will induce forces which can in some instances destroy the forming obstacle since there will be more form drag from a vortex shedding structure. In the case of a LJIGCF a von Karman vortex may induce lateral oscillations and more deflection of the jet.

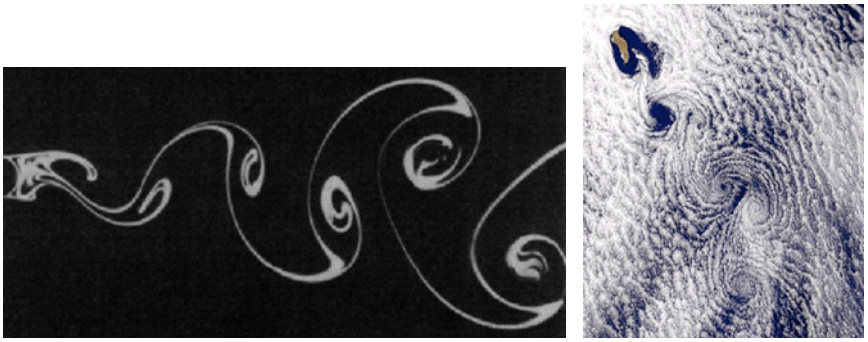

Figure 48: Computed von Karman vortex street (left) and the wake of an island made visual by clouds (right) [NASA]

6.4 Secondary breakup

After column breakup there will be individual lumps, or droplets of liquid, that are subjected to aerodynamic forces, gravitational pull and contact forces with other droplets or walls. In addition there will be surface tension forces trying to restore the droplet to a perfect sphere shape, and internal viscous forces that will resist rearrangement of molecules. At the interface, between the droplets and the gas, viscous forces both in the liquid and gas phases will set up boundary layer flows wherever there is a tangential relative velocity. These will be interdependent. At the interface instabilities may form that may break the droplet into separate smaller entities. At some point in the breakup process, surface tension forces will be dominant and the process will come to a halt.

In the year 1987, Pilch et al. [85] compiled available data on 'acceleration-induced breakup' of droplets that were suddenly subjected to a high-velocity flow field. They reported critical Weber numbers for acceleration-induced fragmentation, correlations for the velocity history of accelerated droplets and correlations for total breakup time. From this they could accurately predict the maximum size of stable fragments. During this work they identified different breakup regimes based on the critical Weber number We_c. They found that below $We \approx 12$, for $Oh < 0.1$ there will be no breakup. The droplet will simply oscillate at its natural frequency but stay

intact. For larger Oh, viscous effects will increase the structural integrity of the droplet. The droplet will thus be able to sustain more aerodynamic forces. This can be seen in the Broadkey correlation:

$$We_c = 12(1 + 1.077 \cdot Oh^{1.6}) \tag{6.6}$$

At about We=12 the droplet may interact with the gas phase in such a way that it breaks up into a few fragments. The breakup time will be long in comparison with the higher We_c droplets. This vibrational mechanism is shown in Figure 49.

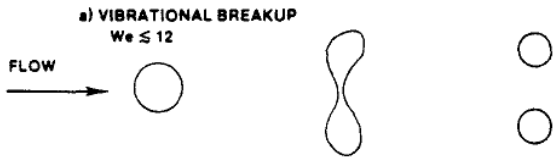

Figure 49: Vibrational Breakup, We≈12 [85]

In the bag breakup mode (Figure 50) there will be enough aerodynamic forces to stretch the droplet into an oblate shape through the combination of a high stagnation pressure on the windward side and a low pressure ring peaking somewhat upstream of the equatorial plane facing the flow (assuming a droplet resembling a perfect sphere). The stagnation pressure will next be able to invert the droplet and stretch the central portions into a thin membrane held together by surface tension. The membrane will burst and produce many small fragments. Later the more massive rim left behind will disintegrate into fewer and larger fragments.

This situation is also conducive to a Rayleigh-Taylor instability forming on the windward side, since light gas is trying to accelerate heavy liquid. In fact, all subsequent modes will have to be considered in the light of this phenomenon. According to Theofanous et al., Rayleigh-Taylor instability alone is the active mechanism for free-stream Weber numbers as low as 28 for low viscosity liquids [86].

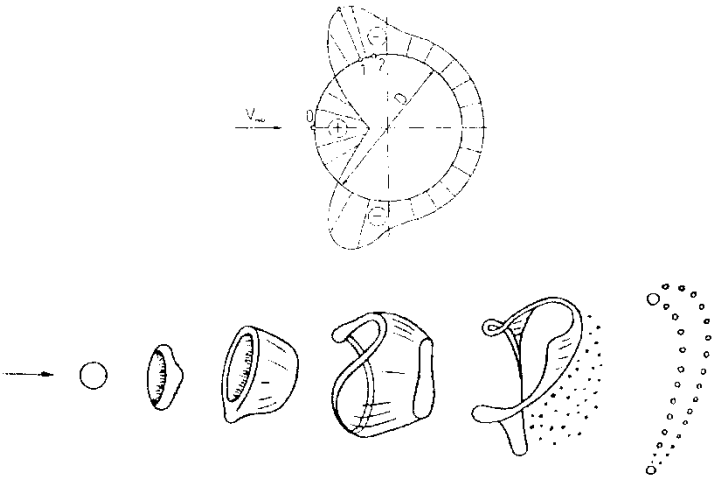

Figure 50: Pressure distribution leading to bag breakup, 12≤ We ≤50 [75]

For the following modes, the descriptions are taken from Pilch et al [85].

Bag-and-stamen breakup (Figure 51) is a transition mechanism that has several features in common with bag breakup. As in bag breakup, a thin bag is blown downstream while being anchored to a massive toroidal rim. In this case, however, a column of liquid (stamen) is formed along the drop axis parallel to the approaching flow. The bag bursts first. Rim and stamen disintegration follows. Bag-and-stamen breakup is sometimes referred to as "'club breakup", "umbrella breakup" or "'claviform breakup".

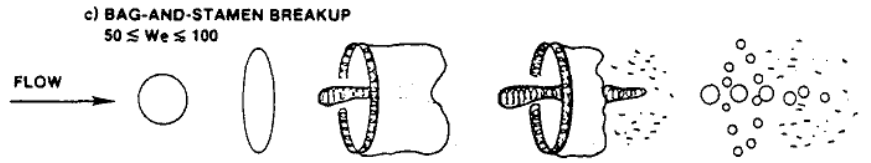

Figure 51: Bag and stamen breakup, 50≤ We ≤100 [85]

Sheet stripping (Figure 52) is distinctly different from the two breakup mechanisms just discussed. No bags are formed. Instead, a thin sheet is continuously drawn from the periphery of the deforming drop. The sheet disintegrates a short distance downstream from the drop. A coherent residual drop exists during the entire breakup process.

Figure 52: Sheet stripping, 100≤ We ≤350 [85]

At still higher Weber numbers, large-amplitude, small-wavelength Rayleigh-Taylor waves are formed on the windward surface of the drop (Figure 53). The wave crests are continuously eroded by the action of the flow field over the surface of the drop. This process is referred to as "wave crest stripping".

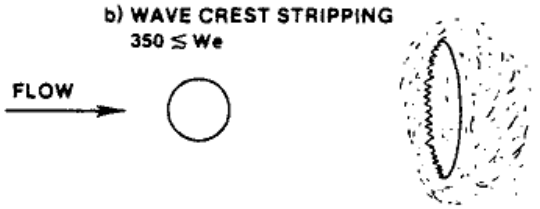

Figure 53: Wave crest stripping, 350≤We [85]

Large-amplitude, long-wavelength Rayleigh-Taylor waves ultimately penetrate the drop creating several large fragments before wave-crest stripping can significantly reduce the drop mass. Drop penetration by large-amplitude surface waves is referred to as "catastrophic breakup" (Figure 54). Catastrophic breakup leads to a multistage process in which fragments, and fragments of fragments, are subject to further breakup. This cascading process continues until all the fragments have Weber numbers below the lowest critical value.

Figure 54: Catastrophic breakup, 350≤We [85]

The different regimes can be collected in a We-Oh diagram as can be seen in Figure 55. Given a droplet and a flow condition, one can thus predict how it is going to break up. The nomenclature varies between sources however. Here instead of the 'Bag and Stamen' regime the authors refer to 'Multimode' breakup [87]. It has also been shown that under

rarefied conditions, modes may form that cannot be sorted into the above categories [86].

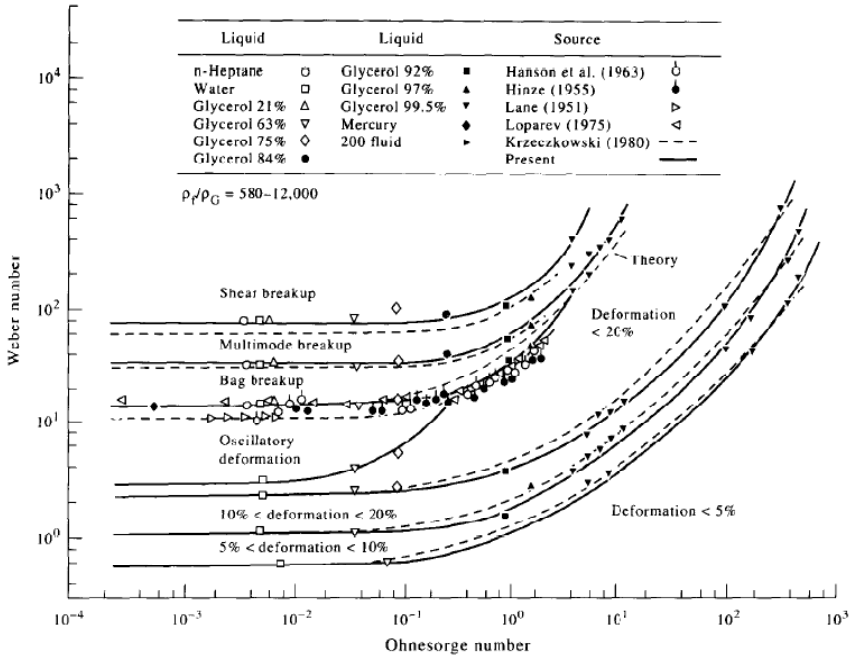

Figure 55: Secondary breakup regimes [87]

6.5 Some examples of breakup

A brief pictorial overview of different breakup situations is given for reference.

The breakups shown in Figure 56 and Figure 57 are the result of an acceleration of a slow dense liquid jet by a low-density light coaxial stream. The nozzle shown in Figure 45 (top) with a diameter of 7.8 mm was used. Only the general trends are given here. Numbers are indicative. For details see [84]. Beginning with no air co-flow, the column will exhibit capillary Plateau-Rayleigh instabilities for a water velocity of about 0.5 m/s. There will be crests with an initial spacing of 4.5 hole diameters. With low air velocities the column may start to meander and bags may form (Figure 56). This would correspond to the 2nd wind induced regime in the quiescent gas case. The difference, however, lays in the direction of the applied aerodynamic forces. At higher gas velocities (15 m/s), the undulations will be governed by the aerodynamic forces. The distance between successive crests will, close to the nozzle be in the order of the hole diameter. The crests are accelerated however, both by gravity and the air-flow, and will

therefore be gradually more separated. At an air velocity of about 20 m/s, digitations will start showing up. These are transverse, or azimuthal undulations due to Rayleigh-Taylor instabilities forming as the interface starts to dilate. These will grow in amplitude and eventually degenerate into ligaments. Figure 57 shows this progression from 15 – 32 m/s. As the air velocity increases, more transverse undulations will emerge and more and finer ligaments will form.

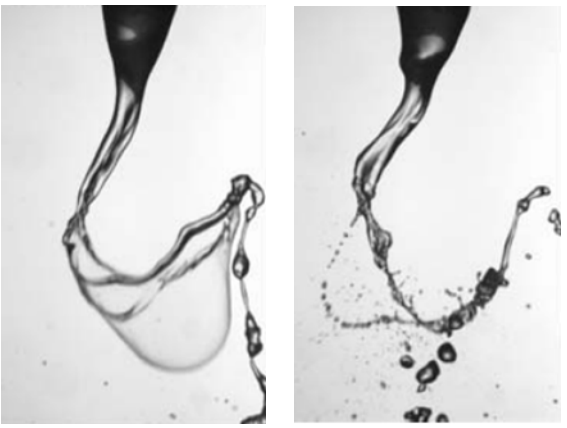

Figure 56: Bag breakup of column in co-flow at low relative velocities [84]

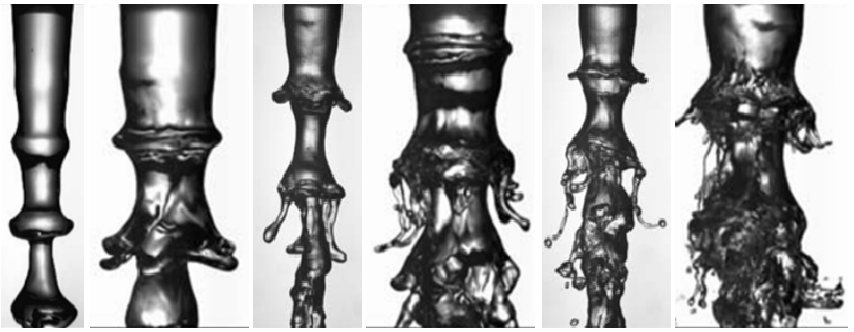

Figure 57: Peeling and ligament formation of column in co-flow at successively higher relative velocity between phases [84]

The spray in Paper 2 has We_g=14 and Oh=0.0049. These numbers compare well with the situation for the bag breakup shown Figure 58. The bubbles seen in Figure 66 and Figure 67 (and possibly Figure 43) are more spherical, whereas the bubbles in Figure 68 and Figure 70 are irregularly shaped. The trend is that smaller bubbles will have more surface tension forces. Thinner walls will have less inertia and therefore respond quicker to the surface tension forces. These types of bubbles will therefore exhibit more sphericity in general.

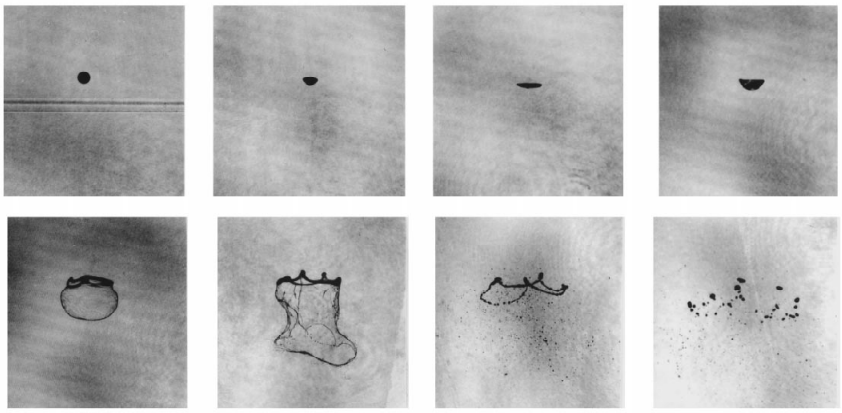

Figure 58: Time lapse sequence of bag breakup, water, We=15, Oh=0.0045 [88]

In Figure 59 the progression from bag via stripping to catastrophic breakup is shown. Rayleigh-Taylor waves are clearly visible in the right picture.

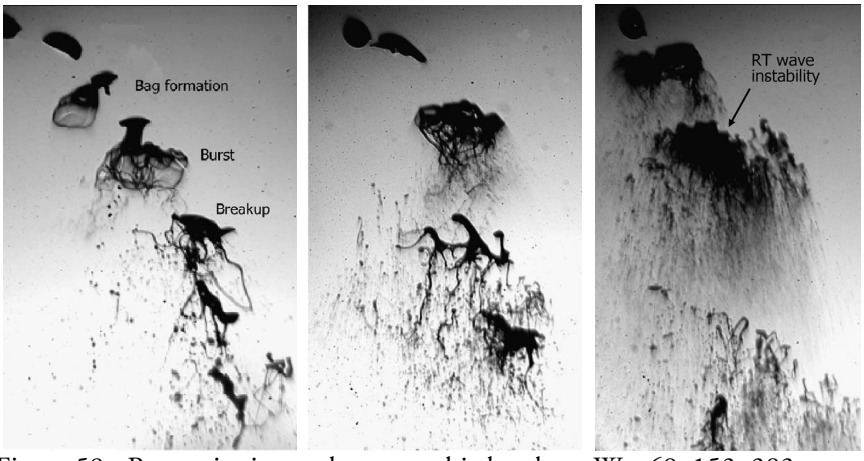

Figure 59: Bag, stripping and catastrophic breakup, We=68, 153, 383, Oh=$3.5 \cdot 10^{-2}$ [89]

The sequences in Figure 60 and Figure 61 show the effect of varying viscosity in that, as viscosity increases, the breakup will progressively be more ligament-like.

Many more high-speed video sequences for the intervals 9600<We<129000 and 0.002<Oh<82.3 are shown at the University of Minnesota website [90].

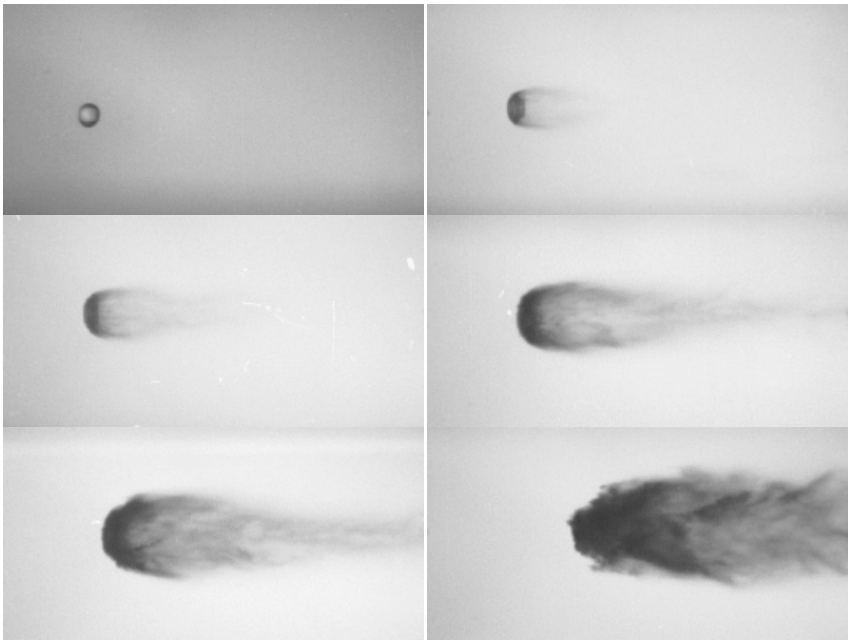

Figure 60: Stages in the breakup of a 2.6 mm water droplet behind a Ma=2 wave. We=11700, Oh=0.002 [91]

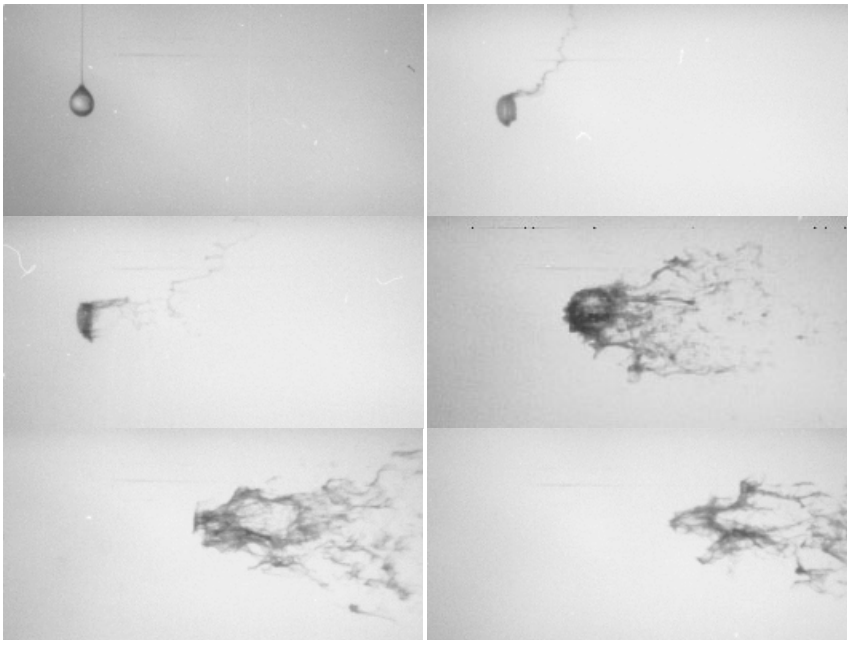

Figure 61: Stages in the breakup of a 2.9 mm water droplet with 2% polyox behind a Ma=2 wave. We=15200, Oh=82.3 [91]

6.6 Liquid Jet In Gas Cross-Flow (LJIGCF)

The breakup of a LJIGCF and subsequent secondary atomization will display phenomena that are combinations of everything mentioned so far in this chapter. In addition there will be aerodynamic forces acting at right angle to the liquid injection direction. The column breakup will be affected by the conditions inside the nozzle, such as velocity profile, turbulence, cavitation, and supply pressure oscillations. As the jet leaves the nozzle, capillary forces will try to expand the column if the molecules of the nozzle walls have higher attractive forces than the neighboring liquid molecules. This is of course dependent on the combination of fluid and wall material and can probably be neglected for the most part. When leaving the nozzle, the boundary layer in the column will have to readjust such that the velocities of the two phases match at the interface. Since the gas flow is essentially coming perpendicularly to the jet, this will set up two counter-recirculating vortices within the column. The internal turbulence will buckle the column surface. The approaching air will interact with the column. A pressure field similar to what is seen in Figure 50 will, combined with local stagnation pressure peaks in the buckled surface, deform the cross-sectional shape and interact with Rayleigh-Taylor instabilities wherever the interface is accelerated by the lighter fluid. If conditions are right, bubbles akin to 'bag breakup' may form inside the column and be blown out on the leeward side (Figure 43, Figure 66, Figure 67, Figure 68, Figure 70 and Paper 2). Shear forces on the sides of the column will try to curl up the interface. This is the Kelvin-Helmholtz instability. Sometimes von Karman vortices may form around the column. The pressure field around the column will then start to oscillate azimuthally. This will translate into lateral column oscillations. At higher gas velocities, side stripping will be seen whereby small droplets are sheared off the column. At even higher air velocities, catastrophic breakup of the column will be seen some distance away from the injection point. This is the situation for the We=568 spray in papers 8 and 9.

The column will bend in the airstream direction. Elements of the co-flow situation may emerge. Ligaments will be drawn out from the disintegrating column. Plateau-Rayleigh instabilities will form. Parts of the column and ligaments will therefore pinch off, forming large droplets subject to secondary breakup (Figure 63 and Figure 64). Droplets may collide and bounce off or merge downstream. The spray cloud will block and entrain gas. This will modify the gas phase velocity distribution and turbulence. The spray will be decelerated in the injection direction by the continuous phase, and in doing so momentum will be transferred to the

continuous phase. A vortex pair will form in the continuous phase as a result. Droplets further downstream will in turn respond differently to this modified gas flow. Smaller droplets will follow the modified flow field more closely (see Papers 8 and 9).

The trajectory of the spray will primarily be affected by the liquid to gas momentum ratio:

$$q = \frac{\rho_l \cdot V_l^2}{\rho_g \cdot V_g^2} \tag{6.7}$$

This is therefore often used together with the gas or liquid Weber number to classify the flow.

Many reports and papers have been written on certain characteristics and aspects of LJCIFs such as expected trajectory, dispersion of the spray, expected drop distributions, effects of viscosity on breakup length, etc. [92], [93], [94], [95], [96], [97], [98], [99]. Attempts have been made to model the compact zone breakup process with CFD techniques. It is, however, a difficult case to model from the beginning to the end because it essentially requires coupled two-phase Navier-Stokes computations (or at least LES with a very fine grid), with sophisticated treatment of the ever-changing topology as column, ligaments and droplets form voids, split up and combine. A combination of DNS/VOF and the 'Level Set' method seems promising [100].

The 'Level Set' approach is somewhat similar to what Nilsson [32] and Engdar [33] used to track the interface between burnt and unburnt species in combustion. A sample of what can be done is shown in Figure 62.

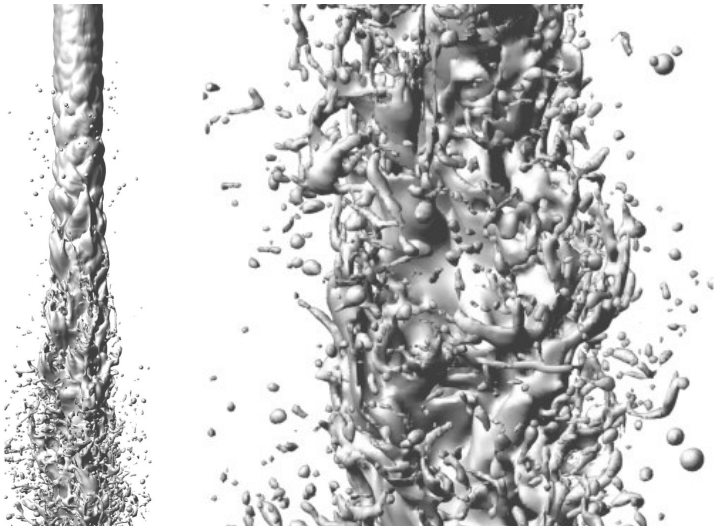

Figure 62: CFD computation of core breakup [100]

At higher liquid flow rates, where the column is broken up very close to the injection point, stochastic methods may be useful tools. These methods are common in commercial CFD codes. Here the primary breakup is assumed complete a priori. Additional knowledge is therefore required. This must come from experiments, correlations or more fundamental CFD work. Papers 8 and 9 exploit PDA measurements and a solver for the Basset-Boussinesq-Oseen equation (BBO) to recreate injection conditions for a LJIGCF.

Below are a few samples from a LJIGCF where many of the topics touched on in this chapter can be seen. While there are some common features between the figures, it is perhaps more striking to see how different they each look despite similar operating conditions. Even being able to compute one instance of this LJIGCF would still say very little about average downstream spray properties. It should be noted, though, that these sprays are not typical of the kinds used for technical purposes. Being poorly atomized by the nozzle and air; the resulting droplets will be too large to suit a gas turbine combustor or a diesel engine. They may however serve well to illustrate some of the effects that may contribute to atomization.

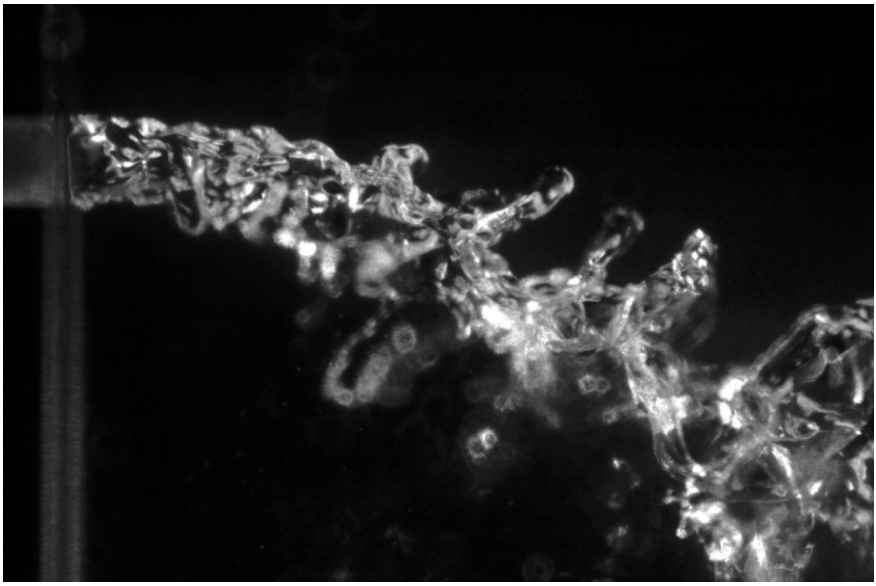

Figure 63: LJIGCF from Paper 2, We_g=14, 1.1 g/s water flow

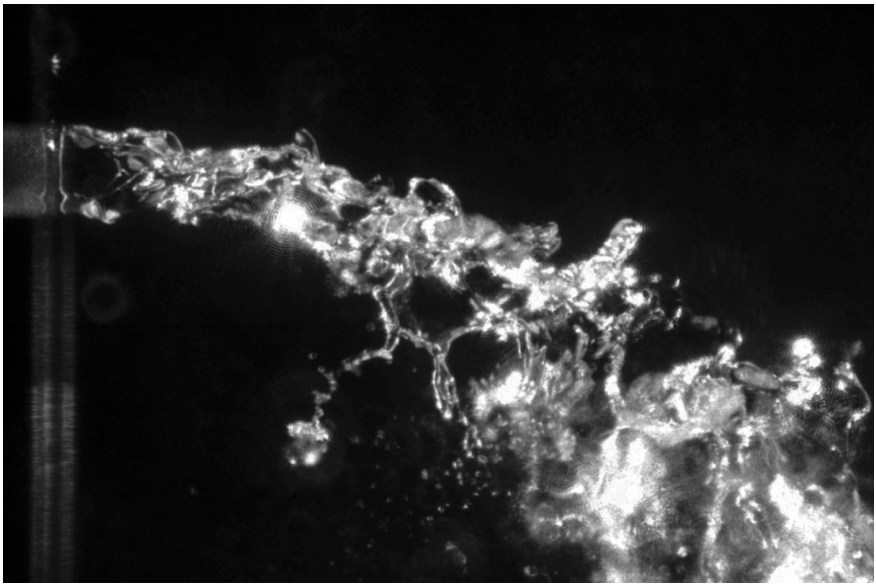

Figure 64: LJIGCF from Paper 2, We_g=14, 1.1 g/s water flow

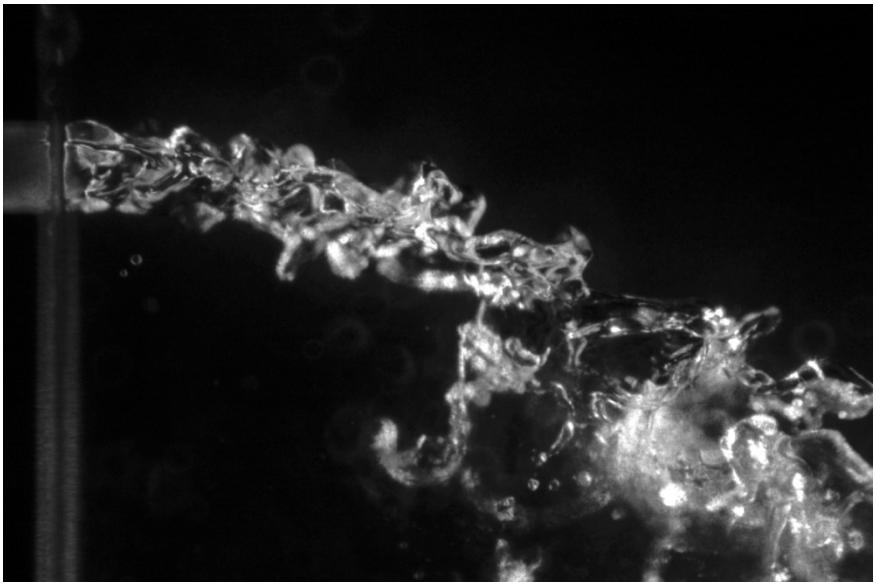

Figure 65: LJIGCF from Paper 2, We_g=14, 1.1 g/s water flow

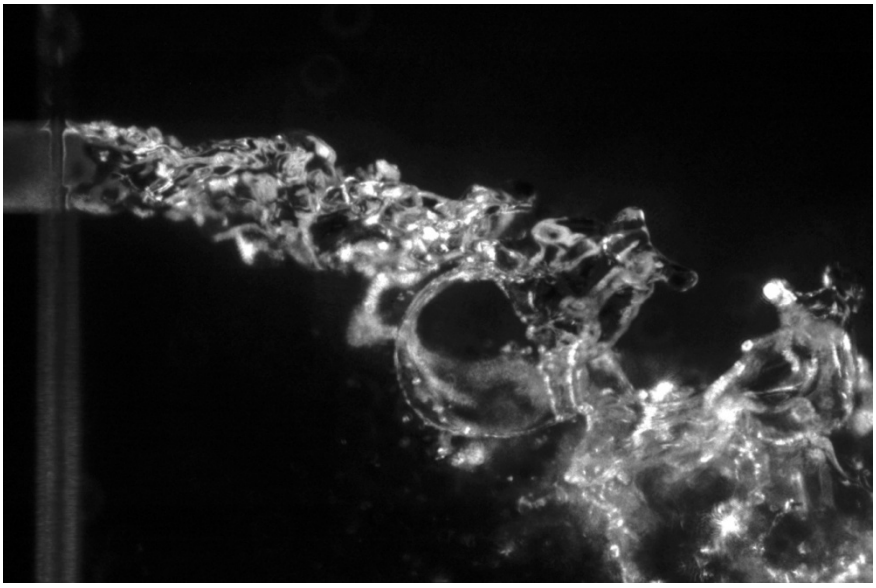

Figure 66: LJIGCF from Paper 2, We_g=14, 1.2 g/s water flow

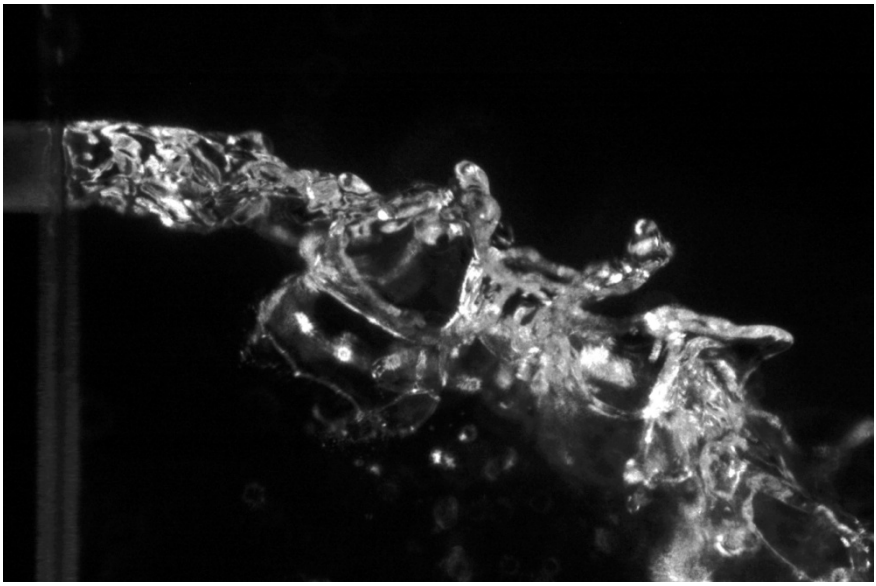

Figure 67: LJIGCF from Paper 2, We_g=14, 1.1 g/s water flow

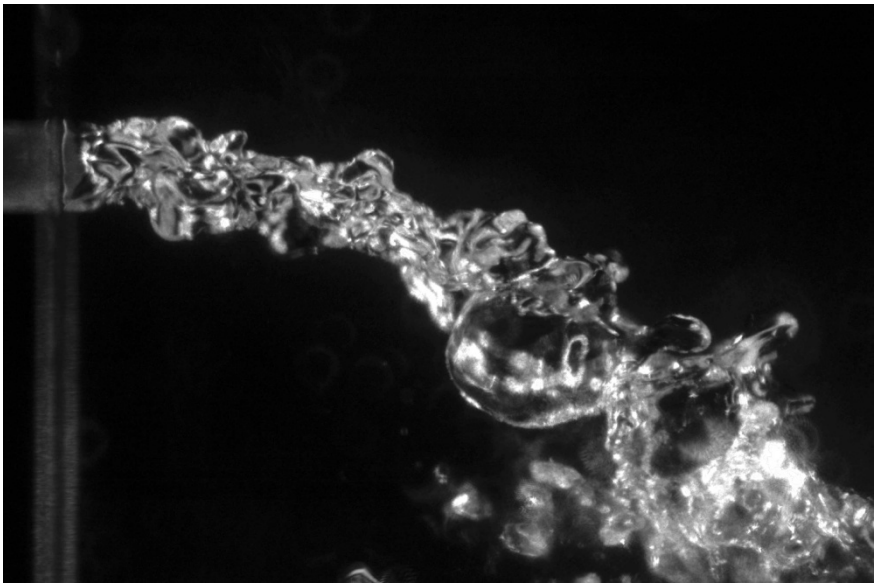

Figure 68: LJIGCF from Paper 2, We_g=14, 1.1 g/s water flow

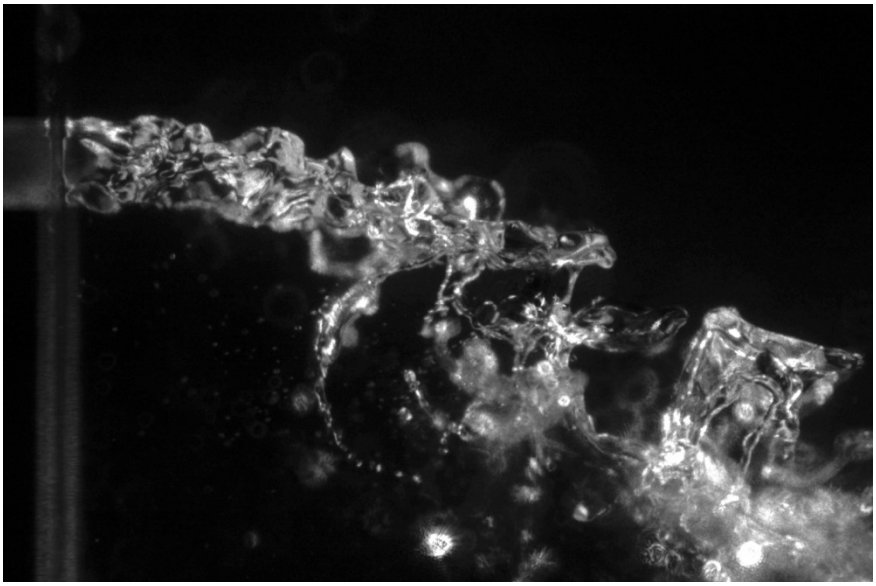

Figure 69: LJIGCF from Paper 2, We_g=14, 1.1 g/s water flow

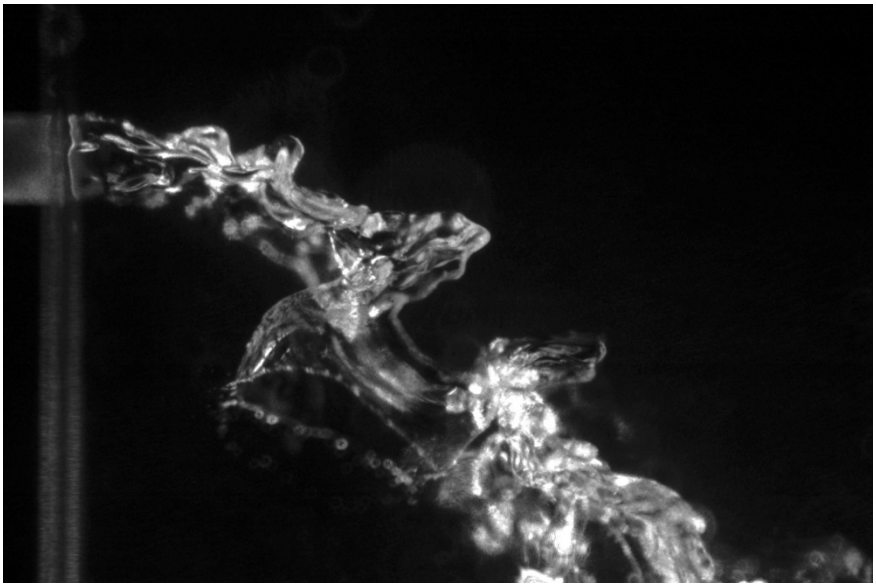

Figure 70: LJIGCF from Paper 2, We_g=14, 0.8 g/s water flow

7 Spray rigs

7.1 Small spray rig

For the purpose of studying sprays in cross flow under varying conditions, a rig was designed and built according to Figure 71. The rig is designed to flow 40 g/s of air heated up to 420°C with a pressure in the range 1-12.3 bar(a). Water flow up to 15 g/s and 200°C at 80 bar(a) may be admitted.

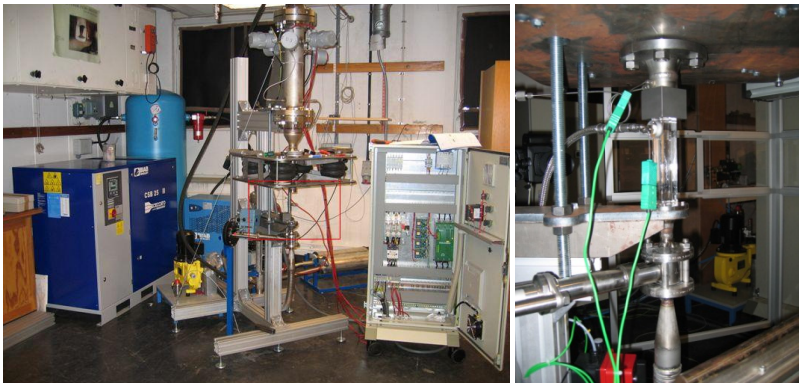

Figure 71: Small spray rig. Close-up of test section to the right.

The air path main components are:

- BIAB CSB 25-13 air compressor
- BIAB DE025 air cooler/dryer
- Gävle Galvan TK GGL-500 air reservoir
- Shubert & Salzer 8020/015VP0013M----C-Z3 air overboard bleed valve
- Micromotion CMF050M320NQFZWZZZ coriolis air massflow meter
- 36 kW Sylvania air heater
- Hellma test section
- Shubert & Salzer 8023/015VQ0113M--91B-Z3 air pressure control valve

The water path contains:

- Sartorius mass flow metering scale
- Dosapro Milton Roy XB140S(J)4H80 water pump
- Swagelok SS-4R3A5 pressure relief valve
- Backer/Knisslinge Mekaniska 6285-0640, 10 kW water heater

The test section, seen in Figure 71 (right) and Figure 72, was manufactured in Spectrosil 2000. Dimensions are shown in Figure 72 (right). As can be seen the section is monolithic, i.e. it is constructed of four rectangular slabs that are fused together. The advantage of this design is that there are no obstructions at the corners from a frame, holding separate windows. The test section was however found to fail at pressures above 9 bar(a). The reason for this is that the air pressure will produce large corner stresses.

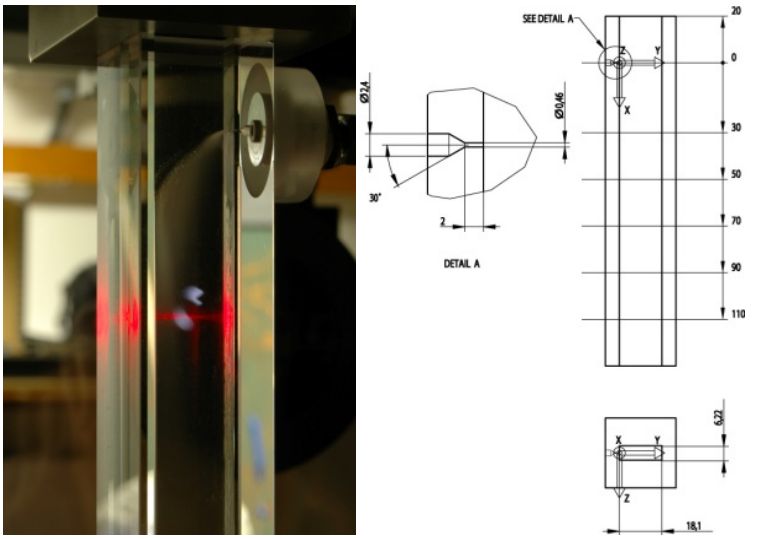

Figure 72: Small spray rig test section (dimensions in mm)

A measurement and control system was implemented in National Instruments LabView using FieldPoint I/O modules. Air mass flow, pressure and temperatures are controlled with PID algorithms. PID control of water temperature was also implemented but it proved to change too slowly to be practical to govern automatically. The user interface is shown in Figure 73 and the control loops are shown in Figure 74 and Figure 75.

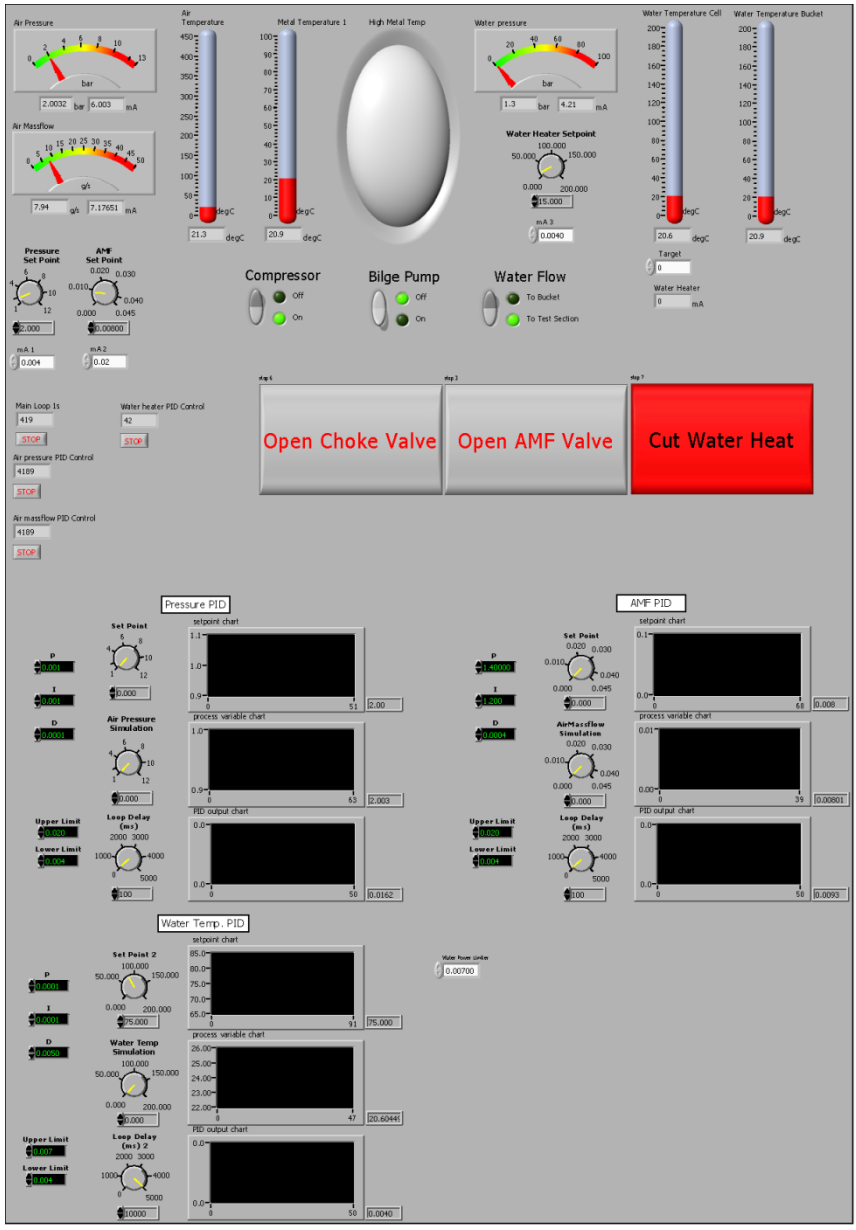

Figure 73: Small rig user interface

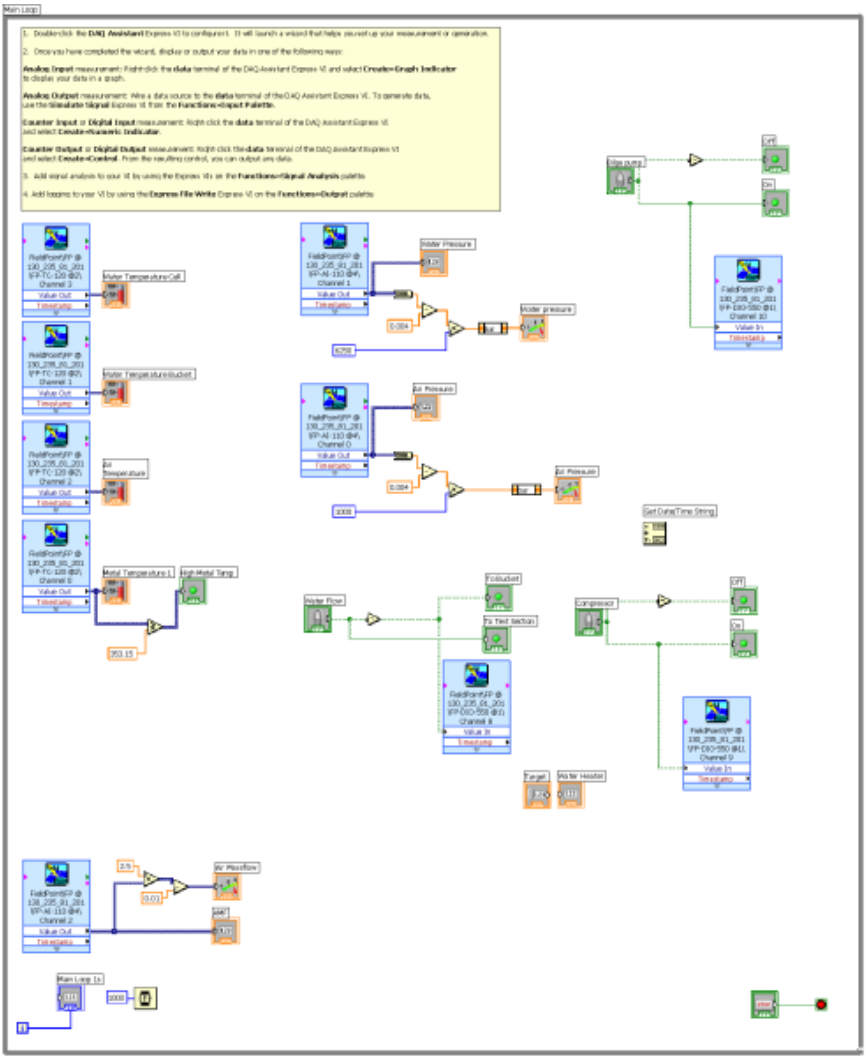

Figure 74: Small spray rig main control loop

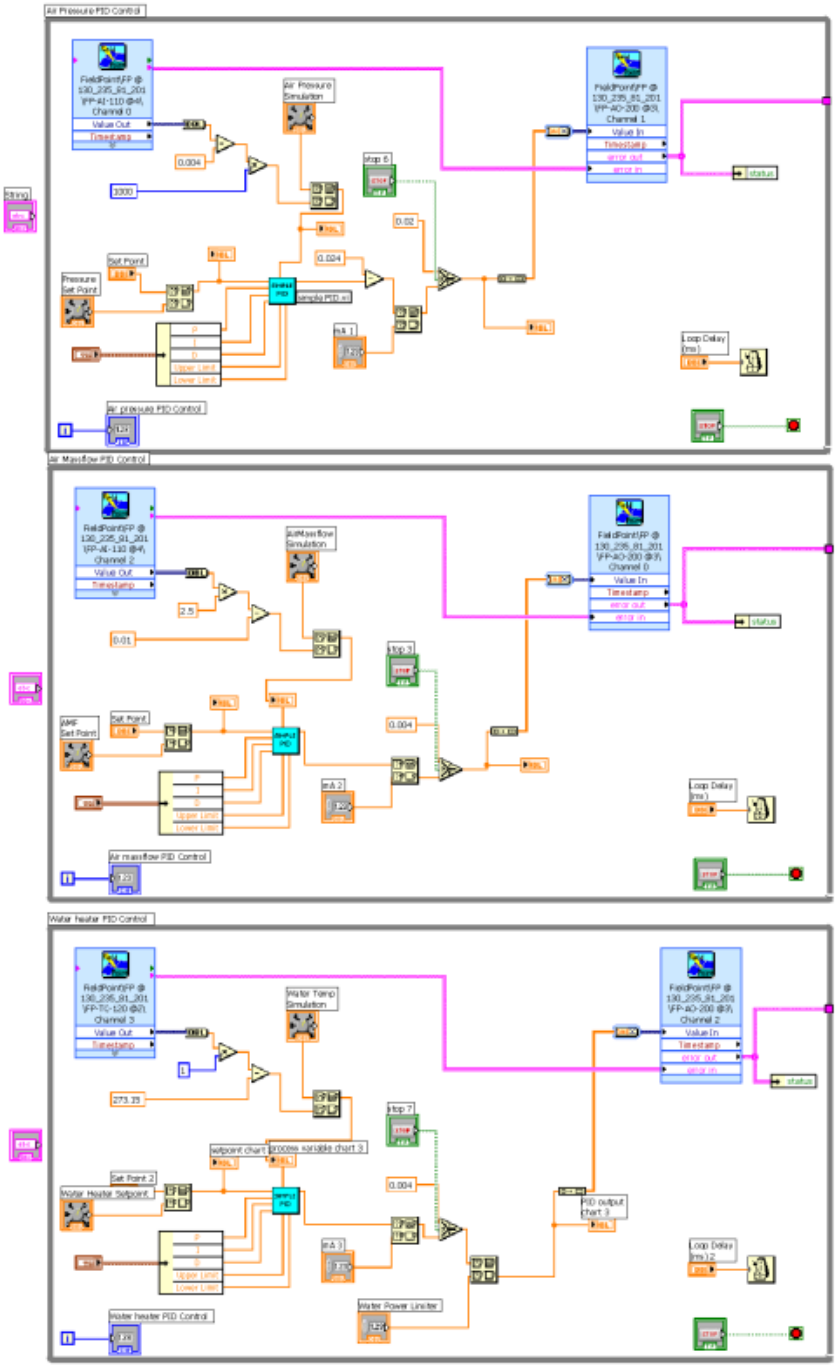

Figure 75: Small spray rig air pressure, air mass flow and water temperature control loops

Air temperature was measured at the inlet to the test section with a Pentronic 20-22150100 type K thermocouple. Inlet pressure was measured with a TECSIS E113 pressure transducer. Water pressure was measure at the pump with a TECSIS E111 pressure transducer. Water temperature was measure at the inlet to the test section with a Pentronic 20-22150100 type K thermocouple. The small spray rig was used in Paper 2.

7.2 DESS rig

The DESS rig is an existing rig located at the Combustion Physics Department of Lund University. The rig is shown in Figure 76. It was used to create the spray investigated in Papers 8 and 9. The rig is currently capable of blowing 1.1 kg/s of air up to 9 bar(a). It can operate with air pre-heat up to 100°C for extended periods.

A test section was designed to fit in the DESS test chamber. It is shown in Figure 77. Figure 78 shows the test section in situ. Also shown are the set of liquid orifices manufactured to fit. Only the ∅0.6·L=0.38 mm hole was used. The cross section of the test section is 40·30 mm. It is approximately 100 mm long. The test section frame was manufactured of SS2343 stainless steel. Windows were made of Spectrosil 2000 quartz glass. The test section was designed such that it may be rotated around its air-flow axis without removing it from the rig.

The orange air inlet piece shown in Figure 77 was designed to gradually transition from a circular to a rectangular cross section. The length and inlet diameter of this transition piece was optimized using a RANS solver. The inlet piece was produced in an EDM. Resulting velocity profiles were measured with PIV. The PIV setup can be seen in Chapter 9.4. Results are shown in Paper 8.

PDA was subsequently used to characterize the spray. The PDA setup can be seen in Chapter 9.2. Results are in Papers 8 and 9.

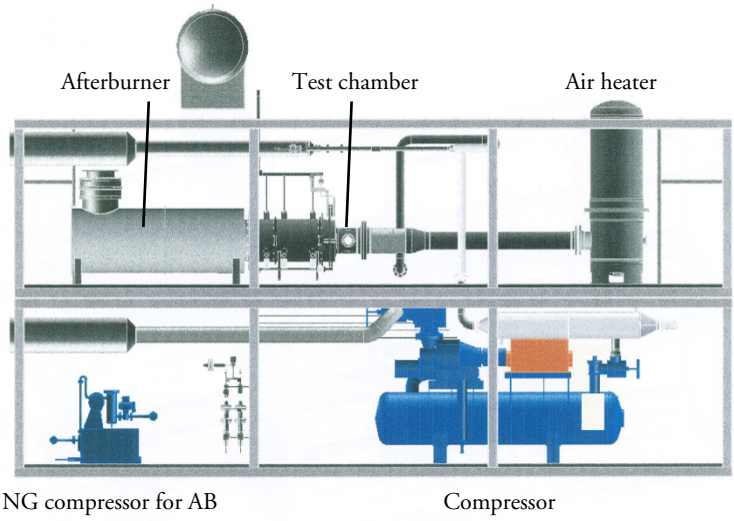

Figure 76: DESS rig

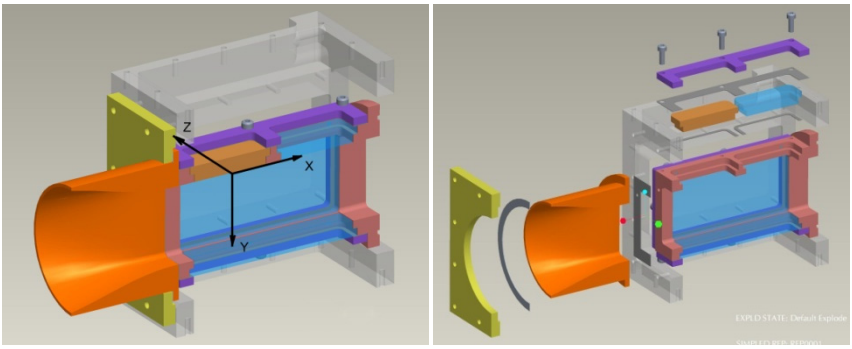

Figure 77: 40·30 mm test section

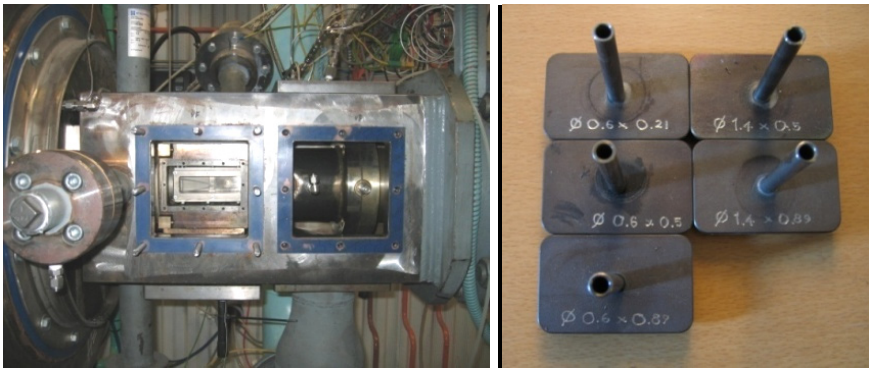

Figure 78: Test section in DESS test chamber (left), Replaceable liquid injection holes marked with ∅ x L (right)

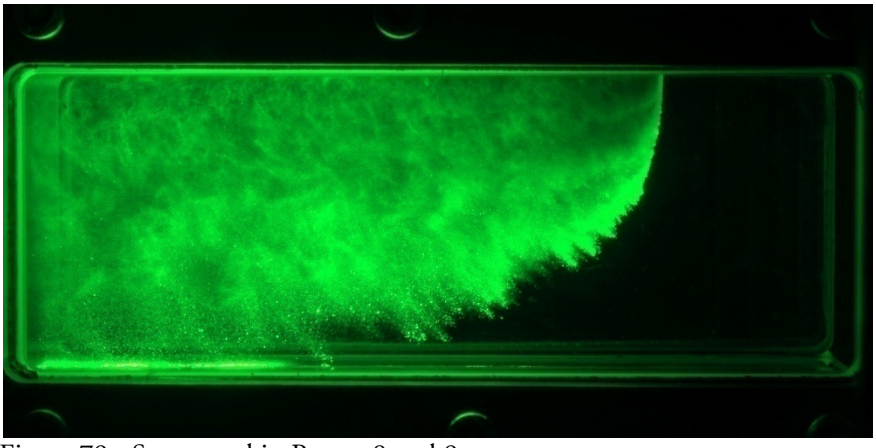

Figure 79: Spray used in Papers 8 and 9

8 Process simulation

Process simulation involves making a computer model of discrete components and connecting them into a network. The components (a.k.a. nodes or units) may represent reaction tanks, generators, electric motors, IC engines, pumps, compressors, turbines or individual stages within a turbine. The connectors are typically pipes or ducts in the case where a fluid is transported from one node to another, but may also be electric current conduits. It follows that energy may also be conveyed from node to node. A process simulation tool is thus an incredibly versatile tool that is used in fields such as chemistry, electricity, economics and engineering. In particular, process simulators may be used to simulate energy conversion devices such as gas turbines or complete plants such as a combined cycle plant or an IGCC plant.

A computer package that allows these kinds of simulations typically consists of two parts, a model development environment and a process simulation environment. In the first, models may be built. These each consist of a set of variables, constants and equations, describing the components behavior as it is subjected to a set of boundary constraints defined by the connectors. In the process simulation environment a complete model is built with components and connectors. An example of a model is seen in Figure 80. The model is then translated into a system of equations, which may be, and most often are, non-linear. The system may contain several thousand equations if a large plant is simulated. Since the equations may be non-linear, Gaussian elimination will not be possible. The approach taken is thus to cast each equation to be equal to zero and use a Newton-Raphson solver to find concurrent roots to all equations.

Each equation is thus written as:

$$f_1(x_1, x_2, x_3, ...x_n, c_1, c_2, c_3, ..., c_n) = 0 \tag{8.1}$$

$$f_2(x_1, x_2, x_3, ...x_n, c_1, c_2, c_3, ..., c_n) = 0 \tag{8.2}$$

…

where x_n are variables and c_n are constants.

For there to be a solution, the number of equations must equal the number of variables. Each equation and variable must also provide unique information of the underlying problem. If not, the equation system becomes structurally singular.

The Newton-Raphson solver relies on initial guesses for all variables. These must be sufficiently close to the correct solution such that the solver can find the correct root. Convergence may also be difficult if the equations contain local extremes close to the desired root. Difficulties also arise from discontinuities in the equations and their derivatives. Equations cannot have a constant solution over an interval of variable values either since this means that a unique solution doesn't exist. Equations having zero derivatives in intervals close to the solution are also problematic.

The complete network used in Papers 5 and 6 is shown in Figure 80.

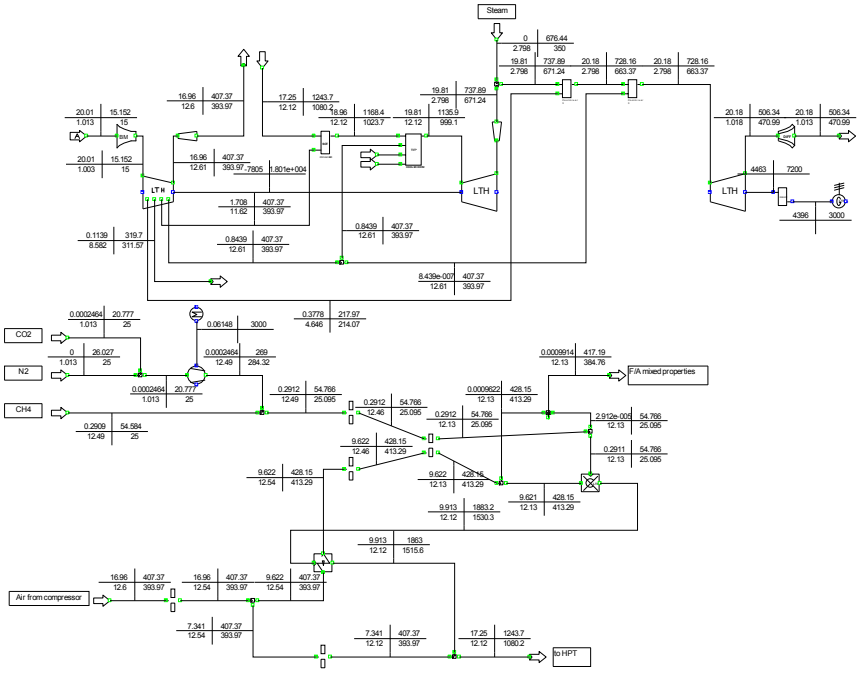

Figure 80: IPSE-Pro model of Volvo VT4400 gas turbine (Papers 5 and 6)

9 Experimental methods

9.1 LDA/PDA

LDA and PDA are point measurement techniques used to measure particle velocities and in the case of PDA, sizes too. PDA is an extension of LDA so LDA is first described.

LDA stands for Laser Doppler Anemometry. The technique utilizes the fact that the frequency from a monochromatic and coherent light source, such as a laser, will change as it bounces off a moving target. This is the Doppler shift. Figure 81a shows an incoming beam along the unit vector $\mathbf{e}_i$. The frequency of the incident light is f_i. The particle has a velocity $\mathbf{U}$. The frequency of the scattered light f_s can be written:

$$f_S = f_i \frac{1-\mathbf{e}_i\left(\frac{\mathbf{U}}{c}\right)}{1-\mathbf{e}_s\left(\frac{\mathbf{U}}{c}\right)} \tag{9.1}$$

where $\mathbf{e}_s$ is the unit vector in the direction of the scattered light and c is the speed of light. For moderate particle velocities (up to supersonic), the frequency of the scattered light will, however, only shift slightly in relation to the frequency of the incident light. This may be overcome by shining two rays from different angles on the particle. Figure 81b shows this case with $\mathbf{e}_1$ and $\mathbf{e}_2$ being the unit vectors for the two incident rays. Since the velocity of the particle differs in the $\mathbf{e}_1$ and $\mathbf{e}_2$ directions, the mixed scattered light will contain a beat frequency reflecting the difference in scattered frequencies from the two light sources. This may be written as:

$$f_D = \frac{2\sin\left(\frac{\theta}{2}\right)}{\lambda} \cdot u_x \tag{9.2}$$

where f_D is the beat- or Doppler frequency, λ is the wavelength of the two incident laser beams, θ is the angle between beams and u_x is the particle velocity in a perpendicular direction to the bisector of the two laser beams and lying in the plane of the two beams (vertical direction in Figure 81b). Measuring f_D will thus yield u_x. It is worth noting that $\mathbf{e}_s$ does not appear in this expression. This means that the direction toward the receiving optics may be chosen freely.

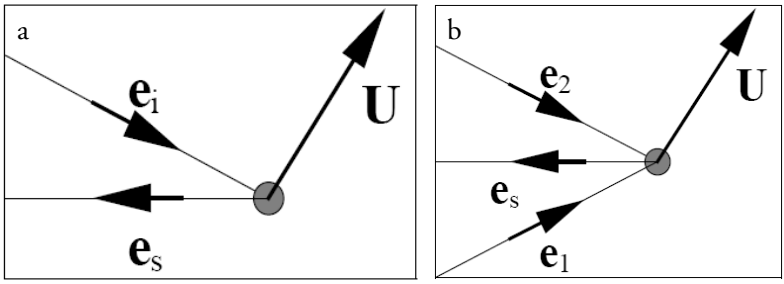

Figure 81: Coherent light scattered from particle [101]

An alternative way to view the situation is to look at the interference pattern at the intersection of the two beams. A set of light and dark bands, stacked in the x-direction, results. This may be seen in Figure 82. Each tier is called a fringe and the distance between them may be computed as:

$$\delta_f = \frac{\lambda}{2\sin\left(\frac{\theta}{2}\right)} \tag{9.3}$$

The light coming off a particle moving in the x-direction will vary in intensity at the frequency:

$$f_D = \frac{u_x}{\delta_f} = \frac{2\sin\left(\frac{\theta}{2}\right)}{\lambda} \cdot u_x \tag{9.4}$$

This is the same result as in Equation (9.2).

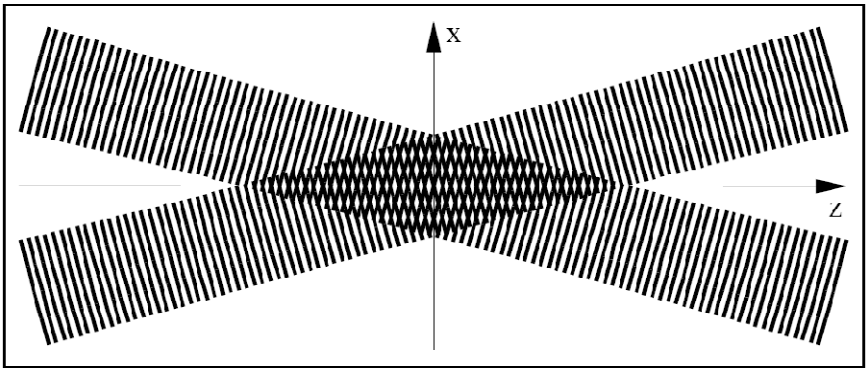

Figure 82: Interference pattern [101]

The light signal coming off the particle is picked up with a photo-multiplier detector (Figure 83). The PM-tube converts the energy contained in each photon to an electron stream at the photocathode using the photoelectric effect. Each electron is then multiplied by the process of secondary emission to produce a signal proportional to the light intensity.

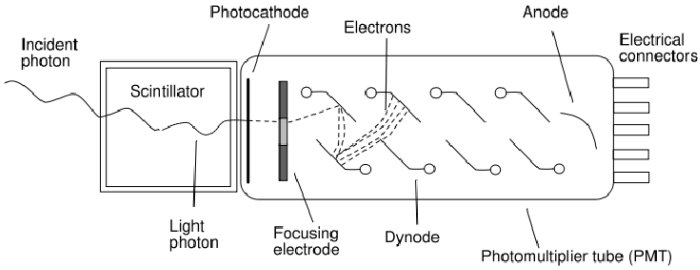

Figure 83: PM tube [Wiki]

The signal from the PM-tube as one particle passes through the measurement volume is shown in Figure 84a. This is called the burst signal. If the low-frequency component, corresponding to the entire passage is filtered out, the signal takes on the shape seen in Figure 84b. The low low-frequency component is called the pedestal. It is used to trigger measurement of each passing particle. The frequency seen in Figure 84b is proportional to the particle velocity according to Equation (9.2).

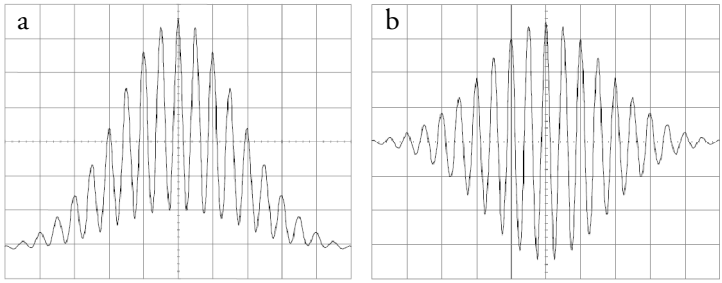

Figure 84: Doppler signal and filtered Doppler signal [101]

Several measurement setup configurations exist where the receiving optics is positioned at different locations in relation to the emitting optics. The simplest setup to use has the receiving and emitting optics integrated into one unit where everything is aligned. This is called backscatter LDA and is shown in Figure 85. The various components are:

- Laser which provides a directional monochromatic and coherent light
- Beam splitter to create two identical beams
- Bragg cell which shifts the frequency of one of the beams
- Front lens which focuses the two beams at an intersecting measurement volume
- Optics for the receiver
- Receiver (PM-tube)

Since most of the light is scattered in the forward direction, it may be difficult to obtain a good signal-to-noise ratio with this setup. With very small seeding particles it may therefore be necessary to go with forward scattering LDA, where a separate receiver is positioned opposite to the emitting optics. Situations where this scheme may be a better alternative are high-speed flows and transient phenomena.

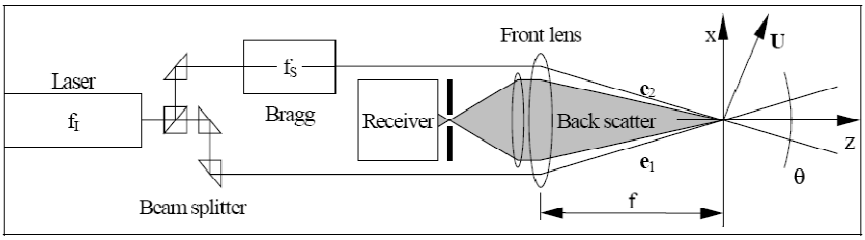

Figure 85: Backscatter LDA [101]

The Bragg cell introduces a frequency shift f_0 to one of the beams. This is used to resolve the velocity ambiguity resulting from a stationary set of fringes. The Bragg cell will give the fringes an x-velocity proportional to the shift frequency. Figure 86a shows the situation without a Bragg cell. Here the measured velocity is either positive or negative by the same amount. There is no way of telling which is correct unless it is obvious from the flow situation. By adding the frequency shift to Equation (9.2), positive as well as negative velocities may be determined within a given range according to Figure 86b.

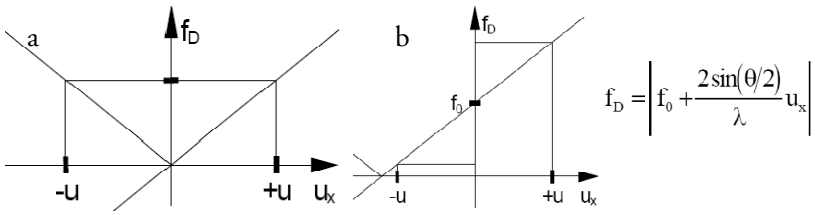

Figure 86: Effect of Bragg cell frequency shift [101]

By positioning the receiver to the side, off-axis scattering is obtained. This may be used to cut out a small slice of the measurement volume, thereby suppressing portions being traversed by different flow velocities or being out of focus. This reduces noise. A typical example where this setup may be useful is close to walls where reflections may be troublesome. An example of this setup can be seen in Figure 87 where φ defines the off axis angle.

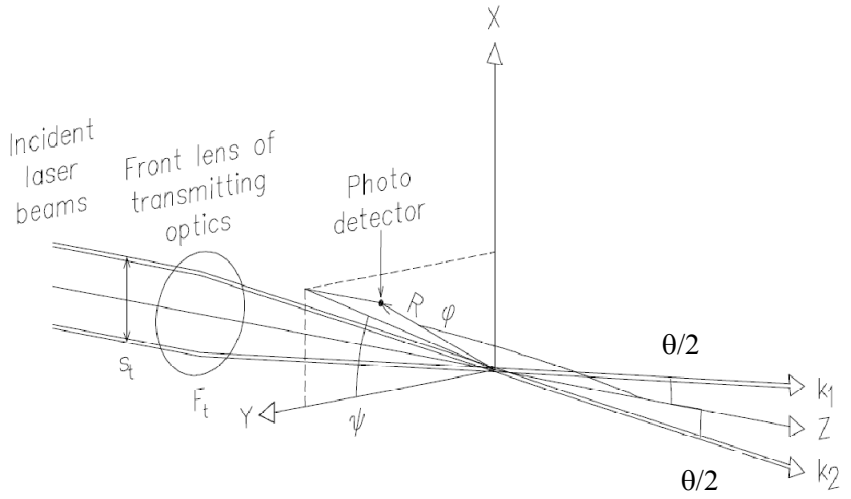

Figure 87: Off-axis LDA defined by φ, elevation defined by ψ [101]

Two or three single-channel LDA systems may be combined to measure more velocity components for each particle. The signals from such measurements are generally separated by using different laser lines and color filters.

PDA, which stands for Phase Doppler Anemometry, adds the capability to measure particle diameters in addition to velocities. Figure 88a shows scattered light from a particle seen from two directions. Figure 88b shows the resulting phase shift between the two wave trains being scattered from the particle. The phase shift is first order proportional to droplet size, but also dependent on the geometry of the setup (Figure 87) and scattering mode. Three of these are shown in Figure 89. The phase shift may be written [102]:

$$\Phi_{12} = \frac{2\pi\sqrt{2}}{\lambda} D \left(\sqrt{1 - \cos\psi\cos\varphi\cos\frac{\theta}{2} + \sin\psi\sin\frac{\theta}{2}} - \sqrt{1 - \cos\psi\cos\varphi\cos\frac{\theta}{2} - \sin\psi\sin\frac{\theta}{2}} \right) \tag{9.5}$$

for reflection and:

$$\Phi_{12} = \frac{4\pi}{\lambda} D \left(\sqrt{1 + m^2 - m\sqrt{2}\sqrt{1 + \sin\Psi\sin\frac{\theta}{2} + \cos\Psi\cos\varphi\cos\frac{\theta}{2}}} - \sqrt{1 + m^2 - m\sqrt{2}\sqrt{1 - \sin\Psi\sin\frac{\theta}{2} + \cos\Psi\cos\varphi\cos\frac{\theta}{2}}} \right) \tag{9.6}$$

for 1st order refraction, where m is the ratio of refractive indices.

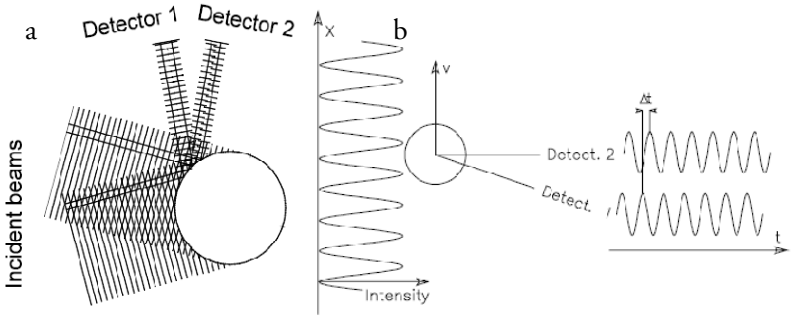

Figure 88: Phase shifted signal when looking from two directions [101]

PDA may thus be set up to work on reflected light or, in the case where the particles are translucent, refracted light. Refracted light may either be first- or second order, meaning that the light passes in and directly out of the particle, or that there is an intermediate reflection (Figure 89).

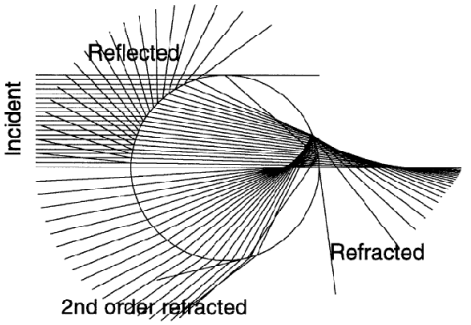

Figure 89: Plane wave reflection and refraction in spherical particle (up to 2nd order) as seen in the incidence plane [101]

The most common setup is first order refraction. The optimum angle for this is the Brewster angle. The reason for this is that reflected and refracted light will interfere adversely. This will result in poor signal quality. The Brewster angle is defined as:

$$\varphi_B = \tan^{-1} m \tag{9.7}$$

At the Brewster angle, the reflected component is perpendicularly polarized with regards to the incidence plane. This contribution to the total signal at the detectors can easily be removed with a linear polarizing filter leaving only refracted light to detect. Operating at the Brewster angle places the detector at φ=50-75° off axis depending on the ratio of refractive indices m.

Figure 90 left shows a conventional PDA system. Here the two detectors are spaced apart in the elevation plane. The two detectors may also be arranged to lie in the off-axis plane. This is the planar PDA shown to the right.

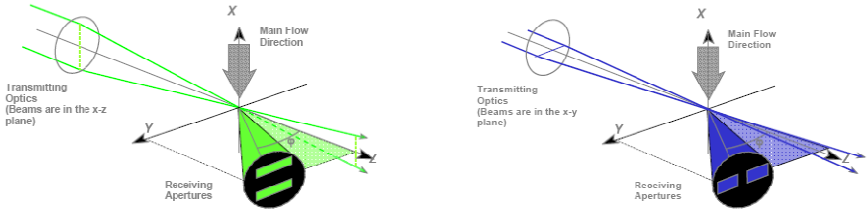

Figure 90: conventional PDA left and planar PDA right [101]

The two systems may be combined yielding a Dual PDA system capable of measuring two velocity components (x and y) and particle sizes based on curvature in two perpendicular directions. The combined instrument is shown in Figure 91.

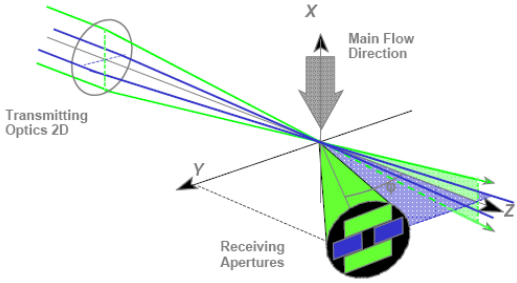

Figure 91: Dual PDA system [101]

If the detected phase shift exceeds one wave-length it becomes impossible to uniquely determine the particle size. In a Dual PDA system this ambiguity may be resolved using the planar PDA, having a lower phase difference to size response, to determine the approximate size. The conventional PDA is then used for higher accuracy (Figure 92).

Each system measures the curvature of the particle in a direction perpendicular to the other. This may be used as a means of rejection of non-spherical particles if reported sizes differ too much.

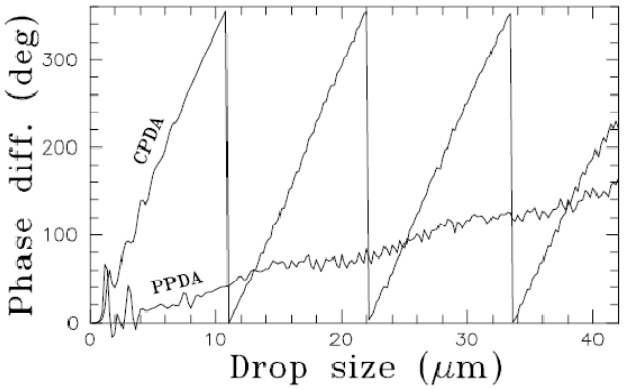

Figure 92: Resolution of size ambiguity in conventional PDA using PPDA [101]

9.2 PDA/Photography setup in the DESS rig

The DESS rig, described in Chapter 7.2, was used to measure the spray in cross-flow investigated in Papers 8 and 9. For PDA measurements and photography, the spray was injected horizontally towards the XYZ traverse shown in Figure 93.

A Dantec Classic PDA system was used. This system differs from the Dual PDA described above in that particle size validation is done with three detectors in one plane. The second direction channel thus operates as a pure LDA system. The PDA system was arranged such that the transmitting optics was directly above the spray and aiming straight down. The receiving optics was tilted down 15° from the horizontal plane such that the off-axis angle φ became 75°. This was as close to the calculated Brewster angle of 74° as was possible without losing optical access to the top half of the spray; -the part measured for Papers 8 and 9. The calculated confidence of linearity between phase angle and diameter is for this setup 97.7%.

In order to obtain the highest diameter range, the angle adjustment micrometer screw at the back of the receiving optics was set to 2 mm. This allowed for a maximum droplet diameter of 106.1 μm.

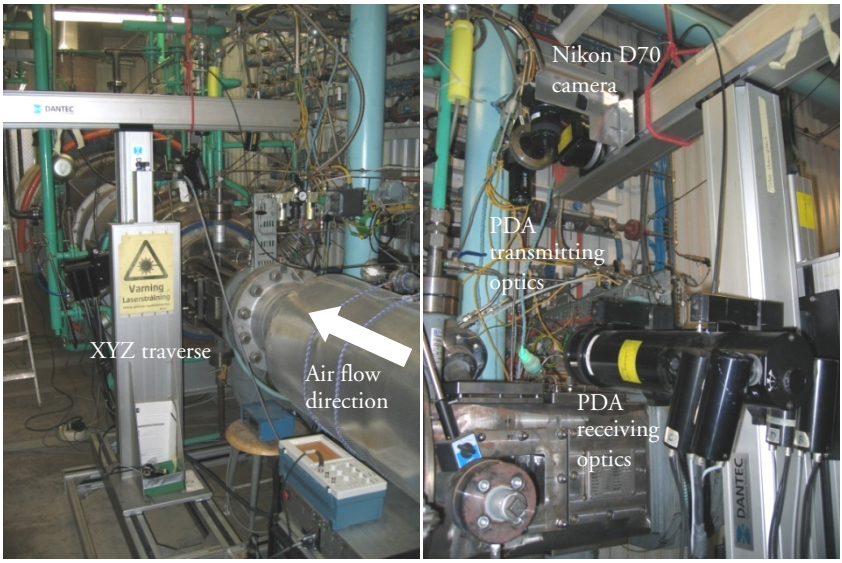

Figure 93: PDA and still photography setup

Figure 94: Closeup of PDA transmitting optics and Nikon D70s DSLR (left) and illumination laser for still photography (right)

The system operated at the following wavelenths:

- x channel (acc. to Figure 77): 514.5 nm
- y channel (acc. to Figure 77): 488 nm

In addition the following data/settings applied for the used PDA setup:

- Focal length of emitting optics: 400.5 mm
- Focal length of receiving optics: 310 mm
- Beam distance: 38 mm (no beam expansion).
- Beam diameter: 1.4 mm
- Fringe direction: negative

PM tube voltages were adjusted ad hoc until calibration was successful.

The Measurement ranges for the particle velocities were set to:

- -54.3 to 190.0 m/s for the x direction (highest bandwith)
- -30.9 to 30.9 m/s for the y direction
- Frequency shift: 40 MHz
- Signal gain: High

The recommended S/N ratio for 24 and more fringes is -3 dB. The setup used had 36 fringes. The S/N ratio was, after some experimentation, set to -6 dB. This produced high data rates with acceptable validation statistics.

Diameter and x velocity validation was switched on. y velocity validation was switched off since the blue laser was very weak and produced poor PM tube level readings. y velocity data wasn't of prime importance either. The diameter spherical validation band was set to 10%. Validation data rate was 32 kHz in the core of the spray and dropping off towards the peripherial regions of the spray.

A Nikon D70s 6 MP Digital Single Lens Reflex camera with a 60 mm F/2.8 D Nikkor macro lens set at f=20–29 was mounted on the traverse adjacent to the PDA transmitting optics in order to facilitate transition between PDA measurements and photography. A Continuum MiniLite pulsed Nd:YAG PIV laser with Lavision sheet optics was used to illuminate the photos. This is shown in Figure 94. The laser was operating at 532 nm at the reduced power setting.

9.3 PIV

Particle Image Velocimetry is a technique used to measure and compute velocity fields from two exposures of a flow taken with a known time interval between them. The technique is normally two-dimensional, but may be extended to three dimensions with an extra camera and a thickened laser sheet.

In the two-dimensional case, the flow is illuminated with a double-pulsed laser equipped with sheet optics. A digital camera is used to record two images of the illuminated sheet either as separate recordings or as a double exposure. The former case is the most versatile since flow directions may be deduced from the order in which the exposures were taken. The camera is in a basic setup arranged perpendicularly to the laser sheet according to Figure 95. In order to make the flow visible, it is seeded with

particles. For the seeding particles to be able to follow the flow, they should be small and with a density close to the fluid. This may be expressed with the dimensionless Stokes number:

$$St = \frac{\tau_v}{\tau_f} \tag{9.8}$$

where τ_v is a characteristic time for the particle and τ_f is characteristic time for the fluid. τ_v is:

$$\tau_v = \frac{\rho_d D^2}{18\mu_c} \tag{9.9}$$

where ρ_d is the particle density and μ_c is the fluid dynamic viscosity. τ_f is not so straight forward as it represents a characteristic time over which a velocity change occurs in the fluid. It is often a convection time associated with flow past an obstacle and may then be calculated as follows:

$$\tau_f = \frac{D_t}{U} \tag{9.10}$$

where D_t is a characteristic length of the obstacle and U is a characteristic flow velocity. In the case where turbulence is investigated, D_t may be seen as some characteristic size of the turbulent eddies of interest. With $St \ll 1$ the particles will follow the flow well as it accelerates, decelerates or changes direction. It may then be said to represent the fluid flow velocity field in the measured plane.

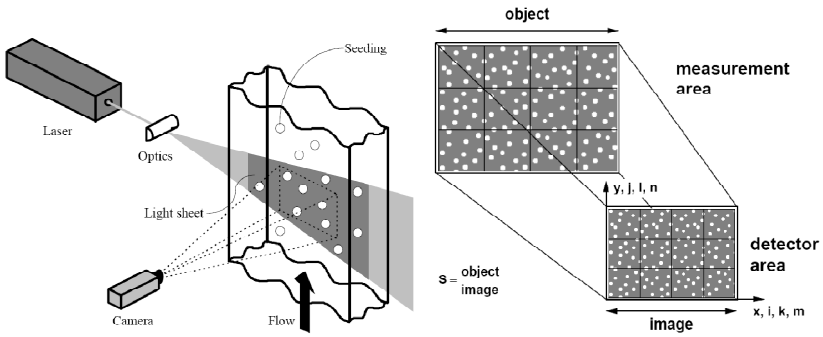

Figure 95: Basic PIV setup (left) and subdivision of field of view into interrogation areas (right) [103]

The images taken with the camera typically cover a large measurement area of the flow, and velocities will vary accordingly. Each image is therefore broken up into sub-regions called interrogation areas, each producing a vector representing velocities in the x- and y directions. Ideally the velocity field within each interrogation area should be uniform. The translation of each area of image B in relation to image A corresponding to the best match

between areas may then be computed. This may be expressed as a cross-correlation:

$$C(\delta_x, \delta_y) = \sum_{x=0}^{\delta_x - 1} \sum_{y=0}^{\delta_y - 1} A_{x,y} B_{x+\delta x, y+\delta y} \tag{9.11}$$

where the highest peak of C corresponds to the best match and δ_x and δ_y for this peak are the displacements. If the delay between exposures is known the velocity components become:

$$U = \frac{\delta_x}{t}, \; V = \frac{\delta_y}{t} \tag{9.12), (9.13}$$

In the case where only one image with two exposures is available, each image interrogation area is auto-correlated yielding three symmetric peaks with the mid-peak being the highest. One of the side peaks represents the sought velocities. The two cases may be seen in Figure 96.

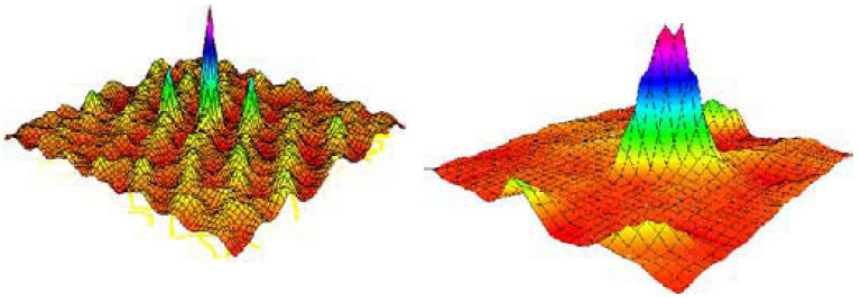

Figure 96: Auto-correlation peaks for C left and cross-correlation peak for C right [104]

Computing correlations according to Equation (9.11) is very time consuming due to the multitude of multiplications and additions required. FFT techniques are therefore preferred and offer substantial time-savings.

Each image typically consists of 2^{10} (1024) pixels in each direction. Interrogation areas are typically chosen to be 2^7 (128) to 2^5 (32) pixels in each direction. This yields 8x8 to 32x32 interrogation areas. The actual number of interrogation areas is chosen based on particle density and velocities. Displacement of particles within each area should be approximately 1/4 of the size of an interrogation area. Inspecting Equation (9.11) it is clear that more pixel combinations are multiplied and added for less translation. There is therefore a bias toward finding small displacements. This "peak locking" may be overcome with an iterative scheme where interrogation area sizes are reduced consecutively.

In order to improve statistical accuracy, many image pairs are used to calculate velocities. Arithmetic averaging yields the final result. Higher moments may be obtained in this step; viz. one velocity component and the corresponding turbulence intensity are shown in Paper 8.

The PIV method is spatially discrete, i.e. it operates on a finite set of pixels, each with a range of allowable intensity values typically in the range 2^{10} to 2^{12} bits. Since small particles are imaged as Airy disks covering several pixels, the intensity information from adjacent pixels may be used to resolve displacements on a sub-pixel level. The Airy disk has a Gaussian distribution. By matching intensities in three adjacent pixels to a Gaussian distribution curve, positions may be resolved to within 0.1 pixel [105].

9.4 PIV setup in the DESS rig

A Dantec Flowmap PIV system was used to characterize the air velocity profile and turbulent velocities within the test section designed for the DESS rig (Chapter 7.2). The PIV setup can be seen in Figure 97. The system consisted of a Quantel/Big-Sky CFR200 twin cavity pulsed illumination laser with sheet optics. The illumination laser was mounted on an x-y table on the blue stand seen in Figure 97. An arm holding a mirror reflecting the sheet 90° down was attached to the x-y table. By rotating the laser sheet optics, a sheet aligned with, or perpendicular to the air-flow could be produced. The latter would be useful for stereo-PIV; something that was ruled out later due to laser break-down and lack of time. The sheet optics was set to approximately 3 mm thickness at the test section.

The data analysis recipe used for PIV was:

- Cross-correlation
  - 50% overlap in horizontal and vertical direction
  - Top hat filter with no DC component
- Range validation
  - 15 to 130 m/s in x direction (acc. to Figure 77)
  - -15 to 70 m/s in y direction (acc. to Figure 77)
- Peak validation
  - Peak height ratios: 1.2
- Vector statistics on all valid vectors (including substituted)

The interrogation area sizes and overlaps were played with a little in order to get good results. This is a compromise game between having

enough seeding particles available for analysis and spatial resolution of the measurements.

A Dantec HiSense PIV/PLIF camera and a camera control were used (Figure 97 right) in conjunction with a Flowmap PIV 2200 processor. Control was from a regular PC running Dantec Flow Manager 3.62 software.

A SCITEK PS-10 drum seeder (seen in Figure 97) was used to inject AEROSIL 200 (SiO_2 by Degussa) about 2 m upstream of the test section. The seeder, rated to 10 bar, was pressurized from a 200 bar air bottle with a reduction valve. The seeding air (typically a couple of g/s) was metered and added to the overall air-flow. A fairly sparse seeding flow proved to work best. A denser flow would quickly destroy visibility as the seeding particles attached readily to the windows.

Measurements were done both for the y=20 mm, z=0 mm and z=6 mm planes (coordinate system according to Figure 77). The measurement plane of interest was selected by rotating the test section accordingly. Results are reported in Paper 8.

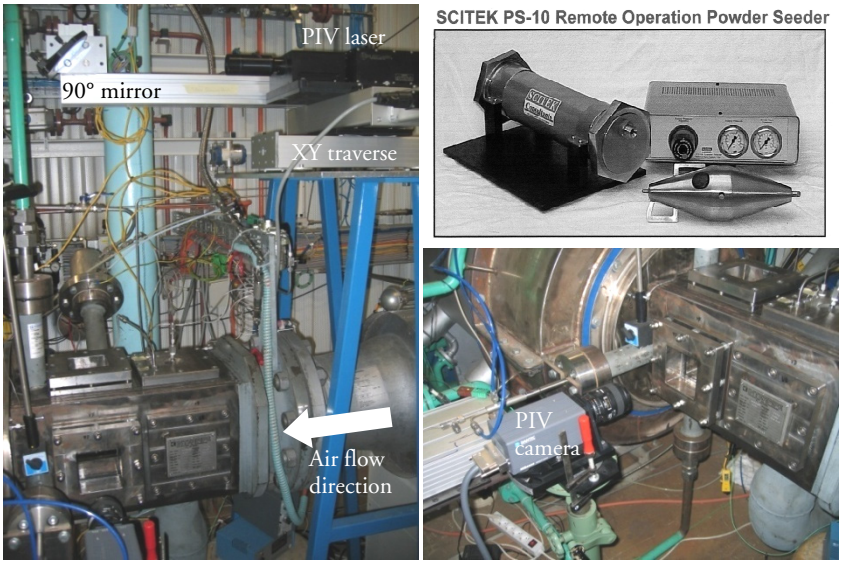

Figure 97: PIV setup and seeding equipment

10 Bibliography

[1] California Air Resources Board web "History of Air Quality Management in California - Key Events", July 18 2008 http://www.arb.ca.gov/html/brochure/history.htm

[2] Haagen-Smit, A., J., "Air Conservation", Science, New Series, Vol. 128, No. 3329 (Oct. 17, 1958), pp. 869-878

[3] U. S. Environmental Protection Agency web, "Acid Rain", December 10th, 2008

[4] Solomon, S., D. Qin, M. Manning, Z. Chen, M. Marquis, K.B. Averyt, M. Tignor and H.L. Miller (eds.), "Technical Summary. In: Climate Change 2007: The Physical Science Basis. Contribution of Working Group I to the Fourth Assessment Report of the Intergovernmental Panel on Climate Change", Cambridge University Press, Cambridge, United Kingdom and New York, NY, USA, 2007

[5] "Inventory of U.S. Greenhouse Gas Emissions and Sinks: 1990 - 2004", U.S. Environmental Protection Agency, EPA 430-R-06-002, 2006

[6] Slanina, J., Warneck, P., Bazhin N. M., Akimot H., Kieskamp W. M., "Assessment of Uncertainties in the Projected Concentrations of Methan in the Atmosphere", Pure & Appl. Chem., Vol. 66, No. 1: 137-200, 1994

[7] Intergovernmental Panel on Climate Change, "Climate Change 2001", Cambridge University Press, ISBN: 0521 80767 0, 2001

[8] Houghton, R. A., J. L. Hackler., "Carbon Flux to the Atmosphere from Land-Use Changes: 1850 to 1990" ORNL/CDIAC-131, NDP-050/R1, Carbon Dioxide Information Analysis Center, U.S. Department of Energy, 2001

[9] Liu, H., Feng, B., Lu, J., Zheng, C., "Coal Property Effects on N2O and NOX Formation from Circulating Fluidized Bed Combustion of Coal", Chem. Eng. Comm., 192:1482–1489, 2005

[10] Gutierrez, M., J., F., Baxter, D., Hunter, C., "Nitrous oxide (N2O) emissions from waste and biomass to energy plants", Waste Manage Res. 2005: 23: 133–147, 2005

[11] Glassman, Irvin, "Combustion, Third Edition", ISBN 0-12-285852-2, Academic Press, 1996

[12] Steele, R., C., Malte, P. C., Nicol, D., G., Kramlich, J., C., "NO_X and N_2O in Lean Premixed Jet-Stirred Flames", Combustion and Flame, Volume 100, Number 3: 440-449, 1995

[13] Etemad, S., Smith, L., Burns, K., "System Study of Rich Catalytic/Lean burn (RCL®) Catalytic Combustion for Natural Gas and Coal-Derived Syngas Combustion Turbines", DOE Contract No. DE-FG26-02NT41521 Final Report, 2004

[14] Goldschmidt, B., "Deponigaskvalitet – Krav och Övervakning", Sycon Report: UGdt020605(deponigas), 2002

[15] Petit, J.R., Jouzel, J., Raynaud, D., Barkov, N., I., Barnola, J.-M., Basile, I., Bender, M., Chappellaz, J., Davis, M., Delayque, G., Delmotte, M., Kotlyakov, V., M., Legrand, M., Lipenkov, V., Y., Lorius, C., Pépin, L., Ritz, C., Saltzman, E., and Stievenard, M., "Climate and atmospheric history of the past 420,000 years from the Vostok ice core, Antarctica", Nature 399: 429-436, 3 June 1999

[16] Hansen, J., Sato, M., "Greenhouse Gas Growth Rates", Proc. of the National Academy of Sciences of the United States of America, Vol. 101, No. 46 (Nov. 16, 2004), pp. 16109-16114

[17] Todaro, R., M. (Editor), "Stratospheric Ozone - An Electronic Textbook", http://www.ccpo.odu.edu/SEES/ozone/oz_class.htm, December 10th, 2008

[18] Crutzen, P., J., "The Role of NO and NO_2 in the Chemistry of the Troposphere and Stratosphere", Ann. Rev. Earth Planet. Sci. 1979. 7: 443-72

[19] Farman, J., C., Gardiner, B., G., Shanklin, J., D., "Large Losses of Total Ozone in Antarctica Reveal Seasonal ClO_X/NO_X Interaction", Nature Vol. 315, 16 May 1985 pp 207-210

[20] Newman, P.A., Lait, L.R., Schoeberl, M.R., "The morphology and meteorology of southern hemisphere spring total ozone mini-holes" Geophys. Res. Lett. 15, 923–926, 1988

[21] Ennis, C., A. (coordinating editor), "Scientific Assessment of Ozone Depletion: 2006", World Meteorological Organization, Global Ozone Research and Monitoring Project—Report No. 50, 2007

[22] Weatherhead E., C., Bech Andersen S., "The search for signs of recovery of the ozone layer", Nature, Vol 441/4, May 2006: 39 – 45, 2006

[23] Conaire, M., O., Curran, H., J., Simmie, J., M., Pitz, W., J., Westbrook, C., K., "A Comprehensive Modeling Study of Hydrogen Oxidation", Int. J. Chem. Kinetics, Vol. 36, Issue 11: 603 – 622, 2004

[24] Bai, X-S, "Turbulent Combustion – Lecture Notes", Lund University, 2006

[25] Omaye, S., T., "Metabolic Modulation of Carbon Monoxide Toxicity", Toxicology 180, pp 139-150, 2002

[26] Lefebvre, A. H., "Gas Turbine Combustion", Taylor & Francis, ISBN 1-56032-673-5, 1998

[27] Svenskt Gastekniskt Center AB, "Energigaser och Miljö", ISBN 91-85207-02-0, 2005

[28] Loo, S., Koppejan, J., "Handbook of Biomass and Combustion", Twente University Press, ISBN 90-365-17773-7, 2003

[29] Zevenhoven, R., Kilpinen, P., "Control of pollutants in flue gases and fuel gases, 2nd edition", ISBN 951-22-5527-8, 2002

[30] Miller, J., A., Kee, R., J., "Chemical Kinetics and Combustion Modeling", Annu. Rev. Phys. Chem. 41: 345-87, 1990

[31] Borghi, R., Destriau, M., "Combustion and Flames", Éditions Technip, ISBN 2-7108-0740-8, 1995

[32] Nilsson, P., "A Level-set Flamelet Library Model for Premixed Turbulent Combustion", Doctoral Thesis, Lund University, ISRN LUTMDN/TMKV--1028--SE, 2001

[33] Engdar, U., "CFD Modeling of Turbulent Flows in Industrial Applications with Emphasis on Premixed Combustion in Gas Turbines", Doctoral Thesis, Lund University, ISBN 91-628-6380-0, 2005

[34] Walsh, P., P., Fletcher, P., "Gas Turbine Performance", Blackwell Science Ltd., ISBN 0-632-04874-3, 1998

[35] Mattingly, J., D., "Elements of Gas Turbine Propulsion", McGraw-Hill Inc., ISBN 0-07-912196-9, 1996

[36] Duwig, C., Fuchs, L., "Study of Flame Stabilization in a Swirling Combustor Using a New Flamelet Formulation", Combust. Sci. and Tech., 177: 1485–1510, 2005

[37] Lucca-Negro, O., O'Doherty T., "Vortex breakdown: a review", Prog. Energy Combust. Sci. Vol. 27: 431 – 481, 2001

[38] Anacleto, P. M., Fernandes, E. C., Heitor, M.V., Shtork, S. I., "Swirl Flow Structure and Flame Characteristics in a Model Lean Premixed Combustor", Combust. Sci. and Tech. 175: 1369 – 1388, 2003

[39] Syred, N., "A Review of Oscillation Mechanisms and the Role of the Precessing Vortex Core (PVC) in Swirl Combustion Systems", Prog. Energy Combustion Sci. 32: 93–161, 2006

[40] Blomstedt, M., Navrotsky V., Lindman, O., "Field Experience From Sgt-600 2nd Generation of Low Emission Combustion Chamber" Siemens Finspong, 2006

[41] Esbeck, D., W., Gates S., Schneider, P., H., "Industrial Advanced Turbine Systems Program Overview" Annual ATS Report to DOE, Solar Turbines Incorporated

[42] Rayleigh, J., W., S., "The Theory of Sound 2nd revised edition", pp 225-235 Dover, ISBN 978-0486602929, 1969

[43] Lieuwen, T., C., "Combustion Instabilities in Gas Turbine Engines", American Institute of Aeronautics and Astronautics Inc., ISBN 1-56347-669-X, 2005

[44] Durox, D., Schuller, T., Noiray, N., Birbaud, A., L., Candel, S., "Rayleigh Criterion and Acoustic Energy Balance in Unconfined Self-sustained Oscillating Flames", Combustion and Flame 156, pp 106–119, 2009

[45] Cheng, D., Y., "The Distinction Betwen The Cheng And The Stig Cycles", ASME GT 2006-90382, 2006

[46] Cheng, D., Y., "Reduction of NOX to Below 2 PPM in a Diffusion Flame", ASME GT 2003-38208, 2003

[47] Lindquist, T., "Evaluation, Experience and Potential of Gas Turbine Based Cycles with Humidification", Doctoral Thesis, Lund University, ISBN 91-628-5330-9, 2002

[48] Thern, M., "Humidification Processes in Gas Turbine Cycles", Doctoral Thesis, Lund University, ISBN 91-628-6696-6, 2005

[49] Air Force Research Laboratory Wright-Patterson AFB OH, Propulsion Directorate, "Innovative Engine Technology Demonstrates Potential to Revolutionize Turbine Engine Performance"

[50] Marshall, R., L., Canuel, G. E. Sullivan D., J., ""Augmentation Systems for Turbofan Engines", Comb. In Adv. GT Syst. Cranfield Intl. Symp. Series Vol 10, Pergamon Press, 1967

[51] Sathiah, P., "Modelling Effects of Flame Development on Stationary and Oscillating Premixed Turbulent Combustion", Doctoral Thesis, Chalmers University, ISBN: 91-7291-830-6, 2006

[52] Wilcox, D., C., "Turbulence Modeling for CFD", DCW Industries Inc., ISBN: 0-9636051-5-1, 2000

[53] Zimont, V., Polifke, W., Bettelini, M., Weisenstein, W., 1998, "An Efficient Computational Model for Premixed Turbulent Combustion at High Reynolds Numbers Based on a Turbulent Flame Speed Closure", Transactions of the ASME Vol. 120, July 1998 pp. 526 – 532, 1998

[54] Peters, N., "Turbulent Combustion", Cambridge University Press, ISBN: 0-521-66082-3

[55] Yang, J-T., Yen, C-W., Tsai, G-L., "Flame Stabilization in the Wake Flow Behind a Slit V-Gutter", Combustion and Flame 99: 288-294, 1994

[56] Yang, J-T., Tsai, G-L., "The Wake Flow Structure of an Open-Slit V Gutter" Exp. Thermal and Fl. Sci. 5:685-696, 1992

[57] Zarzalis, N., Ripplinger, T., Hohmann, S., Hettel, M., Merkle, K., Leuckel, W., Klose, G., Meier, R., Koch, R., Wittig, S., Carl, M., Behrendt, T., Hassa, C., Meier, U., Lückerath, R., Stricker, W., "Low-NOx Combustor Development pursued within the scope of the Engine 3E German national research program in a cooperative effort among engine Manufacturer MTU, University of Karlsruhe and DLR German Aerospace Research Center", Aerospace Science and Technology 6 (2002) 531–544, 2002

[58] Flamme, M., "New Combustion Systems for Gas Turbines (NGT)", Applied Thermal Engineering 24 (2004) 1551–1559, 2004

[59] Wang, Y., D., Huang, Y., McIlveen-Wright D., McMullan, Hewitt, J., N., Eames, P., Rezvani, S. "A Techno-Economic Analysis of the Application of Continuous Staged-Combustion and Flameless Oxidation to The Combustor Design in Gas Turbines", Fuel Processing Technology 87 (2006) 727–736, 2006

[60] Wünning, J., A., Wünning, J., G., "Flameless Oxidationto Reduce Thermal NO-Formation", Prog. Energy Combust. Sci. Vol. 23: 81 – 94, 1997

[61] Wulff, A., Hourmouziadis, J., "Technology Review of Aeroengine Pollutant Emissions", Aerospace Science and Technology, No 8: 557-572, 1997

[62] "Catalytic Combustion Over Platinum Group Catalysts: Fuel-lean Versus Fuel-Rich Operation", Catalysis Today 83, pp 71-84, 2003

[63] Smith, L., L., Karim, H., Castaldi, M., J., Etemad, S., Pfefferle, W., C., "Rich-Catalytic Lean-Burn Combustion for Low-Single-Digit NO_X Gas Turbines", ASME GT-2003-38129, 2003

[64] Lyubovsky, M., Smith, L., L., Castaldi, M., J., Karim, H., Nentwick, B., Etemad, S., LaPierre, R., Pfefferle, W., C., "Rich-Catalytic Lean-Burn Combustion for Fuel-flexible Operation with Ultra Low Emissions", Catalysis Today 117, pp 438-446, 2006

[65] Arellano, L., O., Bhattacharya, A., K., Smith, K., O., ”Demonstration of Engine-Ready Surface-Stabilized Combustion System”, ASME GT2006-91285, 2006

[66] Miller, J., A., Bowman, C., T., “Mechanism and Modeling of Nitrogen Chemistry in Combustion”, Prog. Energy Combust. Sci Vol. 15: 287 – 338, 1989

[67] Schmidt, C., C., Bowman, C., T., “Flow Reactor Study of the Effect of Pressure on the Thermal De-NOX Process”, Combustion and Flame, Vol. 127 Issue 1/2: 1958-1970, 2001

[68] International Energy Agency, “IEA World Energy Outlook 2004”, 2004

[69] Hallock, J., L., Tharakan, P., J., Hall, C., A., S., Jefferson, M., Wu, W., “Forecasting the Limits to the Availability and Diversity of Global Conventional Oil Supply”, Energy 29 (2004) 1673–1696, 2004

[70] Fjellerup, J., Ahrenfeldt, J., Henriksen, U., Gøbel, B., “Formation, Decomposition and Cracking of Biomass Tars in Gasification”, Technical University of Denmark: MEK-ET-2005-05, ISBN: 87-7475-326-6, 2005

[71] Chomiak, J., Longwell J., P., Sarofim A., F., “Combustion of Low Calorific Value Gases; Problems and Prospects” Prog. Energy Combust. Sci. 1989. Vol. 15: pp. 109-129, 1989

[72] Olofsson, G., “A Study of Biomass Combustion Problems and the Selective Catalytic Oxidation of Ammonia”, Doctoral Thesis, Lund University, ISBN: 97-7422-067-5

[73] Wu, P., K., Kirkendall, K., A., Fuller, R., P., Nejad, A., S., ”Breakup Processes of Liquid Jets in Subsonic Crossflows”, J. of Propulsion and Power, 13(1): 64 – 73, 1997

[74] Sirignano, W., A., Mehring, C., “Review of theory of distortion and disintegration of liquid streams”, Progress in Energy and Combustion Science 26: 609–655, 2000

[75] Bayvel, L., Orzechovski, Z., “Liquid Atomization”, Taylor & Francis, ISBN 0-89116-959-8, 1993

[76] Reitz, R., D., Bracco, F., V., “Mechanism of Atomization of a Liquid Jet” Phys. Fluids 25(10): 1730 – 42, 1982

[77] Malloggi, S., Tognotti, L., “An experimental Study on the Mechanism of Jet Breakup”, Proc. Of the Two-day Meeting on Sprays and Their Applications, Milan, Italy, 1986

[78] Powell, C., F., Yue, Y., Gupta, S., McPherson, A., Poola, R., Wang, J., "Development of a Quantitative Measurement of a Diesel Spray Core Using Synchrotron X-Rays", Argonne National Laboratory, Argonne, IL

[79] Powell, C., F., Cheong, S.-K., Ciatti, S., A., Liu, J., Wang, J., "X-Ray Characterization of Diesel Sprays and the Effects of Nozzle Geometry", Presentation at Diesel Engine Emissions Reduction Conference, San Diego, 2004

[80] Lin, S., P., Reitz, R., D., "Drop and Spray Formation from a Liquid Jet", Annu. Rev. Fluid Mech., 30: 85 – 105, 1998

[81] Vahedi Tafreshi, H., Pourdeyhimi, B., "The Effects of Nozzle Geometry on Waterjet Breakup at High Reynolds Numbers", Experiments in Fluids 35: 364–371, 2003

[82] Stiesch, G., "Modeling Engine Spray and Combustion Processes", Springer Verlag, ISBN 3-540-00682-6, 2003

[83] Launder, B., E., Loizou P., A., "Laminarization Of Three-Dimensional Accelerating Boundary Layers In A Curved Rectangular-Sectioned Duct", Int. J. Heat and Fluid Flow, Vol. 13, No. 2: 124 – 131, June 1992

[84] Marmottant, P., Villermaux, E., "On Spray Formation", J. Fluid Mech., vol. 498: 73–111, 2004

[85] Pilch, M., Erdman, C., A., "Use of Breakup Time Data and Velocity History Data To Predict the Maximum Size of Stable Fragments for Acceleration-Induced Breakup of a Liquid Drop", Int. J. Multiphase Flow Vol. 13, No. 6:741 – 757, 1987

[86] Theofanous, T., G., Li, G., J., Dinh, T., N., Aerobreakup in Rarefied Supersonic Gas Flows", Trans. Of the ASME J. of Fluids Eng., Vol. 126, July 2004

[87] "Drop Deformation and Breakup due to Shock Wave and Steady Disturbances", Int. J. Multiphase Flow Vol. 21, No. 4: 545 – 560, 1995

[88] Dai, Z., Faeth, G., M.,"Temporal Properties of Secondary Drop Breakup in The Multimode Breakup Regime", Int. J. of Multiphase Flow 27: 217 – 236, 2001

[89] Park, S., W., Kim, S., Lee, C., S., "Breakup and Atomization Characteristics of Mono-Dispersed Diesel Droplets in A Cross-Flow Air Stream", International Journal of Multiphase Flow 32: 807 – 822, 2006

[90] http://www.aem.umn.edu/research/Aerodynamic_Breakup/

[91] Joseph, D., D., Belanger, J. Beavers, G., S., "Breakup of a Liquid Drop Suddenly Exposed To a High-Speed Airstream", Int. J. of Multiphase Flow 25: 1263 – 1303, 1999

[92] Cavaliere, A., Ragucci, R., Noviello, C., "Bending and break-up of a liquid jet in a high pressure airflow", Experimental Thermal and Fluid Science 27: 449–454, 2003

[93] Povinelli, F., P., "Displacement of Disintegrating Liquid Jets in Crossflow", NASA Technical Note D-4334

[94] Rachner, M., Becker, J., Hassa, C., Doerr, T., "Modelling of the Atomization of a Plain Liquid Fuel Jet in Crossflow at Gas Turbine Conditions", Aerospace Science and Technology 6: 495 – 506, 2002

[95] Ragucci, R., Bellofiore, A., Carulli, G., Cavaliere A., "Momentum Coherence Breakdown of Bending Atomizing Liquid Jet", C.N.R., Napoli, Italy, 2002

[96] Birouk, M., Azzopardi, B., J., Stäbler, T., "Primary Break-up of a Viscous Liquid Jet in a Cross Airflow", Part. Part. Syst. Charact. 20: 283 – 289, 2003

[97] Ragucci, R., Bellofiore, A., Cavallieri, A., "Statistical Evaluation of Dynamics and Coherence Breakdown of Kerosene and Water Jets in Crossflow", C.N.R., Naples, Italy, •2003

[98] Desantes, J., M., Arrégle, J., López, J., J., García, J., M., "Turbulent gas jets and diesel-like sprays in a crossflow: A study on axis deflection and air entrainment", Fuel 85; 2120 – 2132, 2006

[99] Birouk, M., Azzopardi B., J., Stäbler, T., "Viscosity effects on the break-up of a liquid jet in a cross airflow", •2003

[100] Ménard, T.,. Beau, P., A., Tanguy S., Demoulin, F., X., Berlemont,A., "Primary Break Up Modelling Part A: DNS, a Tool to Explore Primary Break Up", ICLASS06-034, 2006

[101] "BSA Flow Software, Installation & User's guide", Dantec Dynamics A/S, Pub no.: 9040U5717, 2002

[102] Albrecht, H.-E., Borys, M., Damaschke, N., Tropea, C., "Laser Doppler and Phase Doppler Measurement Techniques", Springer, ISBN: 3-540-67838-7, 2003

[103] "FlowMap Particle Image Velocimetry Instrumentation, Installation & User's guide" , Dantec Dynamics A/S, Pub no.: 9040U3623, 1998

[104] Jensen, K., D., "Flow Measurments", 10th Brazilian Congress of Thermal Sciences and Engineering, Nov. 29 - Dec. 03, 2004, Rio de Janeiro, RJ, Brazil

[105] Westerweel, J., "Theoretical Analysis of the Measurement Precision in Particle Image Velocimetry", Experiments in Fluids [Suppl.] S3-S12, Springer Verlag, 2000

11 Summary of Papers

Paper 1

Design & Evaluation of an LCV Combustor for the Volvo VT4400 Industrial Gas Turbine

By:

Pontus Eriksson, Steve Walsh, Rolf Gabrielsson, Lars Waldheim and Fredrik Hermann

ASME GT-2002-30088
ASME Turbo Expo, Amsterdam, Netherlands
June 3-5, 2002

This paper presents the design of a Low Calorific diffusion type combustor suitable for the Volvo VT4400 industrial gas turbine. The combustor was built and tested with various LCV gases typical of biomass gasification processes and steal reduction processes. The work was a collaboration between Volvo Aero Malmö and AIT Ltd. Burnley England (Now part of Smiths Group PLC). AIT was formerly Lucas Combustion Group, which has made important contributions to the field of gas turbine combustion design ever since the Whittle W2B.

The combustor shows excellent characteristics in terms of NO_X and CO emissions, both being in the single digit range when FBN was not present. The combustor converted between 90% and 60% of the FBN in the range 500 – 2500 ppm of FBN. The need for additional cleanup of fuel NO_X in a commercial implementation was evident from this paper.

In this paper the design work was carried out by AIT, the project was coordinated by the author with assistance from Rolf Gabrielsson. Chemical modeling was done by Dr. Hermann. L. Waldheim having much experience with the Värnamo plant provided expertise regarding the fuel compositions. The author wrote the paper.

Paper 2

Experimental Investigations of a Low Weber Liquid Spray in Air Cross Flow

By:

Pontus Eriksson, Raik Orbay, Jens Klingmann

ICLASS 06-277
ICLASS 2006 Kyoto, Japan
Aug.27-Sept.1, 2006

This paper presents the first results coming out of the "spray in cross-flow" rig designed and built by the author. A low-Weber spray was investigated with laser sheet photography using a long range microscope, PIV and PDA.

The spray, being a low-Weber spray is characterized by poor breakup, making it unsuitable for most industrial applications. It allows for the study of bubble breakup though – a phenomenon which has been reported only in passing in the literature of sprays. Besides being characterized with PIV and PDA in the far field (well away from the spray injection point), the near field was investigated with photographic techniques. This gave insight into the various forces acting in the breakup process from intact column to ligaments and ultimately droplets.

The author designed and built the spray rig used for the experiments. The experimental work was performed by the author and Dr. Orbay. Dr. Klingmann provided expertise on measurement techniques. The paper was written by the author and Dr. Orbay.

Paper 3

The Zimont TFC Model Applied To Premixed Bluff Body Stabilized Combustion Using Four Different RANS Turbulence Models

By:

Pontus Eriksson

GT2007-27480
ASME Turbo Expo 2007, Montreal, Canada
May 14-17, 2007

This paper presents investigations of four RANS models combined with the Zimont TFC model as implemented in CFX 10.0. The work was initiated by Volvo Aero Trollhättan as an attempt to find alternative CFD combustion models to use in the design of military afterburners.

It was concluded in the paper that the different RANS models yielded quite varying results in terms of turbulent velocity field and turbulent flame speed. It was seen that the k-ω model was best suited to reproduce the experimental data.

Computations and drafting of the paper were done by the author.

Paper 4

Off-Design Performance Investigation of a Low Calorific Value Gas Fired Generic Type Single-Shaft Gas Turbine

By:

Raik Orbay, Magnus Genrup, Pontus Eriksson, Jens Klingmann

Journal of Engineering for Gas Turbines and Power, May 2008, Vol. 130 / 031504

This paper presents investigations of off-design performance of two imagined single shaft gas turbines being subjected to fuels with lower heating value than designed for. One of the turbines was recuperated. The implications for the various components, such as compressor, combustor and turbine were discussed. The overall impact on performance for the turbine was also discussed.

Modeling and computations were done in IPSE-Pro by Drs. Orbay and Genrup. Drafting was chiefly done by Drs. Orbay and Dr. Genrup. The section about combustion chamber off-design behaviour was drafted by the author and Dr. Klingmann.

Paper 5

Off-design Performance Investigation of a Low Calorific Gas Fired Two-shaft Gas Turbine

By:

Pontus Eriksson, Magnus Genrup, Klas Jonshagen, Jens Klingmann

GT2009-59067
ASME Turbo Expo 2009, Orlando, Florida
June 8-12, 2009

This paper presents investigations of off-design performance for the Volvo VT4400 two-shaft gas turbine (i.e. what happens when the fuel is heavily diluted with CO_2 or N_2). The implications for the various components, such as compressor, combustor and turbines were discussed. The overall impact on performance for the turbine was also discussed. All components were unaltered throughout the analysis.

Modelling was done in IPSE-Pro by the author and Dr. Genrup. The author rewrote the compressor and turbine components to handle fully non-dimensional groups. The LPP combustor network was implemented by the author and Dr. Klingmann. Hot loss according to NACA TR-1300 was implemented by the author. Computations were done by the author. Paper drafting was done by the author, except the section on turbine flow-path redesign, which was authored by Dr. Genrup. The code for turbine through-flow design was developed by David Olsson and Dr. Genrup in Matlab. All co-authors contributed to evaluation of findings and conclusions.

Paper 6

Re-sizing of a Natural Gas Fired Two-shaft Gas Turbine for Low Calorific Gas Operation

By:

Pontus Eriksson, Klas Jonshagen, Jens Klingmann, Magnus Genrup

GT2009-60386
ASME Turbo Expo 2009, Orlando, Florida
June 8-12, 2009

This paper is a continuation of paper 5. Here the focus is on various resizing scenarios with the aim of re-optimizing the gas turbine for low calorific gas operation. A new flow path optimized for a fuel diluted with CO_2 to 5 MJ/kg is also proposed and compared with the original flow-path. In this particular scenario the compressor is un-modified.

Modeling was done in IPSE-Pro by the author and Dr. Genrup. The author rewrote the compressor and turbine components to handle fully non-dimensional groups. The LPP combustor network was implemented by the author and Dr. Klingmann. Hot loss according to NACA TR-1300 was implemented by the author. Computations were done by the author. Paper drafting was done by the author, except the section on turbine flow-path redesign, which was authored by Dr. Genrup. The code for turbine through-flow design was developed by David Olsson and Dr. Genrup in Matlab. All co-authors contributed to evaluation of findings and conclusions.

Paper 7

Low-calorific Fuel Mix in a Large Size Combined Cycle Plant

By:

Klas Jonshagen, Magnus Genrup, Pontus Eriksson

GT2009-59329
ASME Turbo Expo 2009, Orlando, Florida
June 8-12, 2009

This paper presents investigations of Low Calorific Gas firing in a combined cycle power plant. Three fuel types are tested and the response of the plant is investigated.

Modelling was done in IPSE-Pro by K. Jonshagen and Dr. Genrup. Computations were done by K. Jonshagen. Paper Drafting was done by K. Jonshagen and Dr. Genrup. The author provided gas turbine knowledge, IPSE-Pro modelling experience and contributed to evaluation of findings and conclusions.

Paper 8

Method for Transfer of PDA Measurements of Spray in Cross-flow to a Single Injection Point in CFD

By:

Pontus Eriksson

ICLASS 2009-141
ICLASS 2009, Vail, Colorado
July 26-30, 2009

This paper presents a method for computing a single injection-point spray in the CFX CFD package. An algorithm was implemented in Matlab and a suitable interface was written as a Fortran user subroutine in ANSYS CFX™ to read in the synthetic spray. A test section was designed and built to suit an existing spray rig. PIV measurements were done for the continuous phase flow to establish velocity profiles and turbulence intensities. PDA measurements were done for a water spray. The measured spray was used to create a synthetic spray for CFD. CFD computations were compared to the measured spray.

The author designed the test section hardware. PIV and PDA measurement setup was done by the author. Measurements were done by the author with kind assistance from Drs. R. Orbay and J. Klingmann. The algorithm to compute the synthetic spray was written by the author in Matlab. CFD computations were performed by the author. The paper was drafted by the author.

Paper 9

Investigations of a We=568/q=51 Water Spray in Air Cross-flow by Means of PDA Measurements and CFD

By:

Pontus Eriksson

ICLASS 2009-143
ICLASS 2009, Vail, Colorado
July 26-30, 2009

This paper is a continuation of Paper 8. The method presented in that paper was used to further study a particular spray. More measurement data is presented. CFD was performed with two-way coupling and RANS turbulence. Computations and measurements are compared.

Further CFD computations were performed by the author. The paper was drafted by the author.